ALKANES ACTIVATION OVER OXIDE CATALYSTS

Filippo Marozzelli

PhD thesis, Cardiff University (2013)

Acknowledgments

First of all, I would like to express how grateful I am with my supervisor, Dr. David J. Willock, for having given me the opportunity to work on such a challenging and interesting topic, guiding me through the development of my research skills and the application of my computational knowledge that improved every day. Also, I would like to thank my other supervisor Dr. James A. Platts for his useful work related (but not only) advises and Prof. Graham Hutchings for his helpful and encouraging remarks during and after the frequent CCI meetings.

I would like to thank all the past and present members of the Theoretical Chemistry group at Cardiff University like Prof. Peter Knowles, Dr. Massimo Mella and my co-workers and friends from the office 1.95.

I could never be who I am now without my parents and my family with their support, love and understanding. Thank you also to my son Morgan (6) who made my time away from the calculations the best possible of my life. The first two years of this project we made our daily trips on the train to Cardiff where I would drop you off in nursery before going to work across the road. Then you started your school and although we were not making those trips together anymore you were still in my mind all the time. I also thank you for your presence right next to me in the last weeks of thesis write up, when I was working on my computer.

Finally, I would like to thank the ARCCA cluster division of Cardiff University for the time on Merlin and Raven computers and thanks also to the Materials Chemistry Consortium for the time on the supercomputer Hector.

Contents

Summary

The basics of the oxidation mechanism of different alkanes within zeolites and over molybdenum oxide surfaces were studied employing state of the art computational modelling.

It was shown that the constrained environment inside *MFI*, *MFS* and *MOR* induces terminal selectivity on the reaction of 6-, 8- and 10- term linear alkanes, *i.e. hexane*, *octane* and *decane*, respectively. The Monte Carlo (MC) random alkane configuration sampling showed that the oxidation reactivity is driven by the fact that the terminal C atoms of the substrate are more likely to be closer to the zeolites internal walls than the methylene (–CH_2–) C atoms. As a confirmation of this, the calculation of k_{prim}/k_{sec} for all the host/guest (alkane/zeolite) systems estimated that the *pore effect* exerted by the zeolites in the reaction favors terminal products (*terminal selectivity*).

The alkane oxidation over $MoO_3(010)$, $Fe_2(MoO_4)_3(001)$ and $(\bar{1}10)$ surfaces involved the activation of a C–H bond of the substrate. The surface calculations were carried out using DFT+U to localize the electrons at a terminal point of the surface. Energy comparison with hybrid DFT (B3LYP) calculations for cluster models of the $MoO_3(010)$ surface showed consistency with the DFT+U results. The propane terminal C–H bond activation generated a propyl radical. Transition state structures were found for the adsorption of radical species on $MoO_3(010)$ and $Fe_2(MoO_4)_3(001)$ surface and the corresponding energy barriers showed that the adsorption on the former system is favored, which indicates that the $Fe_2(MoO_4)_3$ surface alone is not a good catalyst for the reaction studied.

DECLARATION

This work has not been submitted in substance for any other degree or award at this or any other university or place of learning, not is being submitted concurrently in candidature for any degree or other award.

Signed Date

STATEMENT 1

This thesis in being submitted in partial fulfillment of the requirements for the degree of PhD.

Signed Date

STATEMENT 2

This thesis is the result of my own independent work/investigation, except where otherwise stated. Other sources are acknowledged by explicit references. The views expressed are my own.

Signed Date

STATEMENT 3

I hereby give consent for my thesis, if accepted, to be available for photocopying and for interlibrary loan, and for the title and summary to be made available to outside organizations.

Signed Date

1. General Introduction

The content of this thesis focuses on the activation of alkanes over two different categories of catalysts, namely zeolites and molybdenum oxides. Background to these two subjects will be provided in section 1.1 of this chapter. Then, a discussion over the scope of this work and the questions addressed in it will be provided in section 1.2 and finally, in section 1.3, the outline of this thesis will be briefly described.

1.1 Sustainability and Waste Upgrade

In recent years the term "sustainability" has become an increasingly (if not the most) important aspect of the global chemical industry, and has had its expression in the radical rethinking of both production processes and actual products and chemicals targeted. The approach adopted within this reassessment can be described as an effort to improve all aspects involved in the chemical process, from the use of the energy required to run reactions (and its recovery), to limiting the waste produced and "recycle" it as feedstock for other processes, *etc.* but also an effort to enhance the selectivity of chemical processes and to find new alternative and more cost effective ways to obtain the same products with limited production of by-products, which is also linked to a more environmental-friendly approach.

Within this scenario, oxidation processes are instrumental to achieve an improved level of industrial chemistry sustainability because they provide the greatest technological potential of all processes and they are also fundamental to minimise the industry impact on the environment, both in terms of use of natural resources employed and of pollution produced. Particularly, oxidation catalysis plays a key role within this context for being the source of the most important polymer industry intermediates and monomers, the yearly production scale of which reaches large figures worldwide, and also for having been able to address the impact on the environment through a number of improvements that are continuously reaching new

targets. For example, among these oxidation processes is the conversion of *para*-xylene to terephthalic acid (PET monomer) with 44 Mt produced every year by worldwide industry, 98-99% conversion and 93-97% selectivity. Within this process a list of various technological improvements can be mentioned. The terephthalic acid is oxidized with air in acetic acid (corrosive medium), and catalysed by various metals, among which is Br, which is toxic. The targeted improvements for this system are the removal of the corrosive medium, the bromine compounds and of the undesired by-products. Also, the use of a heterogeneous catalyst, that can be recovered and reutilised for a number of cycles, is also a targeted development. These are aspects to be added to the already important list of improvements introduced for this process including energy integration, safety and overall performance.

Another example of oxidation process for its worldwide importance is the oxidation of cyclohexane to the cyclohexanol/-one mix (K/A oil) with 90% selectivity. Cyclohexanol and cyclohexanone represent important precursors for the production of adipic acid and caprolactam, respectively, and are intermediates in the production of nylon-6,6 and nylon-6 polymers, are used as solvents in varnishes and as stabilisers and homogenisers for soaps and synthetic detergent emulsions. Cyclohexanone alone (6 Mt a^{-1}) is also used in the production of insecticides, herbicides and pharmaceuticals. The reaction conditions for the oxidation of cyclohexane require high pressure and temperature, therefore the safety for this process has been enhanced and the overall improvement of its technology has been further developed too. Also, the slightly more economic gaseous oxygen (O_2) as an oxidant has replaced the use of air. The targeted improvements for this reaction are the enhancement of the per-pass conversion (currently 10-15%) and the selectivity itself. Important achievements though have been reached for the oxidation (with HNO_3) of K/A oil to adipic acid. The process has a 100% conversion and 95% selectivity, which have to be added to the abatement of N_2O as by-product, employed as oxidant in the integration with the downstream process, and the recycling of NO and NO_2. The targeted improvements for this reaction are several, from developing a direct oxidation of cyclohexane to adipic acid, to the performance enhancement of the current process with cyclohexanone, to the use of O_2 as oxidant

to replace HNO_3. The process to convert cyclohexanone to caprolactame (with H_2O_2), via a cycloheaxanone oxime rearrangement, has also had several improvements introduced. The reaction has 100% conversion and 96-98% selectivity. The newly introduced oxidant, *i.e.* H_2O_2, allows the removal of ammonium sulphates produced in the classic process (Raschig process) during the oxime formation.

The two processes just described, although very important for the wide application of their products, represent only a fraction of this technology. In fact, the large variety of processes (and operative conditions) at industrial level require an equally long list of oxidants, ranging from the clean and benign ones, *i.e.* air, to the more hazardous, like for example all forms of Cr(VI) (chromium VI) salts which are powerful oxidising agents and also highly toxic pollutants for the environment and dangerous carcinogens for human beings. Within the group of heavy metal oxidants, chromium reagents have been abundantly used for years in industry like the Collins reagent prepared by dissolving CrO_3 in CH_2Cl_2, or the pyridinium chlorochromate (PPC), formed by CrO_3 and HCl dissolved in pyridine and the pyridinium dichromate (PDC), prepared by dissolving CrO_3 in H_2O and then in pyridine. Some of the other oxidants employed in industry that belong to this category contain selenium, ruthenium, lead, osmium, phosphorous, silver and aluminium, while other categories of agents that do not contain harmful metals are the perchlorates, peroxides, iodine compounds, N-oxides, TEMPO agents (radicals) and bismuths. Due to their high reactivity, these agents are necessarily noxious to human health to different extents, nevertheless they all have to be handled cautiously with safety equipment when used during reactions and also their disposal has to adhere to strict health and safety procedures.

The use of fossil fuels is increasing and the interest in the technology to make molecules derived by these fuels industrially available for the production of transportation fuels is globally renewed around the world. A huge effort has been and is still being dedicated by the policies of those countries responsible for larger use of fossil fuels, and therefore for the higher release of gases in the atmosphere, to promote alternative and sustainable energy sources. The objective of that approach

has two important goals: to limit the climate change problem caused, among other factors, by the long term unrestricted use of sulphur containing fuels and, most importantly, to provide an alternative energy source when the natural worldwide reserves are no longer available. Despite the efforts to fulfil these tasks, no substantial alternative is achievable in the foreseeable future.

The energy requirements within each developed country are fundamentally based on availability of chemicals such as gasoline and diesel. These transportation liquid fuels are produced *via* chemical conversion of coal, natural gas and bio-renewable feedstock into CO/H_2 products. One of the aspects of this sulphur-free process that represents a concern, and that has only recently started to be addressed by the world leaders in this technology, is the production of significant amounts of a major by-product represented by C_7-C_{12} linear alkanes. A low content in octane prevents the use of these hydrocarbons as fuels (gasoline), therefore the need of somehow "recycle" and convert these products into something that can be fully used has become of primary importance.

The current processes available to upgrade these alkanes to fuels either involves the use of acid catalysis[1] corrosive agents, with production of vast amounts of waste, or is characterized by a multistep oligomineralization of ethene to longer α-olefins followed by its carbonylation (hydroformylation or Ziegler process).[2]

At petrochemical industrial level, the Fluid Catalytic Cracking (FCC) is the most important process of conversion employed to obtain valuable products. The process upgrades heavy molecular weight and high boiling point by-products of the crude oil distillation into higher octane content products. The "heavy" gases are vaporised over zeolitic powders (generally faujasite)[3] where the cracking process takes place leading to the production of gasoline, aromatics and olefins. Currently, the global FCC capacity stands at 14.39 MMBPD (million barrel per day), or 716.6 Mt (mega tonne), and the worldwide crude distillation capacity is at a total of 88.03 MMBPD (4,383.9 Mt).[4]

The possibility of developing a selective oxidation process to transform these alkanes into chemically valuable intermediates to be employed in the fuel production and in other industrial applications is currently being investigated.[5] This reaction is

able to give access to a broad range of valuable products like ketones, aldehydes, alcohols and acids. Therefore, this study will particularly focus on the direct functionalisation of alkanes to intermediates of important petrochemical industry production processes. The choice of directly functionalising paraffinic intermediates made available during the production of liquid fuels is dictated by different reasons, among which is the economic one.[6] Alkanes are obviously less costly while olefins, generally obtained *via* naphtha steam-cracking, have an added cost due to the process to produce them. Other aspects in favour of alkanes is represented by their versatility as sustainable building blocks for faster reactions with a decreased number of steps and that do not require aggressive conditions, toxic reactants or high energy requirements.[7,8,9,10] The target of this project is to identify suitable materials able to face all the challenges imposed by the heterogeneous catalysis and by the requirements of the partial selectivity oxidation reactions. Among the commodity chemicals targeted by this global approach are primary (terminal) alcohols with a straight chain of different lengths ranging from 4 or 6 terms up to over 22. These alcohols are mainly used in the industry for the production of surfactants but are also precursors of fuel additives. The functionalisation *via* partial oxidation of alkanes at terminal positions is the challenge this project faces. The starting point is represented by experimental results[11] showing an unprecedented terminal selectivity induced on *n*-hexane oxidation by one of the supporting systems chosen for this study, namely zeolites.

The identification of a suitable catalyst capable of supporting this process is the main goal of a combined effort between experimental work and the predictive theoretical modelling described in this thesis.

1.2 Aim and Scope of the Thesis

As already anticipated, the production of transportation fuels is one of the main issues of the modern era. Catalysis is a key discipline to understand the multiple aspects of the technology behind fuels industrial production and overlaps with many other disciplines like chemical engineering, physical chemistry, solid-state physics, organic and inorganic chemistry. Theoretical (and especially quantum) chemistry, is a more and more important tool of investigation to understand catalysis and has become an essential part of the experiment.

The objective of this computational work is to model candidate supporting systems capable of catalyzing the upgrade of C_7-C_{12} linear alkanes, by studying the basic mechanism of the supported reaction of these hydrocarbons. The systems studied are zeolites and molybdenum oxides. The partial oxidation process of alkanes to corresponding alcohols involves an initial chemical event represented by the alkane C–H activation, therefore the efforts of this study were concentrated on this step. Zeolites have been used for many years (and still are) as catalysts for a wide range of processes, and this was possible thanks to their structures characterized by channels and pores, that may resemble small reactions chambers, and by their chemical composition which gives them the ability to selectively switch to certain processes that in gas phase would unlikely occur. Molybdenum oxides (molybdena) are known to be able to catalyze the partial oxidation of alkanes, and this is largely supported in literature.[12,13,14] However, an important aspect of how molybdena actually are able to do so, namely how they activate the substrate by breaking the C–H bond, is still subject of study as unequivocal evidence of its mechanism has yet to be found.

1.3 Outline of the Thesis

Aims and findings of this study are briefly summarized in this section.

Chapter 2 will discuss the available literature on reactions where zeolites were employed, on the adsorption and reaction of the substrates considered in this study and on the characteristics of molybdenum oxides. The zeolites section will describe the chemical and structural characteristics of these catalysts, then a comparison between papers describing different systems where alkanes react and finally structures of molybdenum oxides and main reactions where they have been employed will also be discussed.

Chapter 3 will introduce the theoretical background to our work: characteristics of the Monte Carlo (MC) algorithms will be described as well as the implementation in the in-house C-code *Zebedde* employed in this work to sample important structural and reactivity data. Then, the fundamental theorems of the density functional theory (DFT) will also be discussed and its implementation within the *ab initio* code VASP for geometry optimization, calculation of vibrational frequencies and density of states.

Chapter 4 will deal with the methodology applied in this work: the first section will describe the modifications implemented in the *Zebedde* code to adapt the MC algorithm to the studied systems and the second section will detail the adsorption energy calculations for the systems alkane/zeolite. The third and fourth sections will explain the procedures employed to reach convergence for the DFT calculations parameters and how the lattice parameters were optimized, respectively. The fifth and sixth sections will describe the transition state search and cluster models construction, respectively.

These first four introductory chapters are followed by the results of this study that will be presented in two chapters.

Chapter 5 will deal with the reaction of three linear alkanes, namely *hexane*, *octane* and *decane*, of different chain lengths (six, eight and ten terms, respectively) adsorbing inside three different zeolites, namely *MFI*, *MFS* and *MOR*. After a brief introduction and a section on the computational details of these calculations, the chapter presents the results of the calculation probing the size effect in all the

combinations guest/host (alkane/zeolite) and will discuss the energetics behind it. The fourth section will present results of reactivity calculations built on the platform of data from the size effect findings in order to describe the *regioselectivity* imposed by the zeolite frameworks onto the products and in the last section, among the conclusions, a comparison will also be made with past experimental results found in literature.

Chapter 6, after the usual introduction and brief discussion on the computational details, will present results of the DFT periodic calculations of propane adsorbing on different surfaces and clusters cleaved from two bulk systems, namely orthorombic molybdate (molybdenum trioxide) MoO_3 and monoclinic iron (ferric) molybdate $Fe_2(MoO_4)_3$. In particular, the third section of this chapter will deal with the $MoO_3(010)$ surface and with the corresponding defective surface, which is the same surface with a terminal oxygen removed; results of the propane adsorption onto the defect will also be discussed in this section. Mention will be made of the DFT ability to model this defect by the use of DFT+U. Also, results of defect creation on clusters constructed from the $MoO_3(010)$ surface and of propane adsorption onto the defect will be presented and discussed. The final part of this section will present results of the transition state (TS) searches attempted for the surfaces described: the Nudged Elastic Band (NEB) method is employed for this purpose and energy profiles for the propane activation on the defective surface are given. The fourth section of chapter 6 will present results relative to $Fe_2(MoO_4)_3$ (001) and $(\bar{1}10)$ surfaces and to their corresponding defective surfaces, to propane adsorption onto the defects and to the transition state searches attempted to describe in details propane C–H bond breaking by employing the NEB method.

Finally, discussion of links and interconnections between chapters will be made in the general conclusions of the final chapter 7 and further methods for alternative studies of these systems will also be mentioned.

References

[1] Z. Zhang, S. Sui, F. Wang, Q. Wang, C. U. Pittman, Jr. *Energies*, **6**(9), 4531-4550 (2013).
[2] K.Weissermel, H.-J. Arpe *Industrial Organic Chemistry* (Wiley-VCH, 2003).
[3] Ch. Baerlocher and L.B. McCusker, Database of Zeolite Structures: http://www.iza-structure.org/databases/.
[4] 2014 - 2 / FCC Network News, Volume 51 - February 2014
[5] S. Pradhan, J. K. Bartley, D. Bethell, A. F. Carley, M. Conte, S. Golunski, M. P. House, R. L. Jenkins, R. Lloyd, G. J. Hutchings *Nat. Chem.*, **4**, 134-139 (2012).
[6] J. F. Bradzil *Top. Catal.*, **38**, 289 (2006).
[7] M. Misono *Top. Catal.*, **21**, 89 (2002).
[8] M. M. Bhasin *Top. Catal.*, **23**(1-4), 145 (2003).
[9] J. M. M. Millet *Top. Catal.*, **38**, 83 (2006).
[10] A. Costine, B. K. Hodnett *Appl. Catal. A*, **290**, 9 (2005).
[11] B.-Z. Zhan, B. Modén, J. Dakka, J. G. Santiesteban, E. Iglesia *J. Cat.*, **245,** 316–325 (2007).
[12] K. Otsuka, Y. Wang, I. Yamanaka, A. Morikawa *J. Chem. Soc., Faraday Trans.*, **89**, 4225 (1993).
[13] M. D. Amiridis, J. E. Rekoske, J. A. Dumesic, D. F. Rudd, N. D. Spencer, C. J. Pereira *AIChe J.*, **37**, 87 (1991).
[14] M. R. Smith, U. S. Ozkan *J. Catal.*, **141**, 124 (1993).

2. Literature Review

This work focuses on the role played by catalysts in heterogeneous catalysis and in particular within the oxidation of hydrocarbons, as anticipated in the introduction. Also, attention is paid on the extent of the influence that these catalysts have over the products of the reaction. These important pieces of information can drive design and development of solid catalysts towards new objectives, such as performance improvement and decrease of the impact that chemical waste has on the environment. The examples of catalyst-substrate system studied in this project are relative to *(a)* reactions of linear alkanes with different chain length occurring inside different types of zeolites and *(b)* a partial alkane oxidation over molybdenum oxide surface of different metal compositions. The number of articles published on these topics is considerable, so this chapter will attempt to describe the fundamental characteristics of the catalysts considered. Prior to this, a brief description of the type of oxidation reaction being studied is provided to justify the choice of the catalytic systems analysed here.

Hydrocarbon activation through oxidation is one of the two processes in heterogeneous catalysis employed within the petrochemical and fine chemistry industry, the other process being hydrogenation. The selective oxidation process has not been employed and developed as much as the hydrogenation and the reason can be found in the chemical characteristics of the oxidizing agents employed: they can either be stoichiometric oxygen donors or molecular oxygen (dioxygen O_2) itself can be such agent. In the former case, the very low conversion efficiency of the oxidants leads to large production of waste. Instead, when molecular oxygen is employed, both low selectivity of the reaction and relatively stable products obtained within a homogeneous process make this reaction industrially unattractive. Notoriously, oxidations carried out with dioxygen are spin-forbidden since O_2 is found in a triplet state (T) in nature while organic substrates are in a singlet state (S). The activated oxygen species is generally obtained *via* reductive oxidation of O_2 at the catalyst surface in presence of bivalent metals. Metal and mixed metal oxides are materials the selectivity of which can be dramatically modified. The presence of peroxo

species, for example, can further activate the already activated oxygen species increasing its nucleophilicity with respect to its reactivity towards the co-adsorbed substrate. The consequence of this is that the metal centres become progressively more oxidised and the bonding interaction metal centres–active oxygen strengthens, which is expression of the change from electrophilic to nucleophilic reactivity.

As often happens, nature can represent an important source of inspiration for science: *Methane Monooxygenase* (MMO) enzyme found in microorganisms, catalyzes the oxidation of methane to CH_3OH employing a diiron centre and using molecular oxygen as oxidant. The diiron centre is part of the hydroxylase protein, one of the three units MMO enzyme active site is composed of (figure 2.1).

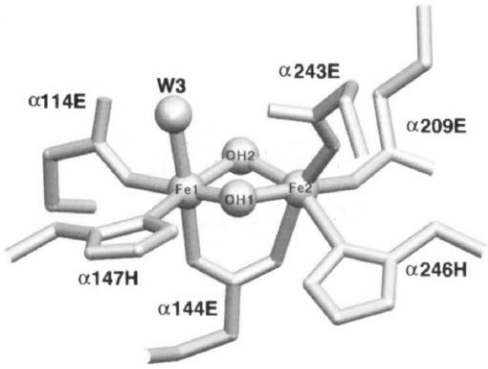

Figure 2.1. MMO enzyme is composed of three units: shown is the hydroxylase protein unit with its di-iron centre active site (figure taken from reference 1).

The di-ferrous form of the hydroxylase protein ($MMOH_{red}$), where both Fe centres are reduced (Fe^{II}–Fe^{II}), starts the catalytic cycle[1] by reacting with the molecular oxygen, as shown in figure 2.4. Three spontaneous reactive steps form a metastable compound (intermediate O, not shown in figure 2.2), a Fe^{III}–Fe^{III} peroxide compound (intermediate P) and finally the proposed Fe^{IV}–Fe^{IV} oxidizing agent of the reaction (intermediate Q), respectively.

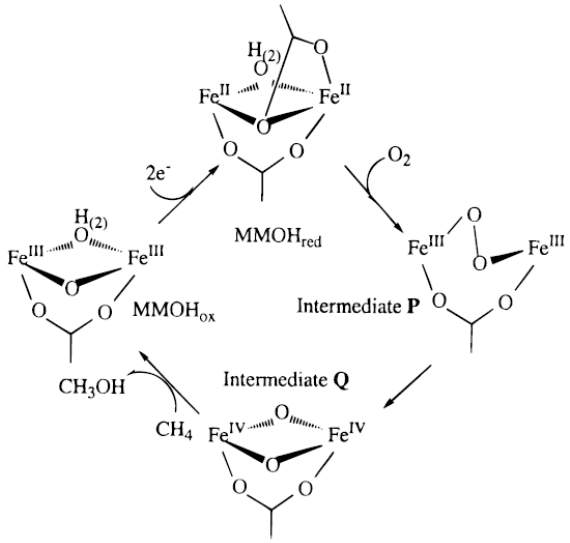

Figure 2.2. MMO catalytic cycle as proposed experimentally (figure taken from reference 1).

The cycle is closed after CH_4 reacts with the enzyme: the activation of one of alkane's C–H bonds is somehow triggered by the reduction of the di-iron centres from (IV) to (III) oxidation state. The methyl radical then formed reacts with the OH. Although MMO is very selective and therefore interesting to model and mimic within the homogeneous catalytic oxidation field, it does not represent an industrially attractive system due to its low turnover frequency.

Cytochrome P450[2] enzymes represent a major player within the areas of toxicology, drug metabolism and pharmacology. P450s are found throughout nature and present in a large number of forms, therefore large is the nomenclature system to identify the components of this group of enzymes. This system is based on families, subfamilies and individual P450s. Eight are the known P450s structures today. All the P450s structures have common regions. The proteins are arranged in similar helices, some of which are in contact with the substrate. The sequence Cys 357 in P450 101 identifies P450s in the gene banks because it corresponds to the most conserved region of P450s. In this region Cys acts as a thiolate ligand to the heme iron.

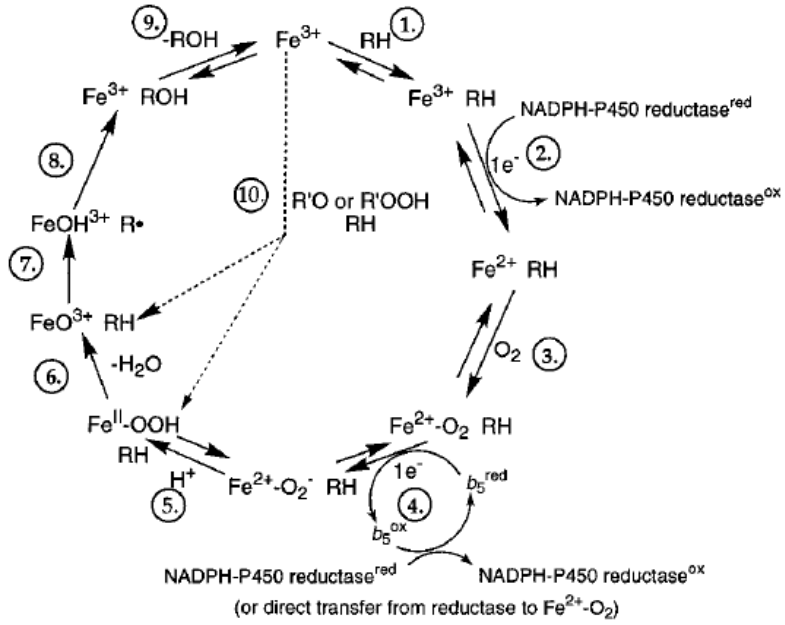

Figure 2.3. Generalised Cytochrome P450 catalytic cycle mechanism (scheme taken from reference 2).

Figure 2.3 shows the most accepted mechanism involving P450 catalysis. The oxidation P450s generally catalyse is the following:

$$NADPH + H^+ + O_2 + R \rightarrow NADP^+ + H_2O + RO$$

At the initial step, probably a rapid diffusion-controlled reaction, iron is in the ferric oxidation state, *i.e.* Fe(III). Step 2 is shown after step 1 because the latter is faster. Nevertheless, step 2 may still occur even when the substrate is not bound. NADPH is the source of electrons that travel through the flavins of the NADPH-P450 reductase. At step 2, ferrous P450 binds O_2. Fe(II) and $O_2^{\bullet-}$ (superoxide anion) may be produced during step 3 because of its instability and the complex Fe(II)$^{\bullet}O_2$ may be generated. At step 4 a second electron is released and a proton is added at step 5. This causes the O–O bond to cleave and generate H_2O and FeO^{3+} (of unknown electronic configuration) at step 6. At step 7, the complex abstracts either an H atom or an electron from the substrate, or else forms a sigma complex with the substrate itself. The product is generated following the intermediate collapse, as step 8. This step is referred to as *oxygen rebound* if H abstraction had occurred at step 7. The product desorbs from the enzyme at step 9.

In heterogeneous catalysis, the conditions under which reactions occur determine whether the solid catalyst is a key element within the overall reaction or it only plays a side role. Under low pressure conditions, the catalyst becomes very important for the partial oxidation of alkanes: CH_4 oxidation on silica-supported molybdate (MoO_3/SiO_2) is 90% selective to oxygenates (CH_3OH and HCHO) and yields CH_4 conversion up to 25% (873 K) in excess amount of water vapour over the catalyst, as Sugino *et al.*[3] report. Under high pressure conditions, the dominant process occurring in presence of a solid catalyst is a radical oxidation. In these conditions, although CH_3OH can be successfully produced,[4] CH_4 oxidation with O_2 is not successful if carried out with large majority of the metal oxide catalysts known: in this case, the factors playing a key role in enhancing the oxidation selectivity are those that generally can influence a gas phase reaction, such as type and geometry of the reactor, amount of time the gas spends in the reactor (residence time) and the isolation of unstable products at the reactor exit (quenching), namely the corresponding CH_3OH and HCHO. Otsuka *et al.*[5] attempted to draw an explanation (figure 2.4) of this by investigating the reaction mechanism when iron molybdate $Fe_2(MoO_4)_3$ is employed as catalyst for CH_4 partial oxidation to CH_3OH.

$$CH_4 \xrightarrow{O_2 \rightarrow O_{ads}} CH_{3\,ads}\,(\text{or } CH_3O_{\,ads}) + H_{\,ads}\,(\text{or } OH_{\,ads}) \longrightarrow CH_3OH$$

Figure 2.4. Mechanism model for CH_4 partial oxidation over iron molybdate $Fe_2(MoO_4)_3$ catalyst (the subscript "*ads*" refers to adsorbed species over the catalyst surface): the substrate is activated by O_2 dissociation; O_2 can either be provided by the gas phase or by the lattice: once dissociated, it adsorbs too on the $Fe_2(MoO_4)_3$ surface. Otsuka's argument[4] is that protonation of CH_3O is prevented by the activated surface O atoms.

The very reactive O atoms from the surface make the mechanism in figure 2.4 very difficult to occur, triggering a complete oxidation of the two possible adsorbed intermediates (CH_3 and CH_3O) to obtain HCHO or CO_x rather than CH_3OH, product of the partial oxidation sought. Under the same conditions, at low temperature, $Fe_2(MoO_4)_3$ yields 100% CH_3OH conversion: this is only possible with the presence of a particular active site (Brønsted centre) capable of partially oxidize the

intermediates and therefore able to protect them from being completely oxidized. Also, the low temperature preserves the meta-stable product, CH_3OH, from decomposing or even from further oxidation. These elements highlight how crucial is the design of catalysts able to activate CH_4, and alkanes in general, at low temperatures, and to directly convert them to the corresponding alcohols.

The active oxygen species on the metal oxide surface are believed to be the initiator of alkane's C–H bond activation at the start of the reaction. The answer as to which one between the three possible adsorbed oxygen species,[6,7,8,9,10] namely O_2^-, O^- and O_2^{2-}, is the actual species responsible for the selective oxidation of alkanes has yet to be provided. It has been suggested[11] that the metal oxide lattice oxygen species of the Mo=O site leads to the partial oxidation of CH_4 over MoO_3/SiO_2, while the bridging oxygen species Mo–O–Mo is responsible for the complete oxidation.

Aluminophosphates (AlPO) represent a different category of solid catalysts falling in the same group of the zeolites. AlPO partially oxidize alkanes when exchanged with transition metals. AlPO-18[12] containing isolated Co(III) or Mn(III) ions acting as catalysts, is used in the oxidation of linear alkanes by employing molecular oxygen (air) via a free-radical chain-autoxidation mechanism. AlPO-18 has a similar channel system to that of the zeotopic analogue Chabazite[17] (pore aperture 3.8 Å). The framework spatial constraints selectively direct the oxidation towards the alkane terminal and secondary positions, the former being favoured over the latter, which goes opposite to the bond strength order[13] (terminal C–H harder to break: 104 kcal mol^{-1} compared to 94.6 kcal mol^{-1} and 91 kcal mol^{-1} for secondary and tertiary, respectively). During the templated hydrothermal syntheses,[14] Co(II) and Mn(II) ions are oxidized to their (III) state and replace the Al(III) ions on the framework. The ability of CoAlPO-18 and MnAlPO-18 to maintain their ions (III) state unchanged during the reaction and their framework constraints make AlPO-18 the AlPO family most active and most regioselective catalysts employed in alkane oxidation: MnAlPO-18 is 65.5% regioselective to the terminal products of the oxidation (CoAlPO-18 is 61.3%), *i.e.* 1-hexanol, 1-hexanone and hexanoic acid, compared to CoAlPO-36 being the nearest in terms of regioselectivity among all tested, with only 22.7% regioselectivity.[12]

2.1 Zeolites

The solid catalyst family includes a number of structurally and chemically different systems that in the last 60 years have played a fundamental role in the large scale industrial production of fine chemicals and within the oil industry. The diversity of reactions for which these systems have been and are still employed in industry is an indicator of their versatility. These catalysts can be grouped[15] in less than ten types of systems, *i.e.* zeolites, oxides, ion-exchange resins, phosphates, clays, immobilized enzymes, sulphates, carbonates and sulfonated polysiloxanes, and are currently being used in nearly 130 different chemical industry processes from cracking, aromatization, isomerization to hydration, dehydration and condensation or alkylation, etherification and esterification *etc.* Within the list of catalysts, zeolites play a major role since they are involved in at least 40% of all processes where solid acid-base catalysts are required.

In 1756 a Swedish mineralogist called A. F. Cronstedt was the first to describe the "boiling stones" (zeolites) after he heated stilbite with a blowpipe flame.[16] Several types of minerals and synthetic materials share some or majority of the characteristics that uniquely identify zeolites, and can be therefore classified generically as zeotypes: these include aluminophosphates (AlPO) formed by alumina and phosphorous based tetrahedra, as explained earlier, silico-aluminophosphates (SAPO's) which are built by introducing Si atoms into AlPO frameworks, metallo-aluminophosphate (MAPO) built by introducing transition metals into AlPO frameworks and MAPSO obtained when incorporating metals into SAPO's frameworks. Zeolites though are aluminosilicate microporous materials with a continuous framework and are reversible ion exchangers which can also be reversibly dehydrated.

The early use of natural zeolites in industry explored their ability to be essentially shape-selective molecular sieves;[17] in recent years though, by artificially controlling their crystallization, new zeolites were synthesized in predetermined shapes, structures and properties tailored for their industrial employment: the most important applications of zeolites are where they are employed as adsorbent, catalyst and ion-exchange materials. Synthetic zeolites represent the vast majority of these

compounds used today in industry; in fact aspects like larger surface, controlled pore size targeting the reactants dimensions, larger thermal and hydrothermal stability are characteristics of their flexibility. The use of synthetic zeolites in oil refining and in petrochemical applications largely contributed to their breakthrough in catalysis.

Zeolites can be modified in their structures with the possibility to include ions or atoms within their framework to enhance their chemical properties towards targeted reactions. This can be achieved by either modifying those active sites where the reaction is supposed to take place, or even by introducing new active sites where there was none before, through a targeted chemical exchange.

The zeolite chemistry is very important nowadays and is associated to environmentally friendly processes with limited (if existent at all) amount of waste with high activity, high selectivity and yields and they are catalytic solids with a large turnover number. Probably the largest application of zeolites is in the cracking processes employed in petrochemical industry. During the process called *thermal* cracking, high pressures and temperatures are employed to break up large and heavy hydrocarbon molecules to smaller molecules. The presence of Al-exchanged zeolites as supporting material allows performing the same reaction using milder conditions (*catalytic* cracking).

The processes zeolites can be designed to catalyze are mainly acid-base reactions. The active sites they possess within their framework can be acid, basic or both. Within this study, acid-site type zeolites will be discussed and studied.

On a general note, a Brønsted acid is able to transfer a hydrogen cation H^+ (proton) to its conjugated base: on a surface area, as well as on the internal walls of a zeolite, H^+ links to the surface anions. In gas phase a Lewis acid shares an electron pair with a base and on a surface area this means that a coordinative bond acid—base is established.

In order to introduce an acid site inside a zeolite framework, a replacement of Si atoms with tetrahedral coordinated Al atoms is necessary: the valence requirement for the active site is then satisfied by adding an H atom to the O atom bridging (O_B) between Al and Si atoms. This modification brings new characteristics within the system. The coordination of Al to O_B can be thought of as a Lewis acid-base interaction and this increases the Brønsted acidity of the H associated to O_B.

A formal definition of synthetic zeolite frameworks topology would describe them as aluminosilicate (4;2)-3D net materials where aluminium (Al) and silicon (Si) atoms are disposed three-dimensionally in a tetrahedral symmetry. Each atom (T) is connected to 4 other atoms which happen to be oxygen (O) atoms: this is driven by the formal 2-valence state of the oxygen anions and that allows links to two consecutive Al and Si atoms. In other words, zeolites are materials whose framework structure is composed of SiO_4 and AlO_4 corner sharing tetrahedrals joint together by O bridges.

Since tetrahedral 3D nets are very common in zeotypes, a way to classify these frameworks becomes fundamental; the approach followed is to identify subunits that can be uniquely linked. In zeolites, these primary building blocks are the just described as TO_4 tetrahedral units: their disposition creates a characteristic framework of tunnels and side pockets with opening dimensions ranging from 5 to 20 Å which is a fundamental characteristic of molecular sieves.

In zeolites, a channel free diameter is limited by secondary building blocks (rings) formed by the TO_4 units, so the pore aperture dimensions are related to the number of atoms rings include (ring size). Within the same zeolite, rings size varies and the resulting free diameter also varies, so the convention adopted to identify uniquely the distance between zeolite channel internal walls is to consider the smallest ring size of the largest channel. According to this rule, channels can be defined as *small*, *medium*, *large* and *ultra-large* if they are respectively formed by 8-, 10-, 12- and >12-rings blocks, giving origin to networks of structures like cylinders or cages that are also open to the outside.

The research field where zeolites are involved has been and continues to be rewarding thanks to the above properties that make these microporous frameworks unique materials for many industrial applications.

Also, due to the flexibility of the active acid sites that can be modified according to the chemical challenges they face and to their high surface area and pore volume, it is not surprising that zeolites have been and still are a very attractive target for study and development in catalysis.

A large availability of important information in literature drove the attention of this study towards diverse zeolites like Silicalite-1 (ZSM-5) or MFI, MFS (ZSM-57), Mordenite (MOR) and Chabazite (CHA).

2.1.1 Silicalite-1 (ZSM-5)[18] or MFI

Silicalite-1 contains straight, nearly circular (5.3 Å × 5.6 Å) channels (figure 2.6(a)) intersecting sinusoidal (5.1 Å × 5.5 Å) channels (figure 2.6(b)). Each channel is a chain (figure 2.5(b)) composed of eight 5-membered ring units (figure 2.5(a)) joined together to form a 3D framework; the chains fused together form layers and also create 10-membered ring apertures (figure 2.5(c)).

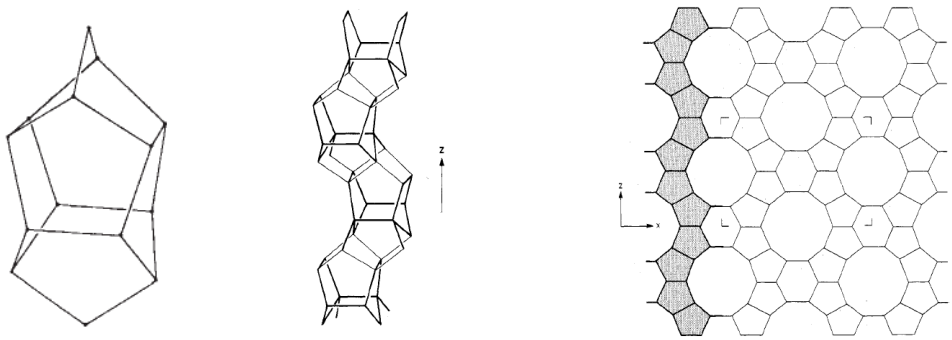

Figure 2.5. (a) 5-membered ring units as primary building block for Silicalite-1 (MFI); (b) framework of a channel formed by eight 5-ring units fused together; (c) layer formed by chains fused together and creating Silicalite-1 channels 10-membered ring openings (figures taken from reference 17).

A schematic drawing of how sinusoidal and straight channels intersect each other is shown in figure 2.6(c) while figure 2.6(d) shows internal surfaces artificially created to highlight the profile of the zeolite inner walls.

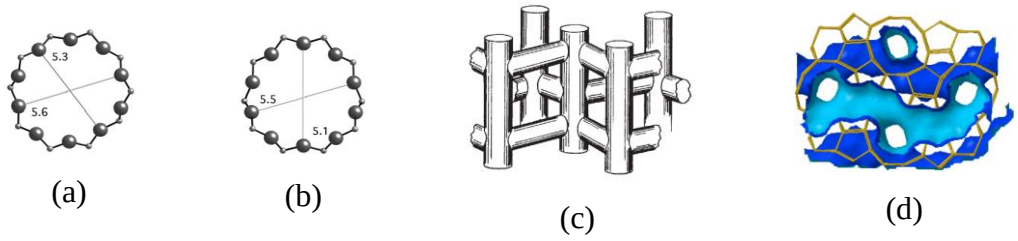

Figure 2.6. (a) Silicalite-1 (MFI) straight channel opening dimensions (5.3 Å × 5.6 Å); (b) sinusoidal channel opening dimensions (5.1 Å × 5.5 Å); (c) schematics of how straight and sinusoidal channels intersect each other; (d) internal surfaces highlighting profile of inner channel walls (figures taken from reference 17).

As just described, Silicalite-1 (MFI) has an uncharacteristic framework structure that gives it specific adsorption and diffusion properties directly linked to its *medium* size channel system, allowing access to molecules with diameters ranging from 6.3 to 7.8 Å.[19,20]

2.1.2 MFS (ZSM-57)[17]

The repeat unit in MFS is composed of 3 T atoms (figure 2.7(a), left) forming a "saw chain" building block, and six of these blocks make up the Periodic Building Unit (PerBU) (figure 2.7(a), right). Vicinal PerBU's are fused in a 4-, 5- and 6-ring system (figure 2.7(b)) to make up a MFS unit cell, a projection of which is shown in figure 2.8(a) (viewed along ***a***) and figure 2.8(b) (viewed along ***b***).

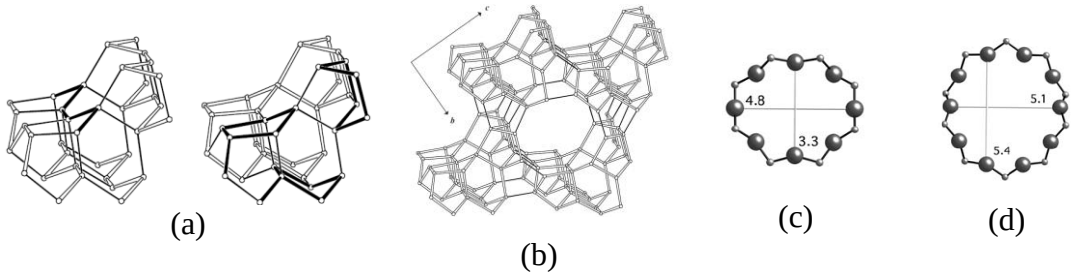

Figure 2.7. (a) MFS Primary building block "saw chain" (in bold) formed by 3 T atom elemental repeat unit (left) and Periodic Building Unit (PerBU) formed by the connection of six "saw chains" (right), both viewed along a; (b) PerBU's fused together through 4-, 5- and 6-ring units to form a typical connection mode for MFS viewed along a; (c) 10-ring channel opening (5.1 Å × 5.4 Å); (d) 8-ring channel opening (4.8 Å × 3.3 Å) (figures taken from reference 17).

In MFS there are 8- (4.8 Å × 3.3 Å) and 10-ring (5.1 Å × 5.4 Å) channels which are therefore classified as *small* and *medium*, respectively (figure 2.7(c), (d)). Figure 2.8(c) and (d) show internal blue surfaces highlighting MFS inner walls profiles, respectively along ***a*** and ***b*** directions.

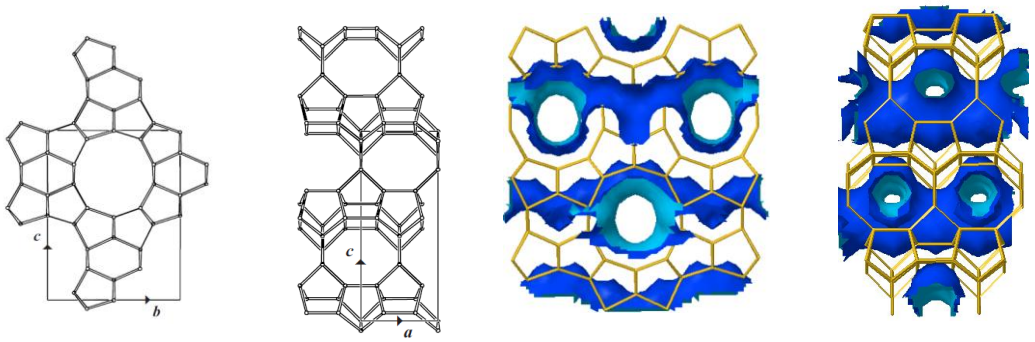

(a) (b) (c) (d)

Figure 2.8. MFS unit cell viewed along (a) *a* and (b) *b* direction; internal surfaces highlighting profile of inner channel walls viewed along (c) *a* and (d) *b* direction (figures taken from reference 17).

2.1.3 Mordenite (MOR)[17]

Mordenite is a high-silica zeolite whose framework building unit is composed by 12 T atoms disposed in a two fused 5-1 units block (figure 2.9(a)); two 5-1 units are linked to form a corrugated layer with a rectangular repeat unit (figure 2.9(b)). The layers (figure 2.9(c)) are connected through 4-atom rings to form a unit cell (figure 2.10(a)).

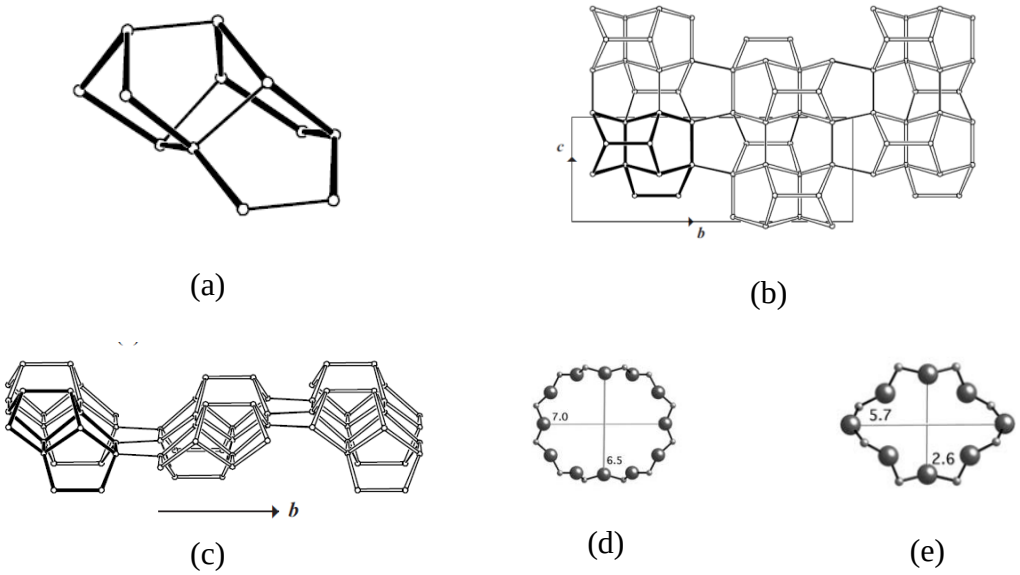

Figure 2.9. (a) Mordenite (MOR) 12 T atom unit; (b) layer formed by rectangular repeat units viewed along a; (c) the same layer viewed along c; (d) 8-ring channel opening (6.5 Å × 7.0 Å); (e) 10-ring channel opening (2.6 Å × 5.7 Å) (figures taken from reference 17).

The channel system is a 12-ring 1-dimension sinusoidal one with *large* (6.5 Å × 7.0 Å, figure 2.9(d)) and *small* (2.6 Å × 5.7 Å, figure 2.9(e)) channels and it includes two (4-rings), four (5-rings) and two (6-rings) side pockets accessible through 8-ring windows.

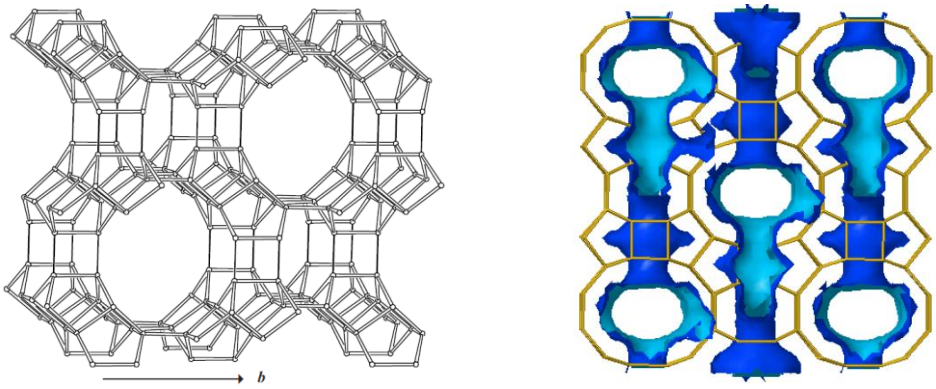

(a) (b)

Figure 2.10. (a) MOR unit cell viewed along c and formed by four layers fused vertically through four atom rings between each pair of layers; (b) internal surfaces highlighting profile of inner channel walls viewed along c (figures taken from reference 17).

2.1.4 Chabazite (CHA)[17]

The Periodic Building Unit (PerBU) of Chabazite (figure 2.11(a)) is two-dimensional and formed by non-connected planar 6-rings: their position, usually called A, is centred at (0,0) on the ***ab*** layer.

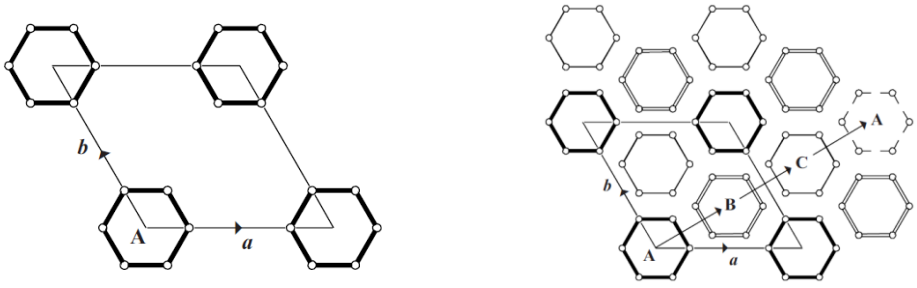

(a) (b)

Figure 2.11. (a) Periodic Building Unit (PerBU) in Chabazite (CHA). (b) CHA hexagonal arrays of planar 6-rings and definition of their positions with respect to each other (figures taken from reference 17).

Neighbouring PerUBs in CHA are connected through tilted 4-rings along +[001] direction.

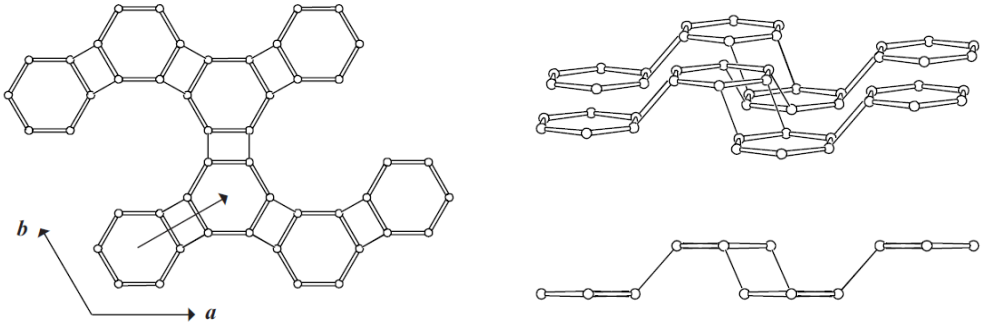

(a) (b)

Figure 2.12. Connection mode in CHA between the layers A, B and C to give the stacking sequence AB, BC and CA. (a) View along [001]. (b) *Top:* view nearly along [010]. *Bottom:* view along [010] (figures taken from reference 17).

There are three ways to build up layers and each way determines a different connection between layers. Starting from position A (figure 2.11(b)), shifting twice by +(2/3***a*** + 1/3***b***) creates layers B and C, giving rise to the first stacking sequence, namely AB, BC and CA (figure 2.12).

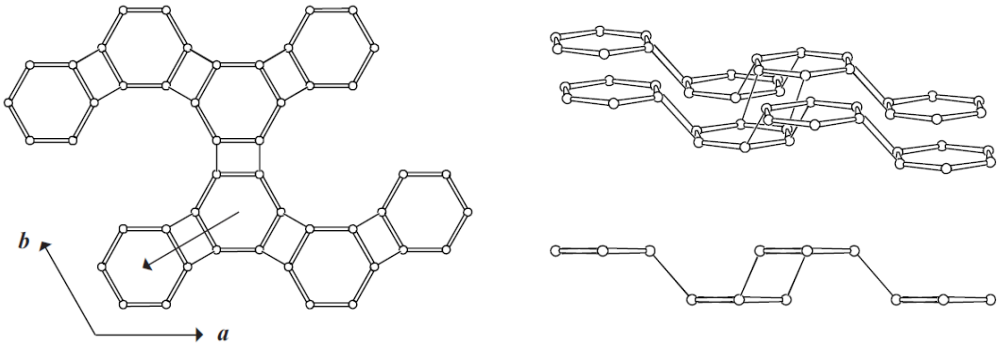

(a) (b)

Figure 2.13. CHA connection mode between the layers to give the stacking sequence AC, CB and BA. (a) View along [001]. (b) *Top:* view nearly along [010]. *Bottom:* view along [010] (figures taken from reference 17).

Repeating the process, shifting by +(2/3***a*** + 1/3***b***) from A gives rise to AC, CB and BA stacking sequence (figure 2.13), while a zero shift from either A, B or C creates an AA, BB or CC stacking sequence, respectively (figure 2.14).

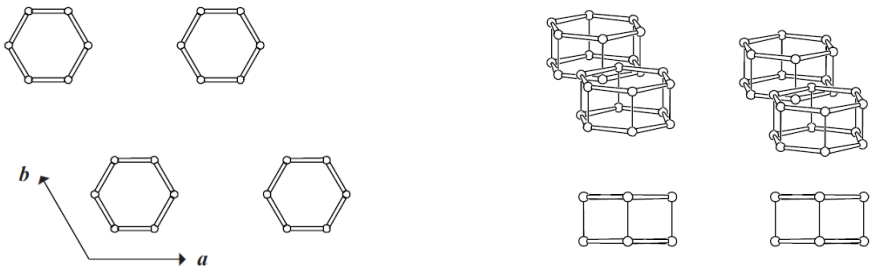

(a) (b)

Figure 2.14. CHA connection mode between the layers to give the stacking sequence AA, BB and CC. (a) View along [001]. (b) *Top:* view nearly along [010]. *Bottom:* view along [010] (figures taken from reference 17).

Figure 2.15(a) shows a *chab* cavity, a composite building unit that gives rise to a three-dimensional channel system (figure 2.15(b)) when interconnected with other cavities through 8- and double 6-rings.

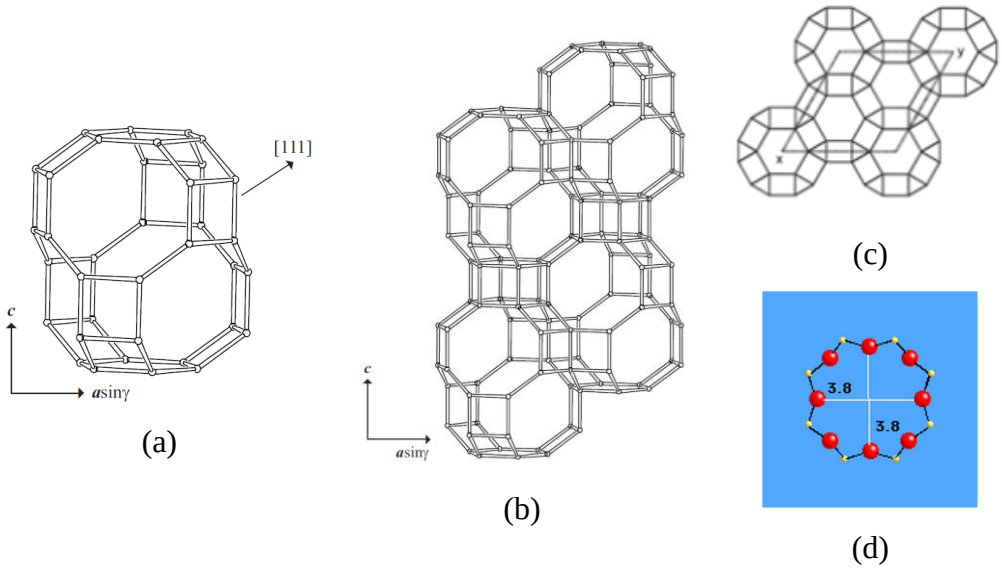

(a) (b) (c) (d)

Figure 2.15. (a) CHA *chab* cavity viewed along <010>. (b) CHA channels viewed along <010>. (c) CHA channels projection down [001] of the PerBU. (d) CHA channels dimensions (figures taken from reference 17).

The channels dimensions (3.8 Å × 3.8 Å, figure 2.15(d)) are variable due to the framework flexibility.

2.2 Alkanes Adsorption and Reaction

The products of heterogeneous oxidation catalysis reactions represent fundamental intermediates in most of nowadays main manufacturing industrial processes. The last decades have witnessed a major improvement in selectivity and efficiency of these reactions and, in the same effort, the environmental impact of these processes has also been reduced to a minimum. Within this scenario, since the breakthrough of the 1980's, the design of new catalysts has played a key role and this has been possible through a deep understanding of the fundamental principles of this type of catalysis. The scope of this project is well within this topic and its aim is to model and design novel and more efficient catalysts in order to enhance efficiency of the use of fuel production side products.

In heterogeneous catalysis where zeolites are employed as supporting materials (host), the reacting species (guest) undergo a series of chemical transformations both prior to reacting and following their conversion into products. Generally, *diffusion* of the reactants is the first event to occur inside the zeolitic pores and channels; this initial phase ends when the substrate reaches the active sites on the catalyst internal surface and *adsorption* at the active site then takes place, followed by the actual *reaction*. Once the reaction has reached completion at the active site, product *desorption* occurs, followed by its *diffusion* through the channels system.

If a metal oxide is employed as supporting material to oxidize alkanes, different events occur and therefore other characteristics of the catalyst can influence the oxidation of hydrocarbon species. As discussed earlier, it is understood that the metal oxide lattice oxygen is the actual oxidizing agent responsible for the substrate conversion into products, which is expected since at low temperatures hydrocarbon oxidations do not occur spontaneously in gas phase without the presence of a catalytic system. The molecular oxygen in gas phase though plays an important role within the heterogeneous catalysis, it restores the initial characteristics of the catalyst by oxidizing the reduced form of its surface and by doing this the catalytic cycle is closed, starting conditions are re-established and a new reactive cycle can be conducted with the same supporting material already used. The ability of the catalyst

to be "recycled" for its use in more than one consecutive chemical process is associated to the turnover number (TON), which is an important characteristic describing productivity, lifespan and degree of environmental impact of the catalyst itself.

In general, a strong M–O bond, where M is the chosen metal species, favours a less reactive process leading to a low yield of alkenes; conversely, a weak bond completely oxidizes the substrate leading to an unselective reaction. The M–O bond strength depends on the metal nature: covalent metals are more adapt if employed in catalytic systems and can also both oxidize (be reduced) and reduce (be oxidized), which is a *redox* requirement (amphoterism) for a system to be an efficient catalyst and essential to support a catalytic cycle.

Generally, the adsorption of species on a surface is a function of different aspects such as the intrinsic reactivity of the chemical species competing for a place at the active site (expression of their chemical nature), the selectivity of the local constraints at the active sites and the structure of the surface itself.

By using supporting materials for the oxidation of alkanes (like 3D crystalline aluminosilicate zeolites, with their characteristic system of internal micro-channels and pores) with the intent of enhancing the selectivity towards terminal carbon atoms, a range of more complex aspects are also introduced, aspects that can heavily influence the selectivity of the products sought: the *regioselectivity* of the reaction is no longer just a function of the intrinsic differences in reactivity between primary and secondary carbon atoms, as it would be in gas phase; local constraints at the active sites inside the zeolite structure where the reaction is forced to take place, can influence the chemical path of the reaction that can also be affected by the *shape selectivity*[14] that zeolite channel and pores layout is able to exert on the reaction.

One of the objectives of this study is to look at the latter aspect when zeolites are employed, and how it can modify regioselectivity and rate of linear alkanes oxidation to give corresponding alcohols.

Iglesia and co-workers[19] studied the oxidation of *n*-hexane inside Mn-exchanged zeolites of different framework dimensions and characteristics (*MFI*, *MFS*, *DDR* and *MOR*):[17] according to the mechanism proposed (figure 2.16), the reaction between

alkane and dioxygen leads to the formation of a key intermediate, namely hexylhydroperoxide (ROOH).

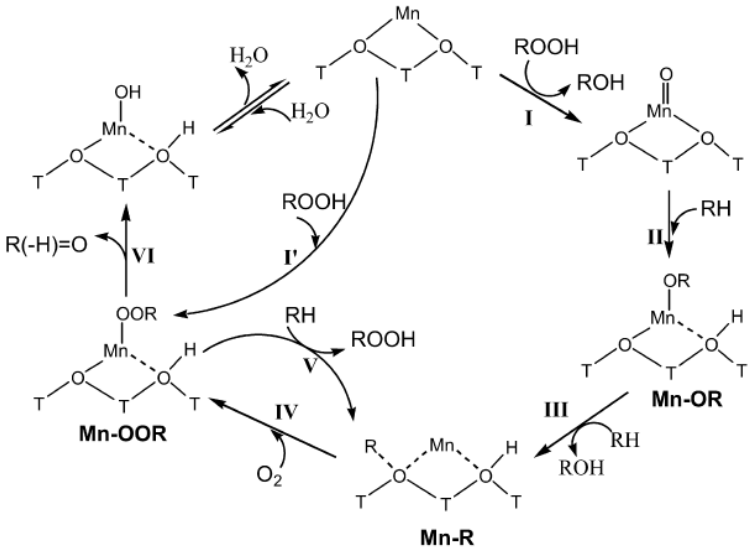

Figure 2.16. Scheme proposed by Iglesia and co-workers[21] for the catalytic oxidation of *n*-hexane on Mn-exchanged zeolites where ROOH (hexylhydroperoxide) decomposes to give ROH (hexanol), R(–OH)=O (hexanone) and hexanal as products (figure taken from reference 21).

ROOH appears to be essential in the regeneration of other important intermediates (Mn-OOR, step **I'**; Mn-OR, steps **I** and **II**). Consistent with the central role played by ROOH, the turnover rate for the production of ROH and R(–H)=O is proportional to the peroxide concentration. The decomposition of this peroxide, catalyzed by the Mn centres, is the kinetically relevant step of the reaction (steps **I** and **I'**). Also, diversity in catalyst structure and channel shape affects the accessibility of those centres: 10-ring zeolites (Mn-MFI, Mn-MFS) seem to favour the peroxide decomposition compared to 8- (Mn-DDR) and 12-ring (Mn-MOR) zeolites. The extent of framework constraint effect over the products (*shape selectivity*) was probed at low peroxide concentrations for a quick reaction time to minimize non catalytic processes: preferential O insertion was identified at alkane terminal over secondary positions inside Mn-MFI and Mn-MFS, with channel diameters of (5.3 Å × 5.6 Å) and (5.1 Å × 5.4 Å) respectively, rather than in Mn-MOR (6.5 Å × 7.0 Å),

while Mn-DDR (3.6 Å × 4.4 Å) showed noncatalytic characteristics due to the extreme difficulty for alkanes to enter and reach the Mn sites.

Mechanism and energetics are also discussed by Corà and co-workers[22] in a DFT study of Mn-doped nanoporous aluminophosphates, Mn-AlPOs, employed for the aerobic oxidation of alkanes.

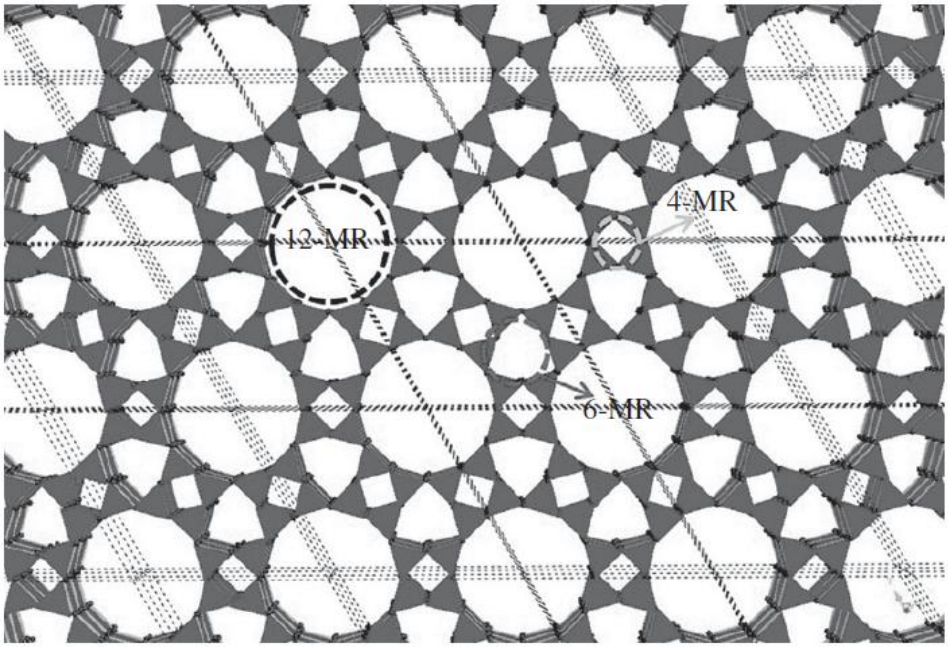

Figure 2.17. AlPO-5 aluminophosphate (AFI) structure with its pores of different sizes: 4- and 6- member ring (MR) channels are too small for any reaction of even small substrates as ethane to occur, on the contrary the 12-RM channels are large enough to be able to host the oxidation studied (figure taken from reference 20).

Figure 2.17 shows the AlPO-5 aluminophosphate (AFI) layout of pores: AFI is an open-structure microporous solid having active sites in the form of dopant ions incorporated isomorphously within its framework sites during its synthesis. AFI's channels are of three sizes, *i.e.* 4-, 6- and 12-member ring (MR) channels, and they are one-dimensional pores with no interconnections: the 12-MR channels (diameter 7.3 Å) are the only ones the substrate is able to access. The Mn dopants are Mn^{2+} ions replacing all Al^{3+} ions present in AFI. Because all of AFI's Al sites have equivalent symmetry, the definition of single-site heterogeneous catalyst (SSHC) for the Mn-doped AFI applies as the Mn active sites, in the form of MnO_4 tetrahedra, are located within an identical environment. Despite Mn-AFI being highly Mn-doped,

interactions between the substrate and vicinal Mn sites do not occur because the Mn^{2+} ions are located at tetrahedral positions allowing the Mn sites to be at least 8 Å apart from one another: this characteristic is fundamental when employing periodic boundary conditions (PBC), as in the work of Corà and co-workers,[20] in order to avoid inter-cell interactions.

The study uses predominantly ethane as substrate to investigate the elementary reaction steps identified in the radical mechanism described, introducing substrates that allow testing the reactivity against primary and secondary C atom oxidation only at those levels where selectivity of the reaction takes place, in order to identify its atomic-level origins.

1) $RH + Mn^{III} \rightarrow R\cdot + Mn^{II}(H)$

2a) $R\cdot + O_2 \rightarrow ROO\cdot$

2b) $ROO\cdot + Mn^{III} \rightarrow ROO\cdot(Mn^{III})$

3) $ROO\cdot(Mn^{III}) + RH \rightarrow ROOH(Mn^{III}) + R\cdot$

4a) $ROOH + Mn^{II}(H) \rightarrow RO\cdot(Mn^{III}) + H_2O$

4b) $ROOH + Mn^{II}(H) \rightarrow HO\cdot(Mn^{III}) + ROH$

5a) $RO\cdot(Mn^{III}) + RH \rightarrow ROH(Mn^{III}) + R\cdot$

5b) $HO\cdot(Mn^{III}) + RH \rightarrow H_2O(Mn^{III}) + R\cdot$

6) $ROO\cdot(Mn^{III}) + ROH \rightarrow ROOH + Mn^{II}(H) + CH_3CH(=O)$

Figure 2.18. Summary of the reaction cycle proposed by Corà and co-workers[20] of the ethane ($R = CH_3CH_2$) oxidation in Mn-AFI, a Mn-doped aluminophosphate (Mn-AlPO): elementary steps are reported. $L(Mn^X)$ indicates complexation of intermediate L on a Mn^{X+} site and $Mn^{II}(H)$ indicates that Mn^{II} active site has a H atom bonded to a vicinal lattice O atom.

The *preactivation* step (figure 2.18(1)) is a C–H homolytic cleavage of the substrate that generates the corresponding alkyl radical R· that, via addition of O_2 and complexation on a Mn^{III} site (figure 2.18(2a) and (2b)) leads to the complex $ROO\cdot(Mn^{III})$ responsible for sourcing ROOH (figure 2.18(3)) which complexes only on Mn^{II} sites (*decomposition* steps, figure 2.18(4a) and (4b)) that are oxidized to Mn^{III}. A further C–H homolytic cleavage generates more radicals (*propagation* steps, figure 2.18(5a) and (5b)) that, similarly to step (3) in figure 2.18, lead to partial oxidation products, *i.e.* ROH, H_2O and ROOH. A final H abstraction from ROH

leads to a *regeneration* step that allows the cycle to be closed by re-establishing the initial conditions on the catalyst via a reduction of the Mn^{II} sites (figure 2.18(6)). It was observed by Corà and co-workers that the thermodynamic driving force of this mechanism is the stabilization of a newly formed radical by the O_2 addition, provided by the high partial pressure of the gas at which these reactions occur. The role of the dopant ion present is both direct and indirect: in the former case, where the metal changes its oxidation state, Mn also breaks bonds to both generate radicals (step 1), with an activation energy gain of 53 kJ mol^{-1} if compared to the non-catalytic activation process, and to decompose ROOH (steps 4a and 4b), where the energy gain is of at least 101 kJ mol^{-1}; in its indirect role instead, Mn acts purely as a complexing agent with ROO· during another bond breaking (step 3), but it still gives its fundamental contribution by lowering the activation barrier for this step of 9 kJ mol^{-1} if compared to the same process occurring in AFI.

The study has identified three possible sources of product selectivity for the process studied: the first one is represented by the O_2 addition to the newly formed planar radical structure that, to avoid obvious steric clashes, occurs on the opposite side with respect to the H-like bond established between the radical C atom and the H atom bonded to a lattice O atom: this leads to an inversion of C site configuration which was not discussed further. The second possible source was identified in the competition between primary and secondary substrate C atoms during the C–H homolytic cleavage leading to corresponding radicals: an energetic analysis of this process with differently functionalized ethane molecules showed that the large AFI channels are not regioselective as the results of the study go in line with the gas phase C–H bond reactivity order, favouring the formation of secondary radicals over the primary. The third possible source of product selectivity was identified in the possibility that the formation of partial oxidation products could trigger their complete oxidation to carboxylic acids in presence of their intermediates, *i.e.* aldehydes (step 6).

Corà and co-workers also carried out extensive theoretical studies on the mechanism of Mn-catalysed hydrocarbon oxidation focussing the investigation on the different steps of the overall cycle proposed. They proposed four steps that feed one into the

other, starting from the *preactivation* step[23] that provides the required species for the transformation (*decomposition* step)[24] of the ROOH intermediate into the final products of the oxidation (alcohol, aldehyde and acid), occurring during the *propagation* step[25] that follows. The fourth and last step, *i.e. regeneration*,[26] is characterised by the oxidation cycle closure and the reactivation of the Mn(II) active sites.

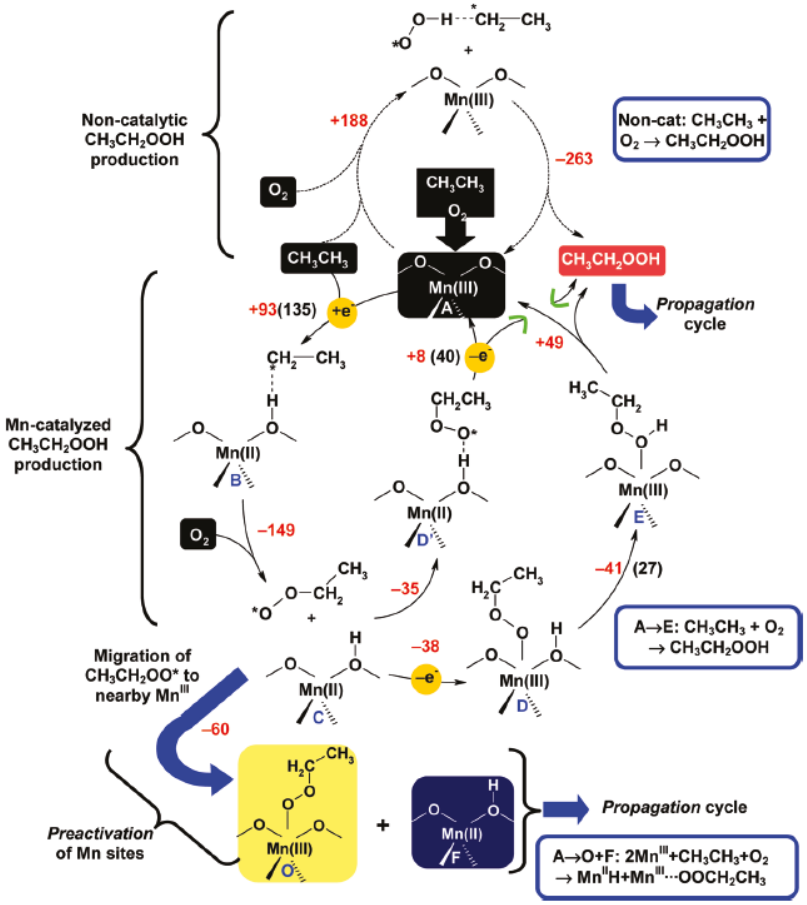

Figure 2.19. Uncatalysed (top) and catalysed (middle) preactivation mechanism (**A** to **E**) for the net production of CH_3CH_2OOH, starting from RH and O_2. Mn sites are also activated through reduction Mn(III) to Mn(II) (**F**) and formation of ROO···Mn(III) complex (**O**) after migration of ROO• radicals. Enthalpies (kJ mol^{-1}) and activation energies are in red and black, respectively (figure taken from reference 23).

The *preactivation* step (figure 2.19)[23] is characterized by the fundamental role played by the Mn active sites in activating the substrate through the interactions between metal centres, one molecule of alkane and one of O_2. These interactions are at the

core of the initial step occurring on the calcined (activated) Mn-doped aluminophosphate (AlPO) catalyst, and they lead to the formation of a reduced Mn(II) site and a Mn(III)···peroxo complex. The authors stress the importance that both Mn(II) and Mn(III) sites be present at the same time in order for the catalytic cycle to take place. It is reported that the catalyst calcination delivers a MnAPO material where all the Mn sites are in their oxidation state (III), which appears not to be enough for the propagation cycle to take place. Therefore, the *preactivation* step is deemed necessary in order to have all the key players in place, *i.e.* Mn(II) sites and peroxo radicals, for the reaction to be initiated.

The proposed catalytic mechanism was investigated with density functional theory (DFT) *via* use of a first principle simulation code and employing B2LYP as the hybrid-exchange functional. The reliability of this approach is reported to be proven by the comparison with X-ray adsorption spectroscopy data over the metal site positions in the MnAPO material framework.

The mechanism shown in figure 2.19 can be described as follows. The substrate (CH_3CH_3) is activated through the abstraction of a H atom by a lattice O atom bonded to the Mn(III) centre (**A** to **B**). The study elegantly shows how the metal centre drives the C–H bond homolysis, thanks to the ability of the Mn centre to be reduced to Mn(II), by studying the spin energies of metal and radical C atom and by calculating the spin density maps of all atoms directly involved. This validation is followed throughout the study for each step of the cycle. Energetic evaluations of the events occurring in these initial stages of the proposed *preactivation* mechanism confirmed that O_2 does not interact with any of the other species and also further confirmed the importance of the metal centre in the system. In fact, the ethane activation (**A** to **B**) occurring inside the Mn-AFI material is 33 kJ mol^{-1} more favourable than in absence of the catalyst or even when occurring in the AFI material (activation energy increasing asymptotically). Once **B** is formed, O_2 attacks the radical C atom stabilising it (large exothermic step). It is reported that the attack occurs on the opposite side of the transferred H•, with respect to the CH_2 plane, due to possible steric clashes with the channel wall (stereospecific attack). The **B** to **C** step is also confirmed by the growing C–H bond distance due to the presence of the

O_2 molecule that, attached to one end of the substrate, pushes the peroxo free radical ($^{*}OOCH_2CH_3$ or ROO•) in the centre of the catalyst channel.

The nonbonded nature of the ROO• species just formed allows it to either receive the lattice H species (**D'** or **D**), after reorienting itself accordingly within the channel, or migrate to a nearby Mn(III) centre (**O**). In the former case, Corà and co-workers reported two possible H-transfers. The first one (**D'**) describes a strong H-bond interaction radical-lattice H (ΔH = -35 kJ mol^{-1}) followed by the H transfer leading to the ROOH species (red box) with the closure of the cycle (**A**). Although the passage **D'** to **A** is energetically unfavourable, it still represent a possible pathway since it allows ROOH and the Mn(III) centre to be available for new reactive events. In the second possible H-transfer, the radical (**C**) adsorbs onto the metal centre and following a radical-stabilising proton rearrangement, Mn is oxidised to Mn(II) (**D**), the proton is transferred (**E**) and the ROOH intermediate is formed (**A**). If migration occurs (**O**), the ROO• species (**C**) leaves the Mn(II) centre and this appears to be justified by the orientation of the radical itself that points away from the metal centre. When the shift occurs, the Mn(II) centre is made available (**F**) to activate the *propagation* cycle in which ROOH, the net product of all the pathways described so far (**A→C→D→A** or **A→C→D'→A**), is decomposed following the scheme in figure 2.20. At the same time, ROO• adsorbs on a new Mn(III) centre (**O**) forming a complex 22 kJ mol^{-1} more stable than that formed in **D**. This new complex ROO···Mn(III) too takes part to the *propagation* step.[25]

$$ROOH + Me^{II}OH \rightarrow RO^{\cdot} + Me^{III}O + H_2O$$

Figure 2.20. Intermediate (CH_3CH_2OOH or ROOH) decomposition scheme occurring on Mn(II) active sites that catalyse the production of water molecules and alcohol, eventually leading to oxo-type radicals (scheme taken from reference 24).

The ROOH *decomposition*[24] occurs following the intermediate adsorption on the Mn(II) active sites made available during the *preactivation* step.[23] The framework's H atom reorients towards the centre of the channel, driven by the most favourable H-bond interactions between the H atom itself and the terminal intermediate O atom. At

this stage of the reaction, simultaneous and important steps take place (figure 2.21), *i.e.* the intermediate O–O bond homolysis leading to the formation of radicals (either RO• or OH•), the H-transfer from the framework to ROOH followed by the adsorption of the intermediate on the metal active site through complexation with Mn(III). Figure 2.21 shows two concerted mechanism proposed by Corà and co-workers. The authors report that one of the two pathways is more stable (25 kJ mol^{-1}) than the other because of the more favourable stereochemistry of the ROOH adsorption (**G1** in figure 2.21) on the metal centre, where an H-bond interaction between the intermediate hydroxyl O atom and the framework is established.

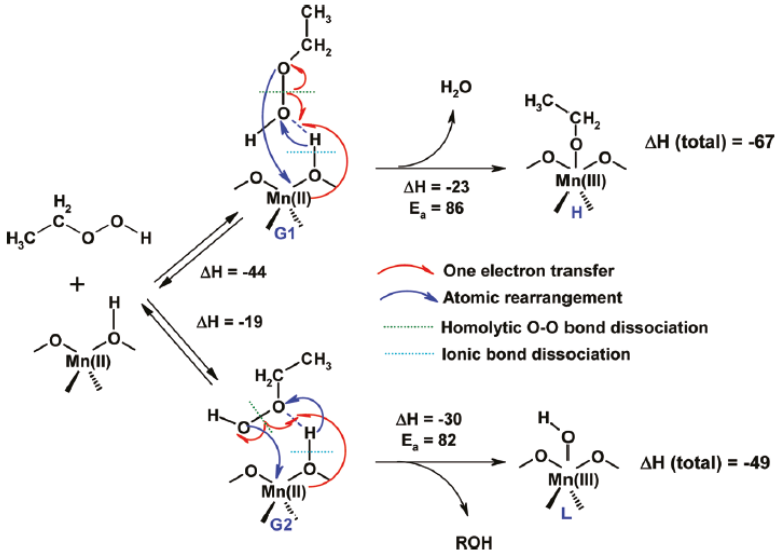

Figure 2.21. Two alternative routes for ROOH *decomposition* step leading to formation of water molecules and RO···Mn(III) complex (**H**), when **G1** intermediate occurs, and ROH and HO···Mn(III) complex (**L**), when **G2** intermediate occurs. Dashed dark-blue lines between H and O in the intermediates indicate H-bonding (figure take from reference 24).

This fact causes the corresponding Mn(III) complex, *i.e.* CH_3CH_2O···Mn(III), to be more dominant but still allows the complex HO···Mn(III) to be formed. The more exothermic *decomposition* path reflects the stability of the corresponding radical species, *i.e.* CH_3CH_2O• more stable than HO•. As mentioned earlier, the role of the metal centre is essential for the *decomposition* step. Corà and co-workers clearly describe how important the ability of Mn to undergo redox processes is for the H-transfer from the network to the newly formed O radical (with which Mn establishes a covalent bond) by the O–O bond dissociation. They also identify how fundamental

the Mn(III) Lewis acidity is in MnAPO materials in stabilising the incipient radicals, formed in the ROOH *decomposition*, through their complexation with the metal centre.

The formation of the Mn(III) complexes during the two possible *decomposition* paths just described, *i.e.* $CH_3CH_2O\cdots Mn(III)$ (or $RO\cdots Mn(III)$) and $HO\cdots Mn(III)$, initiates the *propagation* step (figure 2.22).[25] This reaction eventually leads to $CH_3CH_2OO\cdots Mn(III)$, or $ROO\cdots Mn(III)$, that is also formed in the *preactivation* step[23] and that can initiate further *propagation* processes.

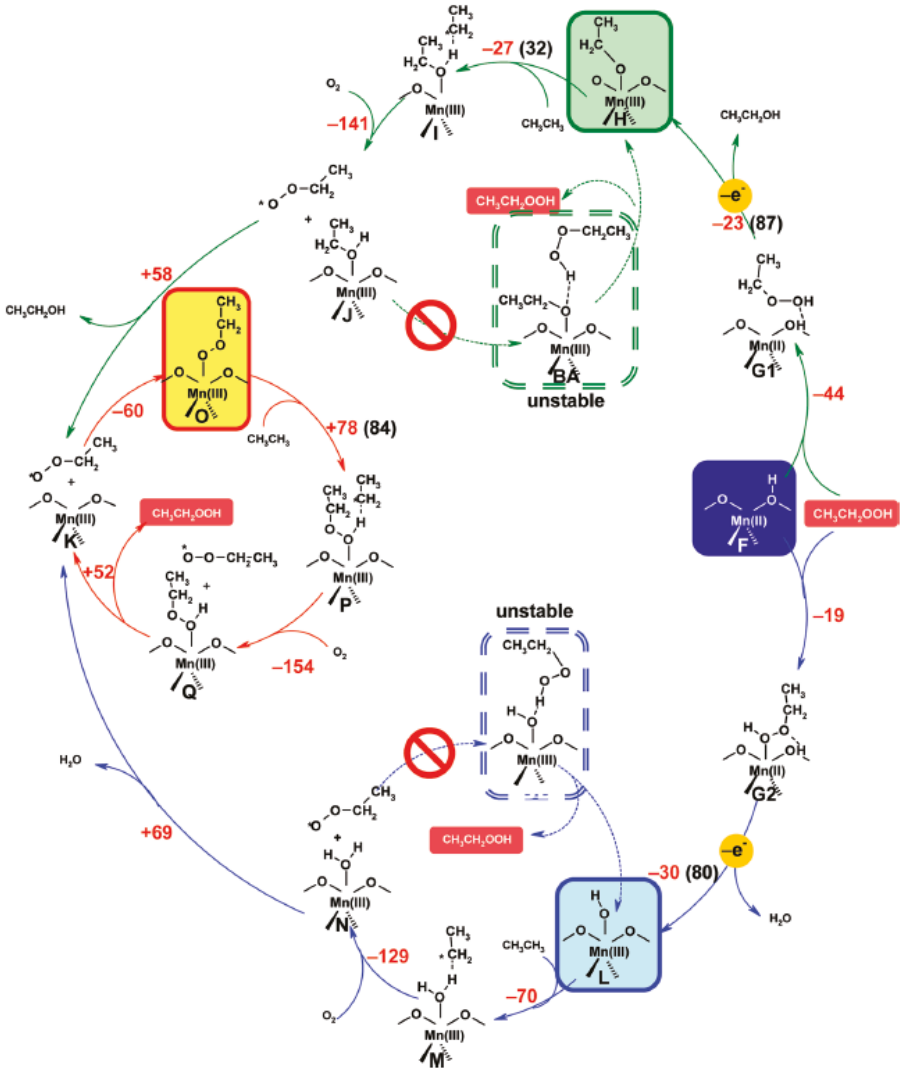

Figure 2.22. *Propagation* cycle scheme. Entalphies (red) and activation energies (back and bracketed) are in kJ mol^{-1} (figure taken from reference 25).

The final products formed during the *propagation* reaction are CH_3CH_2OH, H_2O (overall oxidation products) and CH_3CH_2OOH (ROOH) that allows the progress of further oxidation cycles.

The radical nature of the oxo-type ligands groups, *i.e.* CH_3CH_2O, HO and CH_3CH_2OO, allows the abstraction (homolysis) of H• from the substrate (CH_3CH_3 or RH) C–H bond to form XOH···Mn(III) (where X can either be CH_3CH_2, CH_3CH_2O or H). The ability of the oxo groups to abstract the H• radical follows the order HO···Mn(III) > CH_3CH_2O···Mn(III) > CH_3CH_2OO···Mn(III), which is the same order of the XO–H bond strength. This means in other words that the radical HO• is the least stable, and more prone to accept an electron to fill up its octet, the radical CH_3CH_2OO• is the most stable, and therefore less able to abstract the H• from the substrate, and the radical CH_3CH_2O• is somewhere in the middle of this scale of stability.

The stereospecific O_2 addition to the radical CH_3CH_2• (or R•) that follows the H-transfer produces a stable peroxo radical ROO•, which explains the exothermicity of this step. Then, the desorption of the ligand XOH from the metal centre allows ROO• to bind with Mn(III) forming the complex ROO···Mn(III) through which the *propagation* cycle can progress. The desorption energy order H_2O···Mn(III) > R(H)O ···Mn(III) > ROHO···Mn(III) reflects the ability (Lewis basicity) of the ligands to share electrons to form complexes with the metal centre. Finally, the desorption leads to the oxidation products, *i.e.* CH_3CH_2OH and H_2O.

Corà and co-workers also identified a *propagation* sub-cycle that represents the main source of ROOH for the overall reaction. The process appears to be 51 kJ mol^{-1} more favourable than the ROOH production pathway occurring during the *preactivation* reaction discussed earlier, and is initiated by the newly formed complex ROO···Mn(III).

The net transformation from reactant (**F** in figure 2.19 and 2.22) to product (**K** in figure 2.22) is summarised as Mn(II)(H) + ROOH + RH + O_2 → H_2O + ROH + ROO• + Mn(III) where the metal is oxidised and requires to be further reduced to complete the redox cycle and allow more cycles to occur.

The *regeneration*[26] of the active sites is the last step of the overall cycle. The species that are present at the active sites at this stage are the hydroperoxide (ROOH) and the

ROO···Mn(III) complex (**O** in figure 2.22). As already discussed, all the active sites are in the 2+ oxidation state and, in order for the cycle to progress, they require to be reduced to Mn(II) as only then the intermediate can be decomposed to products. Corà and co-workers describe two different pathways for the active sites regeneration. Initially, the ROO···Mn(III) complex is transformed into an aldehyde molecule and a HO···Mn(III) complex *via* an intramolecular H transfer from the methylene (–CH_2–) to the terminal peroxo O atom. The HO···Mn(III) complex reduction occurs by H abstraction from an organic species (substrate RH or an alcohol ROH). The radical H atom then releases the unpaired electron to the Mn(III) centre and binds, as an H^+ species, to the neighbouring O atom to the newly reduced metal centre Mn(II). This forms the active site for the *propagation* step[24] (**F** in figure 2.22) and a molecule of ethanol generated by the coupling between the formed alkyl radical and the OH originally present on the HO···Mn(III) complex. The accumulation of alcohol triggers the second reduction pathway *via* two consecutive H abstractions from ROH (CH_3CH_2OH). The first abstraction forms CH_3CH_2OOH when the travelling H• atom binds to the terminal O atom of the ligand CH_3CH_2OO in the ROO···Mn(III) complex, generating the CH_3CHO•OH radical species. The second abstraction from the latter generates the CH_3C=OH–OH···Mn(III) complex that will eventually release the aldehyde and **F**. The variation in alcohol/aldehyde ratio, which appears to be in good agreement with experimental observations, confirms the existence of the two proposed pathways that occur at different moments along the *regeneration* cycle.

2.3 Molybdenum Oxides (Molybdates)

Molybdenum (Mo) in oxides is present in various oxidation states leading to different structures and stoichiometry ratios. In this study, the most frequent Mo polymorph is considered α-MoO_3. The orthorhombic molybdate has a unit cell with dimensions (all in Å) equal to a = 3.9628, b = 13.855 and c = 3.6964. In α-MoO_3 molybdenum is fully oxidised to Mo(VI) and the atomistic structure, where Mo is almost octahedral (figure 2.23), is formed by two bi-layers parallel to the (010) plane (figure 2.24).

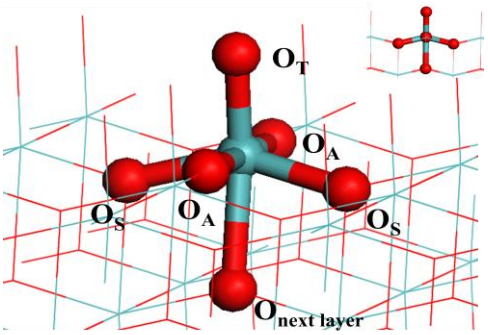

Figure 2.23. Structure of distorted MoO_6 octahedra forming each sublayer of the orthorhombic α-MoO_3 (010) surface: Mo is fully oxidized to Mo(VI). Three different types of oxygen atoms can be identified (key: Mo atom is blue, O atoms are red).

Each crystal plane, or surface, is uniquely identified by a set of numbers known as Miller indices (*hkl*): these quantify the inverse of the intercepts of plane considered with the main crystallographic axes of the solid under study. The indices assignment follows a specific set of rules that include indentifying the intercepts of the plane with the solid X, Y and Z axes, converting the coordinates of those intercepts in fractional coordinates and taking their reciprocal values.

The sublayers of the MoO_3 (010) atomistic structure are weakly bonded to each other by van der Waals interactions. Within each sublayer, three different types of oxygen atoms can be identified (figure 2.23): *asymmetric* (O_A) which is doubly coordinated and forms bonds with two Mo atoms of different lengths; *symmetric* (O_S), also called

bridging oxygen atom, is triply coordinated, forming equally long bonds with two Mo atoms on the same layer and a longer bond with a Mo atom sitting on the other sublayer; *terminal* (O_T) which is coordinated to a single Mo atom forming an Mo=O bond perpendicular to the (010) plane, the shortest of all Mo–O bonds: the O_T stretching frequency was calculated[27] using similar DFT methods to those used in this thesis and matches experimental values[28] both on the perfect and defective MoO_3 (010).

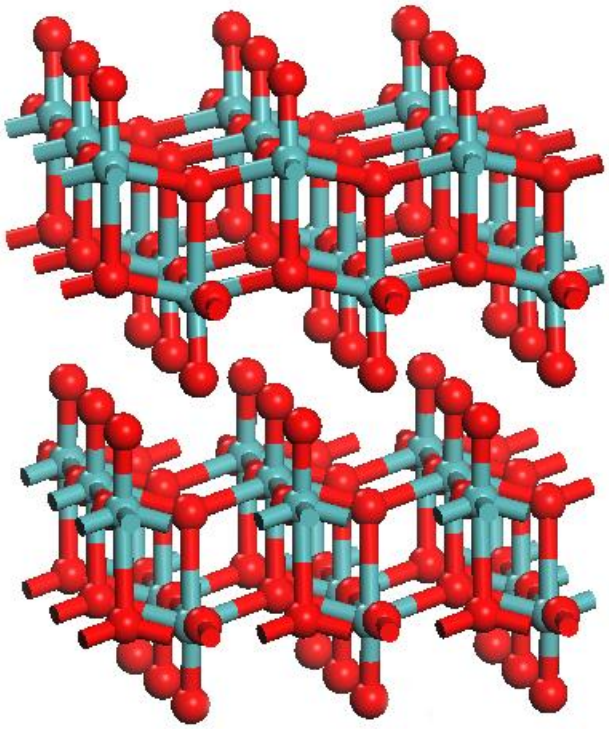

Figure 2.24. The two bi-layered structure of α-MoO_3 with the three types of oxygen indicated (key: Mo atom is blue, O atoms are red).

The flexibility of MoO_3 as a catalyst has been subject of a large number of studies in the last decades. The possibility of having different types[29] of active sites on MoO_3 structure is the result of a combination between Mo valence state and the environment surrounding Mo itself. The reduction of MoO_3 to MoO_2 (topotactic transition) generates temporary oxygen species which are active in complete oxidations. This is linked to the fact that the 1:1 physical mixture MoO_3/MoO_2 creates new interfaces which cause major crystal rearrangements following oxygen species loss. These rearrangements are often called crystallographic shears (CS) and

can be so extended to create planes of defects, called shear planes. During a catalytic reaction, shears can occur and get larger with the reaction time as the catalyst is reduced; when this happens, more ordered systems take shape and new phases are generated: molybdenum common suboxides $Mo_{18}O_{52}$ and Mo_8O_{23} occur generally when lattice oxygen plays a role in the reaction. Wang *et al.*[30] managed to identify successfully the two suboxides employing a combination of electron diffraction, High-Resolution Transmission Electron Microscopy (HRTEM) and image simulation.

The presence of two different M–O sites on MoO_3(110), namely terminal (Mo=O) and 3-folded (Mo–O–Mo), is shown for even thin films of MoO_3 by the results of Queeney and Friend.[31,32] They managed to demonstrate that during CH_4 partial oxidation, methoxy never deposits oxygen from C–O breaking on Mo=O sites but it reacts at highly coordinated oxygen sites (Mo–O–Mo). Infrared spectroscopy identified two ν(Mo=^{18}O) peaks at 944 and 965 cm^{-1} after MoO_3(110) was oxidized with $^{18}O_2$ (figure 2.25), but no peaks at 992 and 1016 cm^{-1} were found after reaction of $CH_3{}^{16}OH$ on the same surface. After surface high temperature oxidation, the system was being cooled down maintaining an O_2 background pressure to populate the Mo=O sites: at this point only a ν(Mo=O) peak at 996 cm^{-1} was identified.

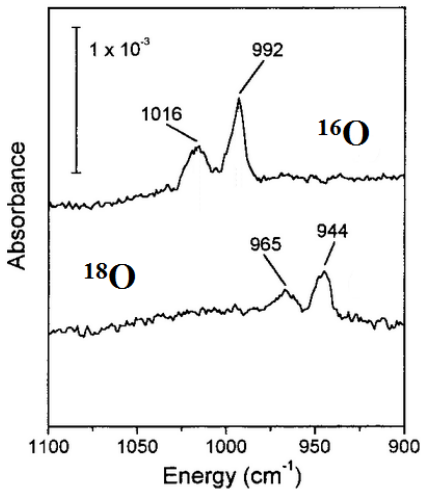

Figure 2.25. Infrared spectra ν(Mo=^{18}O) and ν(Mo=^{16}O) peaks (stretching modes) for isotopically labelled perfect (*left)* and defective (*right*) MoO_3(110) surface (figure taken from reference 25).

Papakondylis and Sautet[33] carried out an *ab initio* study of α-MoO_3 periodic crystal structure, concluding that the solid is composed of basic units where MoO_4 tetrahedra form $(MoO_3)_x$ chains by sharing O atoms and these units are held together by electrostatic forces; furthermore, they found that MoO_3(010) surface contains pentacoordinated Mo atoms with Lewis acid character. Finally, they carried out a study over H_2O and CO molecules adsorbing on the surface Mo centres that described interactions of electrostatic nature.

Almost at the same time, another *ab initio* Hartree-Fock (HF) study by Corà *et al.*[34] described α-MoO_3 structural and ground-state electronic structure reporting that in the MoO_6 octahedron there is a dependency between the Mo–O interaction nature and equilibrium distance, where the former varies from strongly covalent (shortest bond) to mainly ionic interaction (longest bond).

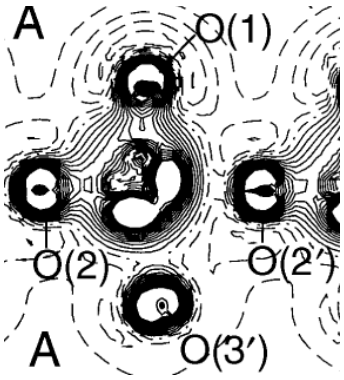

Figure 2.26. Difference electronic charge density map for an isolated MoO_6 octahedron (solid minus isolated Mo_6^+ and O_2^+ ions: Mo is the central atom contained in the crystallographic plane shown and its vertices on the plane are labelled O(1), O(2'), O(3') and O(2). Positive, negative and zero difference are continuous, dashed and dotted-lines, respectively. The interval between the isodensity lines is 0.05 a.u. (electrons a_0^{-3}). "A" denotes parts of the interlayer space. The map extends beyond the central atom (figure taken from reference 28).

The degree of covalence is described with the Mulliken electronic analysis and electron density maps: the maps confirm the asymmetric character of the oxygen atoms O_A (figure 2.23) showing asymmetry of the electronic density between the relevant O_A atoms (O(2) and O(2') in figure 2.26) and the central Mo atom; equally,

the double bond character is highlighted by the largest electron density between Mo and the terminal oxygen atom O_T (O(1) in figure 2.26).

Figure 2.26 also shows white gaps in correspondence of the A spaces: this is due to a lack of electronic density accumulation which corresponds to a minimum in energy as a function of the interlayer distance, indicator of a weak Coulombic force between the layers, both at correlated and HF level. This is a known limitation of the Density Functional Theory (DFT) to treat these weak interactions between layers (chapter 6).

Friend *et al.*[35] employed LDA DFT to investigate MoO_3(010) surface point defects reporting that no significant surface change is followed by the removal of a terminal oxygen atom O_T. The creation of O_T vacancy generated two new states in the energy spectrum of MoO_3(010) surface: a nonbonding state, namely d_{xz}, and a "dangling" d_{z^2} state in the conduction band, both localized on the Mo that was bonded to the removed O_T, with the latter being perpendicular to the surface.

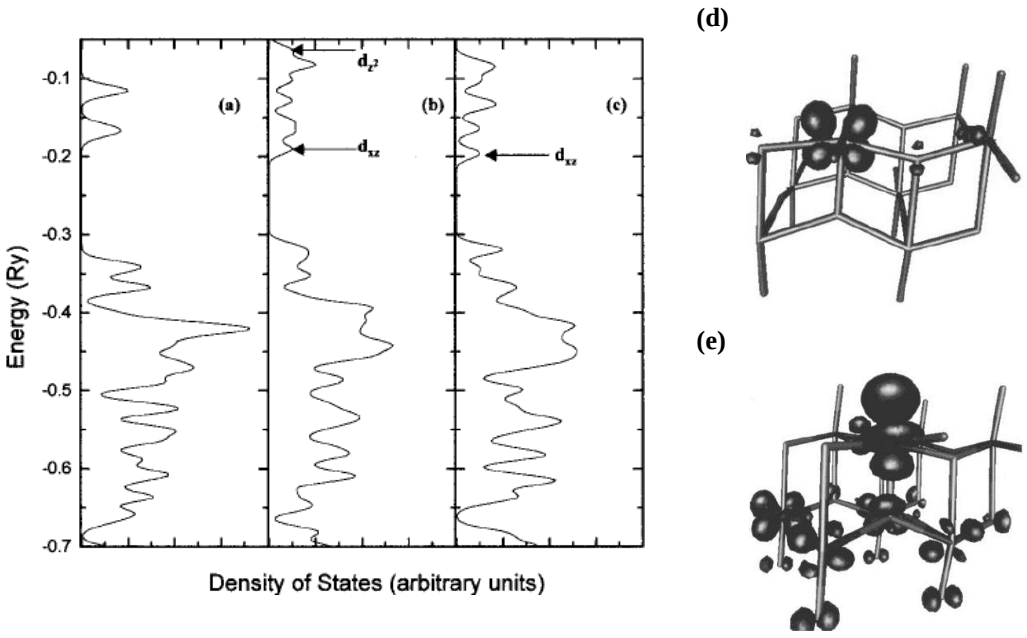

Figure 2.27. Density of States: plots of only those states near the band gap are shown. (a) "Perfect" MoO_3(010) surface; (b) MoO_3(010) surface with a (2×2) array of O_T vacancies: d_{xz} and d_{z^2} indicate the energy of those orbitals related to the vacancy creation; (c) hydrogen atom adsorbed on the O_T vacancy. Isoelectronic plots of vacancy-localized states: (d) d_{xz} and (e) d_{z^2} orbitals (figure taken from reference 29).

Figure 2.27(a) shows the density of states calculated for the perfect (010) surface, while the new features associated with the removal of a O_T are observable in figure 2.27(b) and are plotted in figure 2.27(d) and (e), showing the large contribution from the d_{xz} and d_{z^2} orbitals, respectively, to the concerned crystal orbitals, which allows the states assignments in the DOS diagram shown in figure 2.27(b). The energy required to remove an O_T (10.1 eV) was calculated by deducting the sum of defective surface and that of an oxygen atom to the total energy. The appearance of the d_{xz} state when an H atom is added to an O_T can also be observed (figure 2.27(c)) within the same area to that for the defect formation.

A DFT study of non periodic MoO_3 structures was carried out by Witko *et al.*[36] in 1996: the models they employed are a series of finite sections (up to $Mo_7O_{30}H_{18}$) of the ideal MoO_3 surface saturated with hydrogen atoms positioned at the edges of each model, in order to obtain successful cluster embedding. Results showed that, other than the global surface geometry/orientation, it is the local atomic environment (atomic arrangement) to be the main reason for the difference in electronic structure between the (010) and (001) surfaces; consistent to this, the local atom charging and binding properties are surface-independent. Furthermore, they identified large negative minima in correspondence of the O_T centres in the electrostatic potential sourced by the cluster charge distribution but found no minimum above the bare Mo metal centres. In 1999, Witko *et al.*[37] studied electronic structure and adsorption on MoO_3(010) and (001) surfaces with the same method employed three years before but neglected the cluster surface relaxation, which was instead observed two years after by Friend *et al.*[29] In 2001, Witko and co-workers carried out a DFT study[38] on embedded clusters of the MoO_3(010) surface with as many as fifteen Mo centres, *i.e.* $Mo_{15}O_{56}H_{22}$ (figure 2.28), and compared the results with experiments of ultraviolet photoemission (UPS).

The edges of the $Mo_{15}O_{56}H_{22}$ cluster are saturated with H atoms to satisfy the oxygen atom valency corresponding to that on the surface, based on the type and distance of each O atom from the neglected Mo centres.

The energy required for the defect formation reported by Witko is between 6.8 and 7.6 eV for the removal of all the O surface atoms on MoO_3(010) surface: these

values though, as already mentioned, are missing of a further stabilization of 3.3 eV[29] due to the surface relaxation (neglected in Witko's clusters) occurring following the defect generation.

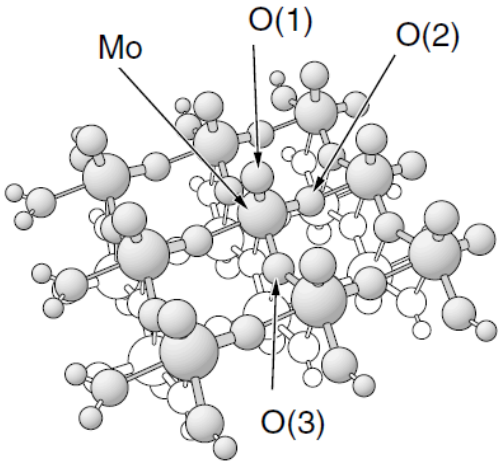

Figure 2.28. Structure of the $Mo_{15}O_{56}H_{22}$ cluster modelling a bi-layered section of the MoO_3(010) surface. Cluster atoms of the top (bottom) part are shown as shaded (white) balls with size decreasing in the sequence Mo, O and H. The central Mo atom and its three vicinal non-equivalent surface O centres are labelled accordingly, *i.e.* O(1-3), where O(1) is a terminal, O(2) is an asymmetric and O(3) is a symmetric oxygen (figure taken from reference 32).

Witko *et al.* published two papers in 2004 on the re-oxidation of transition metal oxides MoO_3 and V_2O_5:[39,40] the findings describe the re-oxidation via molecular oxygen being a localized process and that the surface defects tend to be re-oxidized either through exchange of gaseous oxygen or via diffusion of bulk O atoms. Also, it was suggested that adsorption of H atoms on the surface leading to both hydroxyls and water species, could facilitate generation of surface defects through the relatively easy desorption of those. The O_2 adsorption on the defects was preferred on a parallel mode over the perpendicular: the adsorbed molecule was activated showing an O–O bond elongated with respect to the gas phase, with a decreased bond order. Comparison between MoO_3(010) and V_2O_5(010), in connection with terminal and symmetric O centres, showed a much larger rearrangement for the former surface,[33] unlike what was found by Friend *et al.*[29] that observed no significant relaxation following the terminal oxygen atom removal.

In the monoclinic iron molybdate (α-$Fe_2(MoO_4)_3$) form molybdenum is fully oxidised as Mo(VI) and its symmetry is tetrahedral, while Fe(III) is octahedral (see figure 2.29). The bulk phase is fairly complex, showing different environments characterized by at least five sets of Mo–O and Fe–O bond lengths.

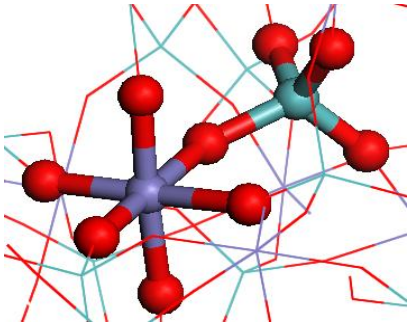

Figure 2.29. Structure of the MoO_4 tetrahedra (O is red, Mo is blue) where Mo is fully oxidised as Mo(VI), linked to a FeO_6 octahedra (Fe purple and is Fe(III)) in monoclinic α-$Fe_2(MoO_4)_3$.

Iron molybdate is one of the main catalysts employed in industry for the oxidation of methanol to formaldehyde. Hutchings *et al.*[41] studied this catalyst in C_7–C_{12} linear alkanes aerobic gas phase conversion. The surface is composed of two phases that form during the catalyst's synthesis: $Fe_2(MoO_4)_3$ is enriched in MoO_3 (molybdate/iron overall ratio 4:1) whose segregation increases the reaction selectivity via creation of adsorption sites by decreasing the surface acidity. The reaction follows the Mars-van Krevelen redox mechanism where the catalyst lattice supplies the selective oxygen (oxidizing agent) and the gas phase re-establishes the catalyst initial conditions by adsorption of gaseous O_2 at the defect.

The reaction of decane was followed at 460°C and deactivation of the catalyst was observed after 3 hours of its use. The reaction was expected to give partial oxidation products, namely C_{10} oxygenates. Instead, major products were isomers of decene, C_6–C_{10} aromatic hydrocarbons and CO_2; ~7% of production was represented by CO, C_1–C_7 hydrocarbons/oxygenates and the unexpected oxygenated aromatics. Further deactivation of the catalyst was observed when feed of gaseous O_2 was interrupted to test the relative importance in the reaction of electrophilic oxygen species compared to those selective short-lived oxygen intermediates generated by the $O_2 \rightarrow O^{2-}$ process. It was established that the combination between catalyst acid sites

progressive deactivation due to carbon deposition and lattice oxide ions loss due to their employment in the reaction, caused a structural transformation of the catalyst phase composition that from $Fe_2(MoO_4)_3$ and MoO_3 became $FeMoO_4$, MoO_2 and Mo_4O_{11} with decreased catalytic activity. The same reaction run at 350°C showed minor loss of molybdenum oxide from the catalyst surface (molybdate/iron overall ratio 4:2) but overall no major changes in the catalyst phases were detected. In these conditions though a completely different product distribution was detected: the selectivity to oxygenated aromatics was five times higher than at 460°C while that to aromatic hydrocarbons was slightly decreased, which suggested the oxygen insertion at the activated intermediates occurred before their desorption from the surface. As for the reaction at 460°C, the catalyst phase composition changed in the first hours of use to the same reduced phases described earlier, with presence of Fe^{2+} and Mo^{4+} on the surface.

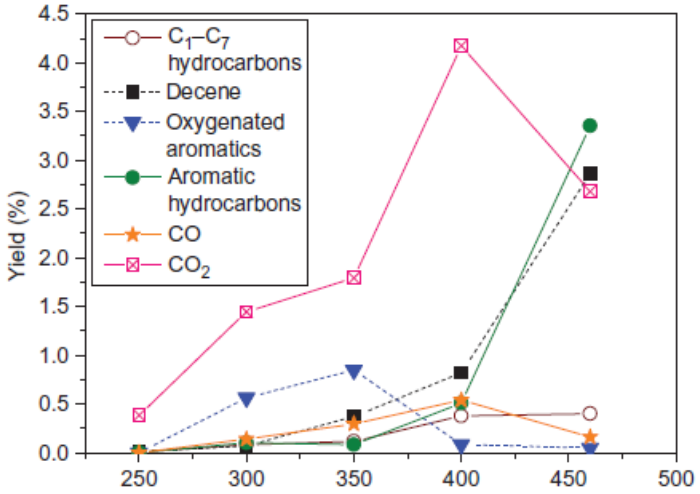

Figure 2.30. Yields of major products C_7–C_{12} linear alkanes oxidation catalyzed by iron molybdate are in function of temperature and of the catalyst phase composition: $Fe_2(MoO_4)_3$–MoO_3 sources non-selective electrophilic oxygen species (O_2^-, O_2^{2-} and O^-) at lower temperatures while $FeMoO_4$–MoO_2–Mo_4O_{11} supplies selective lattice oxide ions (O^{2-}) at higher temperatures (figure taken from reference 35).

The indications provided by the results at 350°C and 460°C suggested a possible link between product distribution and catalyst phase composition and surface structure. For this reason, the temperature influence of the catalyst performance was probed and the results are shown in figure 2.30. At low temperature, the electrophilic adsorbed oxygen species (non selective oxygen) increasingly favour the production

of oxygenated aromatics and CO_2: yield of both species increases with the temperature up to 350°C where the aromatics peak and CO_2 suddenly increases steeply to peak at 400°C, which is an indication of the competition between complete and partial oxidations or, in other words, between non-selective and selective oxygen species. At 400°C, the catalyst undergoes the discussed surface transformations, lattice (selective) oxygen ions become more available and partial oxidation of decane to decene and production of aromatic hydrocarbons are favoured.

The two important factors identified in the two previous sections are the zeolites *shape selectivity* and the oxidation catalysis involving a *redox* cycle of metal centres such as molybdenum. Reactions inside zeolites are forced to occur within a constraint environment and this element seems to be fundamental in driving the regioselectivity towards terminal products. Instead on molybdenum oxide active catalysts, the importance of a surface defect is fundamental for the *redox* process to occur. Removal of a surface O atom from the lattice *via* reduction creates the defect that triggers the cycle.

Therefore, one of the goals set for the work presented in this thesis is making contact with the experimental results[19] on oxidations of alkanes within zeolites. Once this contact is established, a further look into the basic mechanism of the reaction at zeolite supported metal centres will be made, highlighting the geometrical features that characterize the substrate adsorption onto the internal zeolitic walls and describing the chemistry behind the role of the zeolite metal centre within the reaction. For the molybdenum oxides, the goal is to explore the creation of the defect on the surface and describe the main steps of the *redox* cycle which involves a radical mechanism, with special focus on those steps where the radical species are generated. The molybdenum oxide catalyst modelled here in reality is formed by two different components that in this study will be investigated separately to break down and indentify their individual characteristics.

References

[1] H. Basch, K. Mogi, D. G. Musaev, K. Morokuma *J. Am. Chem. Soc.*, **121**, 7249 (1999).
[2] F. P. Guengerich *Chem. Res. Toxicol.*, **14**(6), 611 (2001).
[3] T. Sugino, A. Kido, N. Azuma, A. Ueno, J. Udagawa *J. Catal.*, **190**, 118 (2000).
[4] J. S. J. Hargreaves, G. J. Hutchings, R. W. Joyner, S. H. Taylor *Chem. Commun.*, 523 (1996).
[5] K. Otsuka, Y. Wang, I. Yamanaka, A. Morikawa *J. Chem. Soc., Faraday Trans.*, **89**, 4225 (1993).
[6] J. H. Lunsford *Catal. Rev. Sci. Eng.*, **8**, 135 (1973).
[7] M. Che, A. J. Tench *Adv.Catal.*, **31**, 78 (1982).
[8] M. Che, A. J. Tench *Adv.Catal.*, **32**, 1 (1983).
[9] K. Aika, J. H. Lunsford *J. Phys. Chem.*, **81**, 1393 (1977).
[10] K. Aika, J. H. Lunsford *J. Phys. Chem.*, **82**, 1794 (1978).
[11] M. R. Smith, U. S. Ozkan *J. Catal.*, **141**, 124 (1993).
[12] J. M. Thomas, R. Raja, G. Sankar, R. G. Bell *Nature*, **398**, 227 (1999).
[13] J. A. Kerr *Chem. Rev.*, **66**, 465-498 (1966).
[14] J. Chen, J. M. Thomas *J. Chem. Soc. Chem. Commun.*, 603-604 (1994).
[15] K. Tanabe, W. F. Hölderich *Appl. Catal. A*, **181**, 399-434 (1999).
[16] A. F. Cronstedt *Kongl Vetenskaps Acad. Handl. Stockholm*, **17,** 120 (1756).
[17] F. A. Mumpton *Proc. Natl. Acad. Sci. USA*, **96,** 3463-3470 (1999).
[18] Ch. Baerlocher and L.B. McCusker, Database of Zeolite Structures: http://www.iza-structure.org/databases/.
[19] D. H. Olson, G. T. Kokotailo, S. L. Lawton, W. M. Meier *J. Phys. Chem.*, **85**, 2238 (1981).
[20] D. W. Breck, "Zeolites Molecular Sieves", Wiley: New York, 636-7 (1974).
[21] B.-Z. Zhan, B. Modén, J. Dakka, J. G. Santiesteban, E. Iglesia *J. Cat.*, **245,** 316–325 (2007).
[22] F. Corà, L. Gómez-Hortigüela, C. Richard, A. Catlow *Proc. R. Soc. A*, **468**, 2053-2069 (2012).
[23] L. Gómez-Hortigüela, F. Corà, C. Richard, A. Catlow *ACS Catal.*, **1**, 18-28 (2001).
[24] L. Gómez-Hortigüela, F. Corà, C. Richard, A. Catlow *ACS Catal.*, **1**, 945-955 (2001).
[25] L. Gómez-Hortigüela, F. Corà, C. Richard, A. Catlow *ACS Catal.*, **1**, 1487-1497 (2001).
[26] L. Gómez-Hortigüela, F. Corà, C. Richard, A. Catlow *ACS Catal.*, **1**, 1475-1486 (2001).
[27] R. Coquet, D. J. Willock *Phys. Chem. Chem. Phys.*, **7**, 3819-3828 (2005).
[28] K.T. Queeney, C.M. Friend *J. Phys. Chem. B*, **104,** 409-415 (2000).
[29] J. Haber, E. Lalik *Catal. Today***, 33**, 119-137 (1997).
[30] D. Wang, S. Dangshen, R. Schlögl *Cryst. Res. Technol.*, **38**, 153-159 (2003).
[31] K. T. Queeney, C. M. Friend *J. Phys. Chem. B*, **102**, 5178-5181 (1998).
[32] K. T. Queeney, C. M. Friend *J. Phys. Chem. B*, **104**, 409-415 (2000).
[33] A. Papakondylis, P. Sautet *J. Phys. Chem.*, **100**, 10681 (1996).
[34] F. Corà, A. Patel, N. M. Harrison, R. Dovesi, C. R. A. Catlow *J. Mater. Chem.*, **7**, 959 (1997).
[35] M. Chen, C. M. Friend, F. Kaxiras *J. Am. Chem. Soc.*, **123**, 2224 (2001).
[36] A. Michalak, K. Hermann, M. Witko *Surf. Sci.*, **366**, 323-336 (1996).
[37] K. Hermann, M. Witko, A. Michalak *Catal. Today*, **50**, 567-577 (1999).
[38] R. Tokarz-Sobieraj, K. Hermann, M. Witko, A. Blume, G. Mestle, R. Schlögl *Surf. Sci.*, **489**, 107-125 (2001).
[39] M. Witko, R. Tokarz-Sobieraj *Catal. Today*, **91-92**, 171-176 (2004).

[40] R. Tokarz-Sobieraj, R. Grybos, M. Witko, K. Hermann *Collect. Czech. Chem. Commun.*, **69**, 121-139 (2004).
[41] G. J. Hutchings, S. Pradhan, J. K. Bartley, D. Bethell, A. F. Carley, M. Conte, S. Golunski, M. P. House, R. L. Jenkins, R. Lloyd *Nature Chem.*, **4**, 134-139 (2012).

3. Theoretical Background

This section describes the main theoretical approaches used in this work: Metropolis Monte Carlo random methods (MC), Density Functional Theory (DFT), geometry optimizers, vibrational frequency calculation and density of states and implementation of MC and DFT in those codes employed within this study.

3.1 Monte Carlo

Monte Carlo methods are simulation techniques that randomly sample points in phase space to determine the average of some property *X* that depends on the positions of those points in phase space. In molecular systems, a Monte Carlo simulation generates different configurations of a molecule by randomly modifying the coordinates of the atoms and then selecting the generated configurations on the basis of their importance.

The evaluation of the integral $\langle X \rangle = \int X(r)P(r)dr$ can in principle provide the average value of the property *X* sought, although the integral itself cannot be solved analytically. Within the configuration phase space, the integral can sample the average potential energy $\langle E(r^N) \rangle$ (*N* number of atoms). The expression of the integral contains the probability function $P(r^N) = e^{(-E(r^N)/k_BT)} / Z$ of each configuration where $Z = \int e^{(-E(r^N)/k_BT)} dr^N$ is the configurational integral, or partition function of the system.

Both the integral $\langle X \rangle$ and the probability function could either be calculated numerically, although this would represent an unfeasible task for the hugely large number of calculations, or they could be evaluated by sampling configurations representative of all the states of the system. The latter approach, in its most basic of forms, would involve making random changes to the system coordinates, evaluate the energy corresponding to each move and estimate $X(r)P(r)$ to find $\langle X \rangle$. This

approach tough does not sample properly. In phase space the majority of molecular configurations do not contribute to the average because of the small Boltzmann factor associated to them: they are high energy configurations because the atoms forming the molecules clash or even overlap. Instead, the configurations that do contribute and are observable in nature as phases, *i.e.* liquid, solid, etc., are those having low energy, and they represent a small minority. Therefore, the "basic" form of Monte Carlo methods only samples high energy configurations as dictated by the Boltzmann factor. An alternative to this sampling regime is represented by what is known as *importance sampling* technique, which follows a different approach: low energy (overlapping-free) configurations, when generated, are assigned higher Boltzmann weights and then both low and high energy conformations are counted equally. This "biased" procedure allows low energy configurations to be rated as important and therefore to be sampled. This technique is at the basis of the *Metropolis* Monte Carlo[1] (MC) methods.

Each sampled configuration represents the starting point for the MC iteration that follows it, where a random change in atom(s) coordinates is made. The acceptance rule for each step is (here too) based on an energy evaluation: if the new geometry is more stable than the old geometry ($\Delta E < 0$, change decreases energy), the former is sampled and, again, represents the starting point for the step that follows. Instead, if the new geometry is less stable ($\Delta E > 0$, change increases energy), a random number between 0 and 1 is generated and tested against the probability $e^{-\Delta E / k_B T}$ (Boltzmann factor) for the change to occur: if $e^{-\Delta E / k_B T}$ is larger than the random number, the new geometry is accepted, while rejection occurs if the random number is larger, in which case a further random change to the initial geometry is performed (see expression 3.1) and the original structure properties such as the energy are included again in any averages being accumulated.

$$e^{-\Delta E / k_B T} > rand(0,1) \qquad 3.1$$

An important condition the configuration ensemble generation has to obey, to avoid collecting artefacts, is the *detailed balance* condition: all random coordinate

modifications are required to be reversible so that the probability of making a change in one direction is equal to the probability of undoing the move.

3.2 Density Functional Theory

3.2.1 DFT

In 1960's Kohn, Hohenberg and Sham[2,3] introduced and developed the Density Functional Theory[4] (DFT), a method built on the concept of a single particle electron density *ρ(r)* that, if run with modern functionals, provides accurate results at low computational costs, if compared with the much more complicated Schrödinger equations, as consistently shown in several years of its employment within studies of electronic structures.

The exact Hamiltonian ($\hat{H}$) of an *N*-electron system for the ground state can be written as in 3.2.

$$\hat{H} = \hat{T} + \hat{V} + \hat{U} = \sum_{i=1}^{N}\left(-\frac{1}{2}\nabla_i^2\right) + \sum_{i=1}^{N} v(\vec{r}_i) + \sum_{i<j}^{N}\frac{1}{r_{ij}} \qquad 3.2$$

The equation includes the operators of kinetic ($\hat{T}$), potential ($\hat{V}$) and internal ($\hat{U}$) energy; the right hand side of equation 3.2, shows the exact form of each of the operators: kinetic energy $-\frac{1}{2}\nabla_i^2$ (atomic units) for the electron *i*, the interaction energy $\frac{1}{r_{ij}}$ for *i* and *j* electrons and the external potential $v(\vec{r})$, which is imposed being a constant and under which influence the electrons move.

The first Hohenberg-Kohn (H-K) theorem (see expression 3.3) states that the external potential $v(\vec{r})$ (therefore total energy) is a functional of the electron density $\rho(\vec{r})$. The expression 3.3 also shows that a unique universal functional, $F[\rho(\vec{r})]$, which therefore does not depend on $v(\vec{r})$, exists, although its explicit formula is not known.

$$E[\rho(r)] = F[\rho(\vec{r})] + \int v(\vec{r})\rho(\vec{r})d\vec{r} \qquad 3.3$$

The Kohn-Sham (K-S) theorem states that in a fictitious system where electrons do not interact, the value of $F[\rho(\vec{r})]$ minimizing the expression 3.3, with respect to $\rho(\vec{r})$, is equal to $\left\langle \Psi \,|\, (\hat{T}+\hat{U}) \,|\, \Psi \right\rangle$ with Ψ (psi) being the system wavefunction.

Although the H-K theorems have made a rather important step towards the introduction of an alternative (and far simpler) method to the Schrödinger wavefunction, their formulation does not include the ground state density of a many-electron (real) system to be computed by DFT. On the contrary, the K-S theorem does allow the DFT practical use: the density obtained solving this alternative system devised by Kohn and Sham in 1965, made of many one-electron systems, can be known because it corresponds to that of the ground state. In the K-S system the kinetic energy functional, *T(ρ)*, is partitioned in one term taking care of the non-interacting part, *T(Ψ)*, that can be known exactly, and a second term, V_{XC}, called exchange-correlation term. The introduction of the non-interacting system has pros and cons: although it delivers a computational accurate response, the nature of its approximation does increase the Hamiltonian complexity as *H* is not just a function of the density anymore, *H(ρ)*, but also depends on the system wavefunction, *H(ρ, Ψ)*.

The K-S total energy for the non-interacting system is partitioned in three terms, two of which representing its larger part: the kinetic (non-local) energy and the Hartree Coulomb (classical electrostatic) energy, which can be known exactly. The third term is the exchange-correlation energy, $E_{XC}[\rho(\vec{r})]$, and is calculated by approximations. For this purpose, a homogeneous electron gas system is considered: $E_{XC}[\rho(\vec{r})]$ is calculated by integration of infinitesimal density changes which eliminate the gradient terms, as shown in expression 3.4 (ε_{XC} function of ρ):

$$E_{XC}[\rho] = \int \varepsilon_{XC}(\rho(\vec{r}))d\vec{r} \qquad 3.4$$

The K-S equations can be obtained by resolving the *N* one-electron Schrödinger equations (expression 3.5), or as they are also called, K-S orbital equations in their canonical form:

$$\left\{-\frac{1}{2}\nabla^2 + \nu_{eff}\right\}\psi_i(\vec{r}) = \varepsilon_i\psi_i(\vec{r}) \qquad 3.5$$

with $\nu_{eff}(\vec{r}) = \nu(\vec{r}) + \int \frac{\rho(\vec{r})}{|\vec{r}+\vec{r}'|}d\vec{r} + \nu_{XC}(\vec{r})$ being the effective potential where $\int \frac{\rho(\vec{r})}{|\vec{r}+\vec{r}'|}d\vec{r}$ is the Coulomb potential and $\nu_{XC}(\vec{r}) = \frac{\partial(\rho(\vec{r})\varepsilon_{XC}(\rho))}{\partial\rho(\vec{r})}$ is the exchange-correlation potential, both unknown.

In order to resolve these equations and construct the effective potential $\nu_{eff}(\vec{r})$, the exchange-correlation potential $\nu_{XC}(\vec{r})$ is obtained via iterative calculation of $E_{XC}[\rho(\vec{r})]$, as described for expression 3.4, since $\nu_{XC}(\vec{r})$ is also equal to $\frac{\partial(E_{XC}[\rho(\vec{r})])}{\partial\rho(\vec{r})}$.

Therefore, the expression of the total energy can now be formulated as follows:

$$E^{LDA}[\rho] = T_s[\rho] + E_{ext}[\rho] + E_{coul}[\rho] + E_{XC}[\rho] \qquad 3.6$$

where $T_s(\rho)$ (kinetic energy of non-interacting electron gas of density ρ) can be expressed as K-S orbital eigenvalues, $E_{est}[\rho]$ is the external potential energy and $E_{coul}[\rho]$ is the Coulomb energy (electrostatic Hartree energy of the electrons), as shown explicitly in 3.7:

$$E^{LDA}[\rho] = T_s[\rho] + \int v(\vec{r})\rho(\vec{r})d\vec{r} + \frac{1}{2}\iint \frac{\rho(\vec{r}')\rho(\vec{r})}{|\vec{r}-\vec{r}'|}d\vec{r}'d\vec{r} + E_{XC}[\rho] \qquad 3.7$$

Becke[5] observed that the adiabatic correction formula for the exchange-correlation energy E_{XC} expression[6] could be used as a platform to introduce a new type of functional. The formula he based his observations on is shown in 3.8:

$$E_{XC} = \int_0^1 U^\lambda d\lambda \cong \frac{1}{2}U^0 + \frac{1}{2}U^1 \qquad 3.8$$

The inter-electronic coupling-strength parameter, λ, acts as a switch for the interacting nature of the system: $\lambda = 0$ for a KS system where particles are non-interacting (Hartree-Fock approach), and $\lambda = 1$ for a fully interacting system with which a local spin-density approximation approach can be employed. On the basis of these observations, Becke introduced the half-and-half functional (expression 3.9) where the exchange-correlation term $E_{XC,\,\lambda=1}^{DF}$ can be computed via a density functional approximation, *i.e.* LDA:

$$E_{XC} = \frac{1}{2} E_X^{HF} + \frac{1}{2} E_{XC,\,\lambda=1}^{DF} \qquad 3.9$$

What Becke did with his functional was introducing a new class of hybrid approaches that attempt to combine exact (HF) exchange functionals to GGAs functional, as the general expression is shown in 3.10:

$$E_{XC}^{hybrid} = \alpha(E_X^{HF} - E_X^{GGA}) + E_{XC}^{GGA} \qquad 3.10$$

The semi-empirical parameter α represents the amount of exact-exchange ratio used in 3.10. Hybrid functionals enhance GGAs functionals' ability to describe molecular properties but produce poor results when combined with planewave basis sets in calculations over periodic solid systems.

3.2.2 DFT+U

The combination of DFT and the Hamiltonian of the Hubbard model for the Coulomb repulsion and exchange interaction yields a correction (DFT+U) to the method to overcome its inability to properly describe strongly correlated systems containing metals with semi-filled *d* and *f* shells. In particular, DFT underestimates the total energy therefore the correction applied has to be a positive contribution. This is achieved by employing a rotational invariant energy functional[7] (expression 3.11):

$$E_{DFT+U} = E_{DFT} + \frac{U-J}{2}\sum_{\sigma} T_r[\rho^{\sigma} - \rho^{\sigma}\rho^{\sigma}] \qquad 3.11$$

The correction takes care of the introduction of an extra electron in the system and of the effect this event has on total energy (Hubbard parameter,[8] *U*), on screen exchange (*J*) and on the *d* electrons on-site density matrix (ρ^{σ}).
The Hubbard parameter *U*, which is spherically averaged, is function of the spatial extent of the wave functions and of the screening while *J* is a constant (~1 eV) approximating the Stoner exchange parameter. For $U - J = 0$, no correction to the DFT energy is made ($E_{DFT+U} = E_{DFT}$); instead, when $U - J > 0$ the correction is applied ($E_{DFT+U} > E_{DFT}$): the term added to E_{DFT} is positive because $\rho^{\sigma} - \rho^{\sigma}\rho^{\sigma}$ is already so $(\rho^{\sigma} - \rho^{\sigma}\rho^{\sigma} = \sum_i (\upsilon_i^{\sigma} - \upsilon_i^{\sigma 2}) > 0)$ as the interval where υ_i (on-site occupancy matrix eigenvalue) varies is $0 < \upsilon_i < 1$.

3.2.3 Pseudopotentials

As already described, the use of DFT reduces computational costs. A further reduction is provided by employing *pseudopotentials*. Chemical reactions, and more in general physical processes, take place between the valence electrons of the chemical species, which are those electrons on the "front line" (outer shell) that allow breakage or formation of bonds between atoms to occur. Since the core electrons instead play an indirect role in the reactions as they are "buried" by the valence levels, therefore are inert, pseudopotentials treat them implicitly. This so called frozen-core approximation and is of great importance, especially considering metal systems for which there are many core electrons like molybdenum.

$$\hat{V}^{ps} = \hat{V} + (\varepsilon - \hat{T} - \hat{V})\hat{P} \qquad 3.12$$

The pseudopotential is angular momentum dependent and accounts for quantum-mechanical interactions between valence electrons and core, namely nuclear

Coulomb attraction screened by the core electrons, Pauli repulsion and exchange correlation between core and electrons.

The core wave functions are not calculated and the core effect over the atoms is treated implicitly, leaving only the valence eigenvalues to be calculated (pseudo-Schrödinger equation). This approach is advantageous when, for example, the bulk material is studied: construction of the pseudopotential is carried out through a calculation over all the electrons of one-atom system and is used to calculate the bulk properties for all the atoms forming the bulk system.

3.3 Geometry Optimizers

Among the panorama of algorithms used for electronic ground state calculations, the conjugate gradient scheme[9,10] and the Residual Minimization Scheme – Direct Inversion in the Iterative Subspace[11] (RMM-DIIS) are those employed within this work: for a given geometry, the electronic ground state is obtained from the self consistent field procedure and the resulting atom forces (defined within finite temperature approach as derivatives of generalized free energy) are used by the geometry optimizers to minimize energy with respect to atom co-ordinates; this is carried out cyclically until a convergence criterion is reached, usually set by default to $<10^{-4}$ eV energy difference between cycles.

The **conjugated gradient** algorithm is advised for systems with difficult relaxations: the first step of the routine is characterised by the modification of ions and cell shape towards the direction of the calculated forces and stress tensor (steepest descent direction), followed by a trial step and a correction step; the routine starts back again and carries on until energy convergence. The search direction found in the first step is conjugated to the gradient of all the following steps, which explains the name of this algorithm.

The use the **RMM-DIIS** (quasi-Newton) algorithm is more beneficial when the calculation is very close to a local minimum because the convergence is reached successfully; on the contrary, RMM-DIIS fails if the minimum (*i.e.* transition state) is far. The equilibrium positions are found following the search direction obtained via forces and stress tensor calculation in which the total energy is not considered. The forces are required to be very accurate to allow the algorithm to build up an approximation of the Hessian matrix by implicitly calculating the Hessian matrix inverse on the basis of previous iterations.
A variant of the RMM-DIIS algorithm ("special" RMM-DIIS) does not consider the energy but only calculates the forces that could represent a more convenient setting.

3.4 Vibrational Frequency Calculation

The adsorption of a photon by a molecule can occur if the latter has at least one of its normal modes vibrating at the same frequency as the former. The excitation of a molecule from its vibrational ground state to a given frequency also allows the adsorption of a photon vibrating at that frequency.

The equation for the vibrational frequency $\bar{\upsilon}$ (m^{-1}) of a simple harmonic oscillator can be written as shown below (3.13):

$$\bar{\upsilon} = \frac{1}{2\pi c}\sqrt{\frac{k}{\mu}} \qquad 3.13$$

where k ($kg \cdot s^{-2}$) is the force constant, μ (kg) is the reduced mass and c ($m \cdot s^{-1}$) is the speed of light.

The force constant, k, is provided by the larger part of the calculation which is the diagonalisation of the Hessian matrix (3.14):

$$H_{i,j} = \frac{\delta^2 E}{\delta x_i \delta x_j} \qquad 3.14$$

The matrix is constructed for all atoms in all three Cartesian coordinates by generating each of its elements, $H_{i,j}$, through a small finite increment of each atomic coordinate, x_i, followed by a calculation of the gradients, a coordinate finite decrement and finally a further gradients calculation, while the second derivative, $\delta^2 E$, is given by the difference of the step-size partial derivatives as shown in 3.15.

$$H_{i,j} = \frac{\left(\frac{\delta E}{\delta x_i}\right)_{+0.5\Delta x_j} - \left(\frac{\delta E}{\delta x_i}\right)_{-0.5\Delta x_j}}{\Delta\, x_j} \qquad 3.15$$

A re-definition (3.16) of the Hessian matrix allows the reduction of the gradient calculation random errors by a factor of $\sqrt{2}$; so, given that the matrix is symmetric:

$$H_{i,j} = H_{j,i} = \frac{1}{2}\left(\frac{\left(\frac{\delta E}{\delta x_i}\right)_{+0.5\Delta x_j} - \left(\frac{\delta E}{\delta x_i}\right)_{-0.5\Delta x_j}}{\Delta\, x_j} + \frac{\left(\frac{\delta E}{\delta x_i}\right)_{+0.5\Delta x_i} - \left(\frac{\delta E}{\delta x_j}\right)_{-0.5\Delta x_i}}{\Delta\, x_j} \right) \qquad 3.16$$

Prior to diagonalisation, the matrix (3.15) is mass-weighted ($H^m_{i,j} = \frac{H_{i,j}}{\sqrt{M_i M_j}}$). The eigenvalues, ε, provided by the matrix diagonalisation, provide the solutions to expression 3.13 ($\varepsilon = \sqrt{\frac{k}{\mu}}$):

$$\bar{\upsilon}_i = \frac{1}{2\pi c}\sqrt{\varepsilon_i} \qquad 3.17$$

The code employed in this study, VASP[13,14], calculates the Hessian matrix and the system vibrational frequencies (option IBRION = 5 in INCAR file). Since selective dynamics is supported (in POSCAR file), when the options is switched on, the Hessian matrix is calculated only for the tagged atoms.

3.5 Density of States

The dual nature of electrons allows us to consider these charged particles also as entities exhibiting wave-like properties, therefore an electron can be assigned a wave number, *k*, and can be represented by a vector in *k*-space.
In a classic system, there are no restrictions in the number of electrons occupying the same energy level. However, in a system where quantum mechanics rules apply (atomic scale), restrictions do exist because the electronic wavefunctions obey the Schrödinger equation and its boundary conditions; furthermore, the existence of energy degeneracy at atomic level allows multiple electron wavefunction solutions to exist, although only certain solutions represent band states that are occupied.

The density of states *D* is defined as number of states, *N(E)*, between $E = 0$ and *E* per crystal unit volume, *V*, as shown in 3.18:

$$D = \frac{1}{V}\frac{N(E, E+\Delta E) - N(E)}{\Delta E} = \frac{1}{V}\frac{dN}{dE} \qquad 3.18$$

The atomic scale restrictions, set by the quantum numbers n_x, n_y and n_z, only allow discrete values (states) in *k*-space leading to acceptable electron wavefunction solutions.
The number of allowed states in *k*-space, is given by the density of states in terms of *k*, *i.e.* $\rho(k)\,dk = 2 \times \frac{v\,dk}{V} = \frac{k^2 dk L^3}{\pi^2}$, which also accounts for the electron spin states (up or down): the expression is obtained by dividing the volume between the spheres of radius *k* and *k* + *dk*, *i.e.* $v\,dk = 4\pi k^2 dk$, and the total volume $V = \left(\frac{2\pi}{L}\right)^3$, all multiplied by a factor of 2.
In order to express *D* in terms of energy, the relationship between kinetic electronic energy of an electron ($E = \frac{p^2}{2m}$) and wave number $k = \frac{p}{\hbar}$ has to be considered,

which rearranged leads to $k = \sqrt{\frac{2mE}{\hbar^2}}$. The density of states in terms of energy *D(E)* per unit volume and unit energy, where N_S is the total number of states, is then given by in expression 3.19:

$$D(E) = \frac{1}{V} \cdot \frac{dN_S}{dE} = \frac{k^2}{\pi^2} \cdot \frac{dk}{dE} = \frac{1}{2\pi^2} \cdot \left(\frac{2m}{\hbar^2}\right)^{3/2} \cdot E^{1/2} \qquad 3.19$$

It is worth noticing that *D(E)* is proportional to $E^{1/2}$ and that it is independent of both the boundary conditions and the system dimension (it can also be applied to the bulk material). Similarly, in the "nearly free" electron model it is assumed that the interaction with the core-ions is fairly weak because it is shielded by the core-electrons, which brings to the situation where the conduction electrons form an effective "sea of electrons" subject to a weak perturbing potential. For strongly interacting electrons though, *D(E)* is calculated numerically with 3.18.

As the Pauli principle explains, a pair of opposite spin electrons can be assigned to each energy level, which corresponds to a *k* value. Once all electrons are assigned to all available levels, the *Fermi energy* is the energy of the highest occupied state. The *Fermi energy* can also identify where the band gap is, given that the number of electrons assigned is even and that therefore all the occupied levels are fully occupied.

3.6 Monte Carlo Implementation

Zebedde (ZEolite By Evolutionary De novo DEsign)[12] is a powerful tool created for different computational challenges: the program employs Metropolis[1] Monte Carlo (MC) methods to reach local and global minima of energy. The sequence of actions taken by *Zebedde* during the sampling of thermally accessible states by an alkane (*guest*) when the molecule is inside a zeolite (*host*), or pore, can be briefly summarized as follows: (1) once the zeolite unit cell is defined, the alkane is positioned at the framework centre of mass; because the latter could be located within the van der Waals radius of the pore wall atoms, in principle this first action of the program could cause a large system energy rise due to physical clashes between of alkane and pore atoms (radii overlapping); (2) random changes to the alkane configuration are then carried out by the program that aims to reduce the clashes, employing a Force Field (FF) energy as a control (ΔE in section 3.1). The changes are adjustments coded in the program script as *twist* (dihedral rotation around randomly selected C–C bonds), *shake* (displacement along a random vector) and *rock* (randomly rotated with respect to the pore); (3) each adjustment causes a change in FF energy. A new configuration is generated on the basis of two requirements (section 3.1): if it involves an energy decreases ($\Delta E < 0$), or instead, if it generates an energy increase ($\Delta E > 0$) and its probability $e^{-\Delta E / k_B T}$ is greater than a generated random number between 0 and 1 (see acceptance condition 3.1); (4) in case of rejection, the program carries out further random adjustments until the described conditions are satisfied; (5) in case of acceptance, the new configuration is selected as a starting point for new random adjustments in an attempt to find a more stable geometry; when this is no longer possible, the search is stopped and the last accepted geometry represents a minimum, which is equivalent to say that the alkane has landed on a void inside the *host*.

The outcome of this initial MC process is not just energetic (see adsorption energy expressions 4.1 and 4.2, section 4.4): the calculations also provide geometric information relative to which set of alkane conformations are allowed inside the pore framework, together with position and orientation of the adsorbate within the pore

channels, and they allow to map the most likely *host* regions where the *guest* is likely to eventually land.

The MC calculations are carried out on docked alkane/zeolite systems as a measure to avoid the situation where averaged energies be biased by large values due to the initial clashes following the first calculation step.

3.7 DFT Implementation

The use of the VASP[13,14] (Vienna *ab initio* Simulation Package) code has been fundamental within this study for the investigation of reactions on metal oxide surfaces.

The code employs the DFT method to describe periodic systems. The Kohn-Sham (K-S) equations are resolved through a combination of iterative diagonalisation matrix and Broyden[15] mixing scheme, in a self-consistent fashion: this approach is more efficient when transition metals, with their complex band structure around the Fermi level, are present in the system.

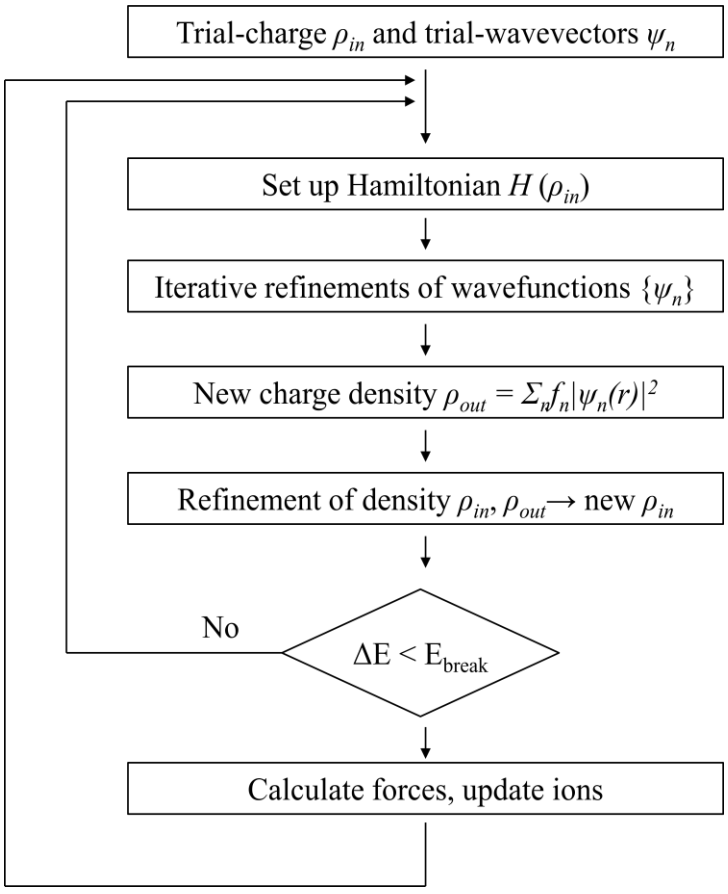

Figure 3.1. Self-consistency scheme

In particular, for what the charge density is concerned, a combination of Pulay[11] and Broyden mixing schemes has shown[13] an improved efficiency in reaching convergence via a self-consistent density functional calculation (figure 3.1). The

schemes refine the charge density by including a small amount of ρ_{in} (current density) into the following iterative step for the calculation of ρ_{out} (new density), so that the approximation that builds up improves more quickly and therefore converges earlier.

The system considered in the Local Density Approximation (LDA) is a uniform electron gas where the density is locally constant. An important limitation of LDA is in its inability to account for the rapid electron density modifications the system is subjected when scaling up from atoms to molecules. An improvement to LDA is the Generalised Gradient Approximation (GGA), which introduces gradients to the electronic density within the approximation in order to overcome those density changes; within GGA, the Perdew, Burke and Ernzerhof's (PBE)[16] functional is employed for the DFT implementation in this study because of its accuracy in describing the uniform electron gas, its ability to properly respond to the molecules' behaviour and for its smooth potential.

Localized functions, like for example Gaussians basis sets, are ion-position dependent, while plane-wave (PW) basis sets treat all areas of space equally and are independent of the crystal type considered; though, the main reason PW basis sets were employed in this periodic DFT study is to do with the fact that they are able to follow the periodicity of the simulation cell: in fact, only plane waves that are periodic with the cell length can be used. These are then combined via a Fourier transform to represent the ground state electron density.

To obtain exact calculations, plane-wave basis set dimensions should be infinite: practically, this can be resolved by truncating the infinite basis set to a finite number of plane waves, defined by the kinetic cut-off energy. In this study, in order to decrease the number of plane waves used, Fast Fourier Transformations (FFT) procedure (the most time consuming task in VASP) is employed, making the determination of the Hamiltonian an easier task since FFT are able to switch from direct to reciprocal space (and *vice versa*), which also provides with a partial diagonalisation that speeds up the K-S (DFT) equations solving.

Another advantage of plane-wave basis sets, if compared to the localised ones, is that the accuracy can also be improved by increasing the cut-off energy. An important disadvantage though is that the treatment of atom core areas is not efficient because this would require a rather large number of planes. For this reason, pseudopotentials are employed to overcome the problem and approximate core electron wave functions: these are pre-calculated within atomic environment and then kept frozen during the *ab initio* calculation. There are mainly two types of pseudopotentials for periodic systems, namely ultrasoft (US-PP)[17,18] and projector augmented wave (PAW-PP):[19,20] the latter has been employed in this study for its ability to exactly reproduce the valence wave function, including the core region nodes, and for being parametrised with smaller core radial cutoffs.

The integration over the Brillouin zone is fundamental to evaluate several important properties within periodic (surface) calculations. In order to compute these integrals, one has to consider the concept of a mesh divided[21] by special points (*k*-points), the (finite) number of which affects directly the accuracy of the computation.
The idea of *k*-points was introduced in an attempt to resolve the problem of calculating periodic functions over an infinite number of points in reciprocal space, as infinite is the possible phase patterns across an infinite crystal. Bloch's theorem in fact states that integrating in real space over a periodic surface is equivalent to carrying out the same operation in reciprocal space over the finite Brillouin zone. Therefore, exploiting the property that electron wavefunctions do not show significant change over small distances in *k*-space, integrations can be computed as discrete summations over finite (but dense) mesh of *k*-points.
In the event of partial occupancies, the linear tetrahedron (bulk systems) and smearing methods, namely finite temperature approaches (metallic surfaces), are the choices to improve convergence in respect to *k*-points sampling. Also methods like Methfessel and Paxton or Gaussian and Fermi smearing can be used for more accurate calculations (*i.e.* density of states).

References

[1] N. Metropolis, A. W. Rosenbluth, M. N. Rosenbluth, A. H. Teller, E. Teller *J. Chem. Phys.*, **21**, 1087 (1953).
[2] P. Hohenberg, W. Kohn *Phys. Rev.*, **136**, B864-B871 (1964).
[3] W. Kohn, L.J. Sham *Phys. Rev.*, **140**, A1133-A1138 (1965).
[4] R. G. Parr, W. Yang *Density-Function Theory of Atoms and Molecules*. 1989, New York: Oxford University Press.
[5] A. D. Becke *J. Chem. Phys.*, **98**, 1372 (1992).
[6] J. Harris *Phys. Rev. A*, **29**, 1648 (1984).
[7] S. L. Duradev, G. A. Botton, S. Y. Savrasov, C. J. Humphreys, A. P. Sutton *Phys. Rev. B*, **57**, 1505 (1998).
[8] H. Tasaki *J. Phys.: Condens. Matter*, **10**, 4353-4378 (1998).
[9] M. P. Peter, M. C. Payne, D. C. Allan *Phys. Rev. B*, **40**, 12255 (1989).
[10] D. M. Bylander, L. Kleinman, S. Lee *Phys. Rev. B*, **42**, 1394 (1990).
[11] P. Pulay *Chem. Phys. Lett.*, **73**, 393 (1980).
[12] D. W. Lewis, D. J. Willock, C. R. A. Catlow, J. M. Thomas, and G. J. Hutchings *Nature* **382**, 604 (1996).
[13] G. Kresse, J. Furthmüller *J. Comp. Mat. Sci.*, **6**, 15 (1996).
[14] G. Kresse, J. Furthmüller *J. Phys. Rev. B*, **54**, 169 (1996).
[15] D. D. Johnson *Phys. Rev. B*, **38**, 12807 (1988).
[16] J. P. Perdew, K. Burke, M. Ernzerhof *Phys. Rev. Lett.*, **77**, 3865-3868 (1996).
[17] D. Vanderbilt *Phys. Rev. B*, **41**, 7892 (1990).
[18] G. Kresse, J. Hafner *J. Phys.: Condens. Matter*, **6**, 8245 (1994).
[19] P. E. Blöchl *Phys. Rev. B*, **50**, 17953 (1994).
[20] G. Kresse, J. Joubert *Phys. Rev. B*, **59**, 1758 (1999).
[21] H. J. Monkhorst, J. D. Pack *Phys. Rev. B*, **13**, 5188 (1976).

4. Methodology

4.1 Host-Guest Monitoring Study and k_{prim}/k_{sec} Estimation

Iglesia *et al.*[1] showed that the selectivity of the oxidation of *n*-hexanes occurring inside zeolites could be influenced by the choice of the zeolitic channel structure. This triggered the focus of this part of the study towards the idea that the channel structure alone could be accountable for the observed differences in selectivity between the reaction occurring in gas phase and inside the zeolites. A study of distances between selected host-guest (zeolite-alkane) atoms was carried out to computationally reproduce those experimental results. The distances C_{alkane}–$O_{zeolite}$ and C_{alkane}–$Si_{zeolite}$ were monitored during a MC calculation and the exercise was extended to all the three alkanes (*hexane*, *octane* and *decane*) inside the zeolites studied in this project (*MFI*, *MFS* and *MOR*).

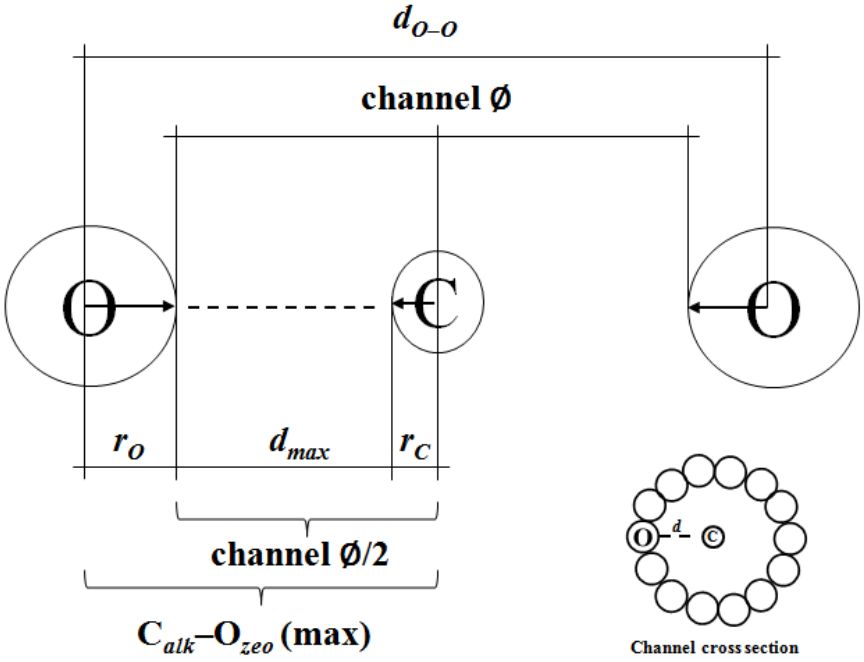

Figure 4.1. Drawing of the interatomic distances between guest C atoms and host O atoms within a zeolite channel. The *Zebedde*[3] code was modified to record visits of the C within the d_{max} range only. *Right corner*: a zeolite channel cross section with one guest C atom in the middle.

Figure 4.1 shows a drawing for the C_{alkane}–$O_{zeolite}$ distance study, but the same concepts can be extended to the C_{alkane}–$Si_{zeolite}$.

The *Zebedde*[3] code (chapter 3) was employed to carry out the monitoring study that was run along the MC calculations. The code required to be modified in order to follow the two distances and was instructed to monitor all contact events for the relevant atoms within a cut-off distance. This distance was the result of the sum of O ionic radius,[2] C atomic radius[2] and the maximum value of the distance *d*, namely d_{max}, corresponding to the alkane C atom positioned in the middle of the zeolite channel. With this modification, the calculation was able to source the number of visits that the alkane C atom made within the range d_{max} and to associate each visit to the corresponding C_{alkane}–$O_{zeolite}$ (or C_{alkane}–$Si_{zeolite}$) value. The aim of the monitoring study was to demonstrate that the number of visits made by the terminal alkane C atom is greater than that of the internal C atoms along the chain, which indicates that during a MC sampling run the terminal alkane C atoms are more likely to be closer to the zeolitic wall than those further inside the chain. These findings were then used to estimate the terminal reactivity in terms of *pore effect*. In fact, the existence of a *pore effect* would be enough to demonstrate that the zeolite frameworks have an influence on the reactivity and that this influence was driven by the zeolitic channel shape (*shape selectivity*).

The *pore effect* of the zeolite over the regioselectivity of the alkane oxidation was described by comparing the constants of the reaction occurring at terminal positions on the alkane chain, *i.e.* k_{prim}, and at the second positions, *i.e.* k_{sec}. In order to estimate the terminal selectivity of the reaction though, the k_{prim}/k_{sec} ratio was calculated for each host-guest combination. This was carried out using the data sourced by the monitoring study. The rationale behind this is based on the fact that in chemical terms each visit made by an alkane C atom within the d_{max} range from the zeolite O (or Si) atom can be seen as a potential reactive event, which means that the C atom that makes more of these visits is more likely to react. Therefore, the k_{prim}/k_{sec} ratio is a way to qualitatively estimate the reactivity of the terminal C atom against that of the C atoms of the methylene ($–CH_2–$) group in second position. Numerically, the k_{prim}/k_{sec} ratio is simply equal to the ratio between the number of

visits for primary and secondary C atoms to the zeolitic O (or Si) atoms as a function of the distance. The k_{prim}/k_{sec} ratio expected values are greater than the unity, in case of terminal selectivity, or between 0 (zero) and the unity, which would mean that the methylene C atoms are more reactive towards the oxidation. As already anticipated above, *Zebedde* was able to associate each C atom visit to the corresponding C_{alkane}–$O_{zeolite}$ (or C_{alkane}–$Si_{zeolite}$) value, which means that each k_{prim}/k_{sec} ratio is also associated to the same value. This in turn allows identifying the most favourable C_{alkane}–$O_{zeolite}$ (or C_{alkane}–$Si_{zeolite}$) distance for the terminal position to be oxidized.

4.2 Adsorption Energy

The adsorption of a *guest* molecule on a *host* surface of a real system is characterized by a complex set of interactions adsorbate/adsorbent (alkane/zeolite). The first of two contributions to these interactions is quantified by the *van der Waals* energy (E_{vdW}), relative to the interaction between the charge clouds on each *guest* (adsorbate) atom and that on each *host* (adsorbent) atom. In this study, the interaction is considered only within a cut off distance atom-atom and the energy E_{vdW} is obviously function of *guest*/*host* inter-atomic distances, often modelled by the Lennard-Jones (LJ) 12-6 potential. The LJ potential is positive for short distances due to the repulsion of the overlapping electronic orbitals, while is always negative at very large distances atom-atom although it approaches the zero value. This part of the energy is the most indicative of whether the MC sampling of alkane configurations has generated an ensemble and has reached a stable level. The standard deviation of the energy is able to give a feedback on whether the calculation is required to be run for larger number of MC steps or not. The second contribution to the host/guest interactions is quantified by an *intramolecular* potential (E_{intra_alkane}) for the alkane (adsorbate), as a function of its internal coordinates, which contributes to the adsorption energy through geometry distortion caused by the structure rearrangement following the binding to the surface. E_{intra_alkane} is always a positive energy and it provides useful information in the comparison between configurations of the same molecule, in which case an energy difference (ΔE) would be indicative of the relative stability between conformers.

The program *Zebedde*[3] is designed to source total energy (E_{tot}), which is the sum of the E_{intra_alkane} and E_{vdW} contributions, as shown in 4.1.

$$E_{tot} = E_{intra\_alkane} + E_{vdW} \qquad 4.1$$

The event of an alkane entering and diffusing inside a zeolite (pore), followed by its adsorption onto the internal walls of the framework, can be considered like a chemical reaction between reactants that are converted into products, as represented by the statement $<<alkane_{(g)} + pore \rightarrow alkane_{(ads)}\cdots pore>>$. Just like it would happen

for the expression of the energy of a chemical reaction, *i.e.* $\sum_{PROD} En - \sum_{REAC} En$, the adsorption energy (E_{ads}) expression of the above process can be written out in equation 4.2:

$$E_{ads} = E_{tot} - E_{intra\_pore} - E_{alkane(g)} \qquad 4.2$$

In the calculations, the zeolite is considered as the environment. For this reason $E_{\text{intra\_pore}}$ is set to zero, which simplifies 4.2 to 4.3:

$$E_{ads} = E_{tot} - E_{alkane(g)} \qquad 4.3$$

In order to calculate the adsorption energy, it is necessary to have a reference state to the energy of the alkane in gas phase. This also allows making comparisons with different host/guest systems. The process followed to compute $E_{alkane(g)}$ from 4.3 involves running a MC simulation for the alkane in gas phase using a periodic repeat of the same dimensions of the supercell used in the adsorption calculations. This gives the reference state for the molecule adsorbing into the zeolite framework. The corresponding $E_{tot(g)}$ only includes an $E_{intra\_alkane(g)}$ contribution as the interaction alkane/zeolite is neglected. Therefore, obtaining E_{ads} is reduced to arithmetically carrying out a simple $E_{tot} - E_{tot(g)}$ subtraction, as shown in 4.4:

$$E_{ads} = E_{tot} - E_{tot(g)} = E_{inter\_alkane} + E_{vdW} - E_{inter\_alkane(g)} \qquad 4.4$$

To be noticed is that the two energies E_{inter_alkane} and $E_{inter\_alkane(g)}$ carry different information although they refer to the same molecule. The $E_{intra\_alkane(g)}$ contribution explores all the possible configurations of the alkane in the gas phase because it has more freedom than the alkane inside the zeolite. Because of this, 4.4 takes into account the part of the adsorption free energy that has to do with the change in the available alkane configurations when passing from gas phase into the zeolite.

4.3 Converging Calculation Parameters

4.3.1 *k*-points

For the periodic DFT calculations presented in chapter 6, choosing the correct number of *k*-points is fundamental to carry out an accurate periodic calculation. The other important aspect directing the choice of how many *k*-points to consider is whether the system is metallic, semi-conductor or insulator: a metallic system requires an order of magnitude more *k*-points than the other types of systems.

The *k*-point mesh chosen is picked at the bulk energy convergence with respect to the fineness of the mesh itself.

Surface calculations are run inside a cell having three lattice vectors pointing towards the three directions in space. The longest lattice vector is corresponding to the vacuum, where the band dispersion is zero: for this reason, only one *k*-point sampled along this direction is enough. The other two directions have the same number of *k*-points found for the bulk, since the convergence speed between the two systems is very similar.

Table 4.1. MoO_3 bulk energy convergence is tested against the *k*-point grid variation. The energy difference between two consecutive grids is shown in the ΔE column.

***k*-points grid**	**MoO_3 bulk energy (eV)**	**ΔE (eV)**
3×3×1	-101.64008	-
3×3×3	-101.643535	-0.003455
5×5×5	-101.74473	-0.101195
7×7×7	-101.749512	-0.004782
9×9×9	-101.75013	-0.000615

Table 4.1 shows that the convergence of MoO_3 bulk was reached for the 3×3×1 *k*-point grid to a precision of 10^{-3} eV. The MoO_3 bulk lattice parameters are a = 13.825 Å, b = 3.694 Å and c = 3.954 Å.

4.3.2 Mesh Cut-off

The maximum value of ENMAX is set when PREC = High. ENMAX for MoO_3 is 400 eV (oxygen) so when PREC = High, VASP[4,5] sets the energy cut-off value to 520 eV, which is equivalent to the maximum value of ENMAX found in the PP file increased of 30%. Figure 4.2 shows a plot where variation of the bulk energy is tested against the energy cut-off ENMAX.

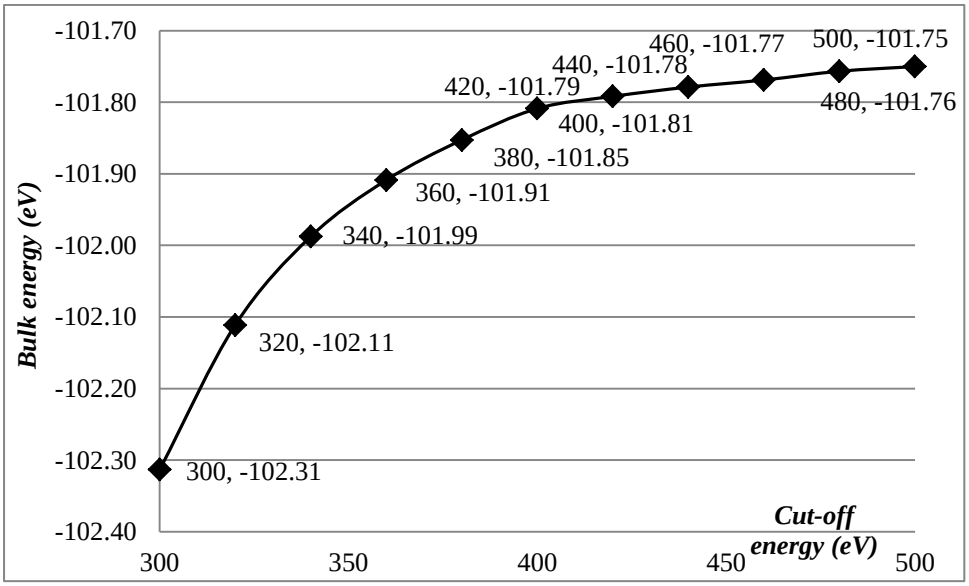

Figure 4.2. Bulk energy as a function of the cut-off energy: the study is carried out to find the suitable value to use in the calculations.

The bulk energy is fully converged within 0.007 eV when the cut-off energy is equal to 500 eV. When PREC = Normal or Accurate, the cut-off energy is set by default to 400 eV: this value of cut-off energy gives an energy difference of 0.04 eV which is satisfactory for the large number of calculations run in this project, while a higher value of energy cut-off is only required for accurate evaluations of quantities related to the stress tensor.

4.4 Lattice Parameter Optimizations

The theoretical analogy between DFT and many-body models, in terms of forces acting on atoms, could lead to think that the Pulay problem ($\widetilde{F}_i$) does not occur.

The Hellmann-Feynman forces ($F_i = -\frac{d}{dR_i}\langle \Psi \mid H \mid \Psi \rangle = -\left\langle \Psi \mid \frac{\partial H}{\partial R_i} \mid \Psi \right\rangle - \widetilde{F}_i$) are the derivatives of the total energy with respect to the atomic positions (R_i): in the many-body theory, the implicit derivatives $\widetilde{F}_i$ vanish from the Hamiltonian because they are the derivative of a constant ($\widetilde{F}_i = E\frac{d}{dR_i}\langle \Psi \mid \Psi \rangle$).

Similarly, the variational character of DFT allows simplifying the calculation of the forces acting on atoms: in equation 4.5, the explicit derivative of the electronic part and the ion term (E_{II}) can be easily calculated, while the last term of the equation is eliminated when the ground state is a minimum.

$$F_i = -\nabla_{R_i} E = -\int n(r)\nabla_{R_i} V(r)dr - \nabla_{R_i} E_{II}(R) - \int \left[\frac{\partial F}{\partial n(r)} + V(r)\right]\nabla_{R_i} n(r)dr \qquad 4.5$$

In VASP though, performing calculations with the energy varying with the lattice volume causes problems leading to the diagonal components of the stress tensor to be incorrect. This issue (Pulay stress) is caused by the fact that the plane wave basis set employed is not complete with respect to changes of volume. Furthermore, all the volume/cell shape relaxation algorithms implemented in VASP employ constant basis sets, and this leads to an underestimation of the equilibrium volume as a result of the energy changes.

There are approaches though that can minimise the problem, if not completely eliminate it: many calculations, where plane wave basis sets are employed, have shown a nearly absent Pulay stress if constant volume relaxations are carried out; this is due to the nearly uniform variation of the diagonal stress tensor elements that always change of a constant amount. Alternatively, calculations where the volume

changes as opposed to a constant energy cut-off have also shown a satisfactory Pulay problem reduction.

The latter approach is employed within this study because it has shown reliability for bulk modulus and lattice constant calculations (variation step of the lattice parameter is 1% of the initial value).

4.5 Transition State Search

Within the modelling of a chemical reaction, the knowledge of a transition state (TS) geometry and energy barrier represents one of the most important targets in computational chemistry because it discloses fundamental information about the species (or even the different parts within one species) directly involved in the process that turns reactants into products. The description of a TS is one of the most difficult tasks in theoretical field, which is proven by the large number of methods developed over the years with this objective. The approach adopted within this study to identify the TS is by employing in sequence the Nudged Elastic Band[6,7,8] (NEB) method and the Dimer method.[9]

The Nudged Elastic Band method

The study is carried out with the end structures already being known. The method builds up a reaction path by guessing an established number of intermediate geometries connecting start and end molecules; these geometries, or images, are linked to each other by "springs", in order to prevent them from crashing at the end points. In this study the spring constant is set to the default value (SPRING = -5), and this allows a uniform distribution of the images along the energy path. The downsides of this method are represented by the images sliding down towards the minima and also the tendency of the path to tunnel through the TS energy barrier when approaching the TS. These issues are resolved by projecting out the perpendicular component of the spring and the parallel component of the true force from the total force that acts on each image. If the end structures are $\vec{P}_0$ and $\vec{P}_M$, the $M-1$ images are $\vec{P}_1$, $\vec{P}_2$, etc. to $\vec{P}_{M-1}$, with $\vec{P}$ being a generic point in the system phase space (3×N lists of coordinates within a system formed by N atoms); the force acting on each image i (calculated from the DFT equations) is expressed by $F_i = \vec{F}^S_{i||} + \vec{F}^l_{i\perp}$ where $F^S_{i||} = (k_{i+1}|\vec{P}_{i+1} - \vec{P}_i| - k_i|\vec{P}_i - \vec{P}_{i-1}|)\hat{\eta}_i$ is the component of the force that is parallel to $\hat{\eta}_i$ (normalized local tangent at imagine i), $\vec{F}^l_{i\perp}$ is the perpendicular component and k_i is the spring constant between the images i and $i-l$.

In proximity of a saddle point, the number of images is increased purposely to have a better estimation of $\hat{\eta}_i$.

VASP is run with all the input files located in the same directory, which must also contain as many subdirectories as the images employed are: each subdirectory must store a POSCAR geometry file corresponding to the relevant image. The number of images is set prior to the calculation by specifying an integer number in the input file; images can either be sourced by an initial linear interpolation or, where the complexity of the reaction requires a cleverer way to describe how the geometry is affected along the pathway, by the GRUP method which is part of the utility program *Intervasp*,[10] created and developed by Dr. Willock's team. Here is a brief explanation of how *Intervasp* and the GRUP method work: within the start geometry file, a central atom is identified and each atom of the group the central atom belongs to is labelled as GRUP; the calculation carries out a linear interpolation of the central atom between its initial and final coordinates, stored in the end geometry file. Initially, each one of the GRUP atoms are also interpolated on the basis of their initial and final distance from the central atom, but then adjustments to their positions are made in order to have a smooth variation of this distance along the interpolation. These adjustments are required in order to avoid situations where bond lengths within the molecule, in our case propane (C_3H_8), are shortened as a result of the interpolation. Within *Intervasp*, the option *late centre* is also available to interpolate those reactions where the molecule has to reach an optimal position before an atom transfer, from the molecule to the surroundings, can take place. When the *late centre* option is selected, the program generates a trajectory composed by two parts: the first part is characterised by the molecule moving as a rigid body along the direction of the vector between initial and final positions of the transferring atom. The beginning of the second part of the trajectory is predetermined on the basis of the transferring atom final bond length, stored in the end geometry file; the SWITCH directory value *multiplier* specifies the distance range within which the atom starts moving towards its final position (*multiplier* default value is 1.5 times the transferring atom final bond length). When the transferring atom is within the switch over distance, the program stores the current molecule centre of mass coordinates, works out the centre of mass trajectory vector to take the molecule from the switch

over position to its final position and smoothly moves the rest of the molecule towards that final position. A further level of control for this process can be introduced by modifying a second SWITCH value, namely *magnification factor*, which specifies the density of steps the algorithm should take after the switch over occurs. Finally, it is clear that the number of images when the GRUP method is employed is a combination between interpolation integer, *multiplier* and *magnification factor*.

The Dimer method

The NEB method is supported by the dimer method9 in its search for the transition state (TS). The ability of the dimer method to employ first derivatives to identify saddle points is fundamental for plane wave based DFT calculations in order to avoid evaluating costly second derivatives. The dimer method can find a TS without any knowledge of its final state, but in this study its use is aimed at refining the already guessed TS by the NEB method: two images, the "dimer", at a distance ΔR from each other, are moved uphill on the potential energy surface (PES) by the algorithm. During this process, the lowest curvature mode of the dimer position is the target sought by rotating the images.

The movement of the dimer over the PES is tracked by computing force (F_R) and energy (E_0) acting on the dimer midpoint. It is important to highlight that the key aspect of this approach is that it allows considerable reduction (*via* parallelization) of force and energy evaluations required to find saddle points, because F_R and E_0 are derived from energies (E_1, E_2) and forces (F_1, F_2) acting on the two images, rather than being evaluated at the midpoint itself: F_R is the average force of F_1 and F_2, while E_0 is derived in 4.6:

$$E_0 = \frac{E}{2} + \frac{\Delta R}{4} \cdot (F_1 - F_2) \cdot \hat{N} \qquad 4.6$$

where E (energy of the dimer) is the sum of the energies acting on the images.

The algorithm displaces the dimer and at the same time rotates it and minimizes E. The minimization of E is linearly related to the potential curvature, C, as shown in 4.7.

$$C = \frac{E - 2 \cdot E_0}{(\Delta R)^2} \qquad 4.7$$

This means the rotation aims to identify the lowest curvature mode at the dimer midpoint which corresponds to the saddle point.

4.6 Cluster models

Four clusters of different size were cut from MoO_3(010) perfect surface, each one including a growing number of molybdenum atoms, *i.e.* one, three, six and fifteen, with all their relative neighbouring O atoms and H atoms employed to saturate the valence at the edges of the cluster where surface atoms were neglected (figure 6.4), following the saturation scheme adopted by Witko and co-workers[11,12] in their MoO_3 cluster models. The optimized $Mo_1O_6H_6$ structure recalls very closely the configuration of molybdenum in a MoO_6 basic unit of the orthorombic MoO_3 layered structure discussed in chapter 2, a distorted octahedron with a central molybdenum atom and six neighbouring O atoms. Since molybdenum symmetric features, when bonded to oxygen atoms, are clearly transferred from the surface to the clusters (chapter 6), discussions of cluster structures within this work will adopt the same oxygen species labelling used for the bulk and surface structures in chapter 2: for clusters too, each molybdenum atom is bonded to two *asymmetric* (O_A) oxygen atoms with a single bond, two *symmetric* (O_S) oxygen atoms with a single bond and a *terminal* (O_T) oxygen atom with a double bond.

The same cluster construction protocol is followed for $Mo_3O_{14}H_{10}$, $Mo_6O_{25}H_{14}$ and $Mo_{15}O_{56}H_{22}$ clusters and is briefly explained: the H atoms for the cluster termination are added to O atoms at the cluster edges and placed at the standard distance of 0.97 Å, on the same direction of the bond with the neglected surface Mo atom, and then optimized. O_T atoms have no H atom added as their valence is implied from the bond distance with their vicinal Mo atom: since Mo–O_T corresponds to a double bond, the O atom is already fully saturated. O_A atoms have either no H atom added if their distance Mo–O_A is equal to that of Mo–O_T, for the same reasons, or two H atoms added if otherwise, while O_S have one H atom added. For the way clusters are built, two of the lower side edges have the interlayer O atoms bonded to only one Mo atom: for this reason, each O atom has only one H atom added.

In total, the number of H atoms added to each clusters in order to satisfy their stoichiometry, is six for $Mo_1O_6H_6$, ten for $Mo_3O_{14}H_{10}$, fourteen for $Mo_6O_{25}H_{14}$ and twenty-two for $Mo_{15}O_{56}H_{22}$.

Each cluster structure was prepared for the calculations with the adsorbate: geometry optimizations of a perfect cluster, which is a cluster with no O atom removed from its surface (no defect), were carried out keeping the cluster atoms initially frozen and allowing only the H atoms to relax. This was followed by another geometric optimization where the H atoms were kept frozen into their optimized positions while the body of the cluster was allowed to relax: in this way, the central region results bonded to an optimized peripheral region that mimics a periodic structure and this set up was used in all the remaining calculations the relevant cluster was undergoing. At convergence of the second geometry optimization, an O_T atom was removed from the cluster to create a defect and a further geometry optimization was carried out. At convergence, the relevant cluster was considered ready to be employed in geometry optimizations with the substrate to model the adsorption process.

References

[1] B.-Z. Zhan, B. Modén, J. Dakka, J. G. Santiesteban, E. Iglesia *J. Cat.*, **245,** 316–325 (2007).
[2] R. D. Shannon *Acta Cryst. A*, **32**, 751 (1976).
[3] D. W. Lewis, D. J. Willock, C. R. A. Catlow, J. M. Thomas, and G. J. Hutchings *Nature* **382**, 604 (1996).
[4] G. Kresse, J. Furthmüller *J. Comp. Mat. Sci.*, **6**, 15 (1996).
[5] G. Kresse, J. Furthmüller *J. Phys. Rev. B*, **54**, 169 (1996).
[6] H. Jönsson, G. Mills, K. W. Jacobsen *Classical and Quantum Dynamics in Condensed Phase Simulations*, ed. B. J. Berne, G. Ciccotti, D. F. Coker (1995), Singapore: World Scientific.
[7] G. Mills, H. Jönsson *Phys. Rev. Lett.*, **72**, 1124 (1994).
[8] G. Mills, H. Jönsson, G. K. Schenter *Surf. Sci.*, **324**, 305 (1995).
[9] G. Henkelman, H. Jónsson *J. Chem. Phys.*, **111**, 7010 (1999).
[10] http://theory.chem.cf.ac.uk/~dave/inter_vasp.html.
[11] A. Michalak, K. Hermann, M. Witko *Surf. Sci.*, **366**, 323-336 (1996).
[12] K. Hermann, M. Witko, A. Michalak *Catal. Today*, **50**, 567-577 (1999).

5. Hexane, Octane and Decane Adsorption in Zeolites

5.1 Introduction

The oxidation of linear hydrocarbons is an important and still relatively unexplored chemical process to convert C_7–C_{12} alkanes to their corresponding alcohols. The oxidising agent chosen for this study is air, although both peroxy species and dioxygen (O_2) itself are valid oxidizing agents. Hydrogen peroxide is a very powerful oxidant and very selective. The negative aspects of using hydrogen peroxide industrially though are represented by the fact that it is a hazardous substance, a mutagen and an unstable and irritant liquid that requires special storage conditions undergoing strict safety regulations. The use of oxygen instead of air in chemical reactions has to be evaluated too. For example, when used in high pressure conditions, the compression savings have to offset the higher cost of the product relatively to air. When O_2 is employed with catalysts at low per-pass conversion, the reaction benefits from its use because the elimination of the inert nitrogen reduces the amount of unreacted feed that requires to be recycled, but this does pose a health and safety risk since increasingly explosive regions are encountered during the diluent removal.

Enzymes found in microorganisms like *Methane Monooxigenase* (chapter 2) and *Cytochrome P-450 Monooxygenase*[1] are examples of natural systems able to overcome limitations imposed when molecular oxygen is employed to oxidize hydrocarbons. Scientists study these models provided by nature to transfer those characteristics into laboratories in order to build and develop catalytic systems capable of mimicking layout and environment of the enzymatic active sites.

Development of successful catalysts is also based on the observation of important aspects of existing systems and on their maximization to further improvement. With this approach, Iglesia and co-workers[2] described how microporous materials, employed as support for oxidation of linear alkanes, can affect reaction rates and regioselectivity for the production of terminal alcohols, and outlined how the shape selectivity of the active sites has an important influence on which regioisomer is predominantly produced (chapter 2).

Molecular oxygen insertion at terminal C–H bonds in linear alkanes is less likely to occur in gas phase than at secondary positions: H atoms are more strongly bonded to terminal C atoms than to those in methylene groups (–CH_2–). The energy necessary to remove a terminal H atom from propane (H-*n*-C_3H_7) is greater than that required for a secondary H atom (H-*i*-C_3H_7) (423.3 *cf.* 409.1 kJ mol^{-1}),[3] in fact the resulting secondary carbocation is more stable than the primary as the partial charge is more delocalized by the inductive (electron donating) effect exerted by the alkyl groups in the former case. As a result of this, terminal alcohols are not the main products in gas phase alkane partial oxidations as terminal C–H bonds, in linear alkanes, are more difficult to oxidize.

What just described is only one of the aspects exerting an influence over the regioselectivity of the reaction studied here. The use of zeolites, materials with a characteristic system of internal micro-channels and pores, increases the number of elements able to have an effect on the final result of the reaction. In other words, as discussed in chapter 2, a higher terminal selectivity for the reaction is no longer purely a function of the substrate carbon atoms intrinsic reactivity in gas phase: local constraints at the zeolitic active sites play a role in selectively affecting the reaction chemical path, therefore it is possible here to talk about zeolite shape selectivity, the description of which is the aim of this part of the study. The first task was to reproduce computationally what Iglesia and co-workers described experimentally.[2] They analyzed Mn-exchanged *MFI*, *MFS* and *MOR* and probed the zeolites selectivity through the oxidation of a linear chain alkane like *hexane*. They found that, the substrate converts into the corresponding terminal alcohol with a selectivity of 24% (Mn-*MFI*), 14% (Mn-*MFS*) and 9.5% (Mn-*MOR*) compared with the unselective noncatalytic reaction (8.2%). These figures were obtained within the first 0.5 h of reaction and therefore at low conversion (*initial* terminal selectivity). This was necessary to minimize the presence of the intermediate ROOH, identified in the proposed reaction mechanism (figure 2.16), because after the initial stage of the reaction the increasing intermediate concentration would decrease the selectivity of all zeolites down to the level of the unselective noncatalytic process. The explanation for the patterns found by Iglesia and co-workers is on the channel dimension grounds. Foster *et al.*[4] defined a zeolites *cavity* as the diameter (D_i) of the largest

sphere that can fit the framework, with the sphere not necessarily being free to move, and the *aperture* of a zeolite as the diameter of the largest sphere that can freely move inside the zeolite framework (here labelled D_{max} not to be confused with d_{max} of figure 4.1). *MFI* with 6.30 Å (D_i) and 4.64 Å (D_{max}) is the zeolite with the most severe internal constraints compared to *MFS* (6.75 / 5.31 for D_i /D_{max}, Å) and *MOR* (6.4 / 6.39 for D_i /D_{max}, Å), and these characteristics were identified by Iglesia and co-workers as the elements driving the (initial) terminal selectivity of the reaction.

5.2 Computational details

Zebedde[5] is the C-code program employed in this study (chapter 4) to investigate the adsorption of alkanes on the internal zeolitic surface, and also to identify likely alkane adsorption configurations and relevant energies. This information is important to ascertain whether the *regio*-chemistry of the reaction under study is affected by the adsorption stage, which has already been experimentally demonstrated being influenced by what is defined as *shape selectivity* exerted by the zeolites.[2] Despite originally designed for *templating*[6] purposes, thanks to its flexibility the program allows its use for a wide range of computational challenges. Its modification allowed dealing with zeolites and reactions occurring inside their structures.

Once the zeolite structure is sourced by the modelling package[8] employed in this study, the correct force field is applied to the structure: PCFF[7] (values in Appendix 1), from the family of CFF91 force fields, is parameterized against experimental values covering a wide range of compounds, including zeolites. A Metropolis Monte Carlo (MC) calculation (chapter 3) run in this study with *Zebedde* can be divided into two stages, the first one of which is more of a docking style run. The program starts by positioning the substrate in a location in correspondence of the centre of mass of the zeolite unit cell. No centre of mass position is established *a priori*, therefore the docking run is purely aimed at eliminating energy biases due to initial clashed in those instances when the zeolite centre of mass results either very close to a channel wall, or even inside it. The moves of the guest (alkane) structure that the program visits (chapter 3) are coded as *twist*, which involves the rotation of the dihedral angle around randomly selected C–C bonds, *rock*, where the molecule rotates with respect to the zeolite and *shake*, which is the displacement of the molecule structure along a random vector. For the *twist* and *rock* actions, the step size taken is of 45° and 5°, respectively, while for *shake* the molecule is displaced of 0.1 Å.

As discussed in chapter 4, the program calculates the van der Waals (vdW) interaction energy between each atom of the guest molecule and each atom of the host framework (zeolite), and also the internal molecular mechanics energy of the guest. The cut-off distance for the vdW energy calculation was set to 6.5 Å and the

computations were run at the temperatures of 350K and 500K. These temperatures were chosen in order to investigate over a wider range around the experimental temperature of 403K. The purpose of this is to verify whether there is an underlying temperature effect that might influence the reaction and also to sample more configurations during the MC calculations.

At the end of the docking run, which is when the average energy stops decreasing, the guest molecule is in a more reasonable location (in a void and away from the host internal walls) to start a second MC run that is then able to sample statistics: averaged energies and standard deviation are calculated at each accepted MC step.

During the run, the program compares its own force field database with the potential types defined for the input file in the PCFF force field, looking up for bond and angle stretch, torsion and van der Waals potentials.

Zebedde is able to generate clips of the MC run that can be used to visually appreciate the alkane structure moves visited during the run, realize the interactions between guest and host, testing the implications of alkane chain length during the run and probing the more likely areas of the zeolite channels where alkanes are driven to. The clips created show frames written from the trajectory files generated by the guest structure accepted moves. The program can be modified so that only a chosen number of frames are actually shown, and this is to avoid having to handle large clip files. As part of this project, geometry analysis (monitoring study, section 4.1) was written into this part of the code to produce distributions of A–B atom distances, with A and B defined by the user in the input file.

5.3 Alkanes adsorbing in Silicalite-1 (*MFI*), *MFS* and Mordenite (*MOR*)

MC calculations were run with three alkanes of linear structure and different numbers of carbon atoms, *i.e. hexane* (6), *octane* (8) and *decane* (10), in order to test the adsorption energy against the chain length. The guests have been docked inside the structures of the three zeolites discussed earlier (*MFI*, *MFS* and *MOR*) prior to running MC calculations, as already anticipated.

The standard deviation of the host/guest MC interaction energy E_{vdW} (chapter 4) is a good indicator of whether the calculation has sampled the correct configurations of the system among the many possible. Table 5.1 collects data relative to the converged MC energies of three consecutive runs for each alkane/zeolite system.

Table 5.1. Alkane-zeolite interaction energy E_{vdW} (with standard deviation) for the studied systems at 350K: 10^6 steps were used for the MC calculations.

	Stable E_{vdW} *Energies* (kcal mol^{-1})		
	MFI	***MFS***	***MOR***
hexane[a)]	-14.23 ± 2.28	-10.93 ± 2.30	-9.30 ± 2.31
octane[b)]	-14.38 ± 2.66	-18.38 ± 2.77	-16.76 ± 2.64
decane[c)]	-22.80 ± 2.90	-20.23 ± 2.83	-19.28 ± 2.84

Energies are averages of three consecutive MC runs (kcal mol^{-1}): [a)] in *MFI*: -15.46, -12.38 and -14.86; in *MFS*: -14.01, -10.53 and -8.26; in *MOR*: -11.62, -4.26 and -12.02; [b)] in *MFI*: -19.55, -14.44 and -9.14; in *MFS*: -20.29, -17.26 and -17.59; in *MOR*: -19.92, -14.35 and -16.02; [c)] in *MFI*: -23.63, -17.94 and -26.84; in *MFS*: -16.87, -27.03 and -16.78; in *MOR*: -19.48, -21.18 and -17.18.

Figures 5.1 to 5.3 show snapshots of the equilibrated calculations where each alkane has reached a void in the middle of the relevant channel: these pictures are extracted from Materials Studio,[8] the visualization software employed in this study.

All three alkanes shown in figure 5.1 fit the straight channels of *MFI* occupying the central, and therefore more spacious part of the pore: the internal framework system is also highlighted (figure 5.1(d)) in a two-sided surface view, where the brighter colour shows the inner side of the channel.

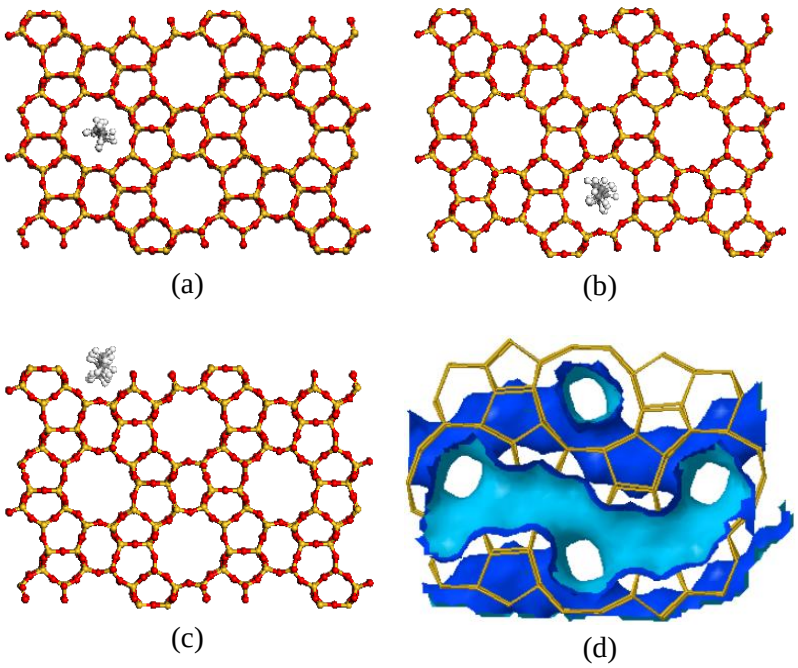

Figure 5.1. (a) *Hexane*, (b) *octane* and (c) *decane* adsorbed inside *MFI* (key: silicon atoms are yellow, oxygen atoms are red, carbon atoms are grey, and hydrogen atoms are white); (d) detail of *MFI* channel system surfaces: lighter blue is the channel internal face – Si atoms framework only displayed.

From these snapshots, it is possible to appreciate the extent of the possibility of clashes during the docking stage in a system where sinusoidal channels cross straight channels; also, one could observe that the straight channels, which also have a smaller cross section, seem to promote adsorption as their geometry may make a better match with the low energy *all-trans* conformation of the alkanes.

The same type of considerations made for *MFI* can be extended to *MFS* (figure 5.2). The two zeolites have similar channel systems (figure 5.2(d) and figure 5.3(d)) where larger straight channels are made in communication with one another by sinusoidal interconnecting channels, which are of smaller diameter in *MFS* (chapter 2). In particular for this zeolite, these smaller channels have also side pockets that are not found inside *MFI* sinusoidal channels.

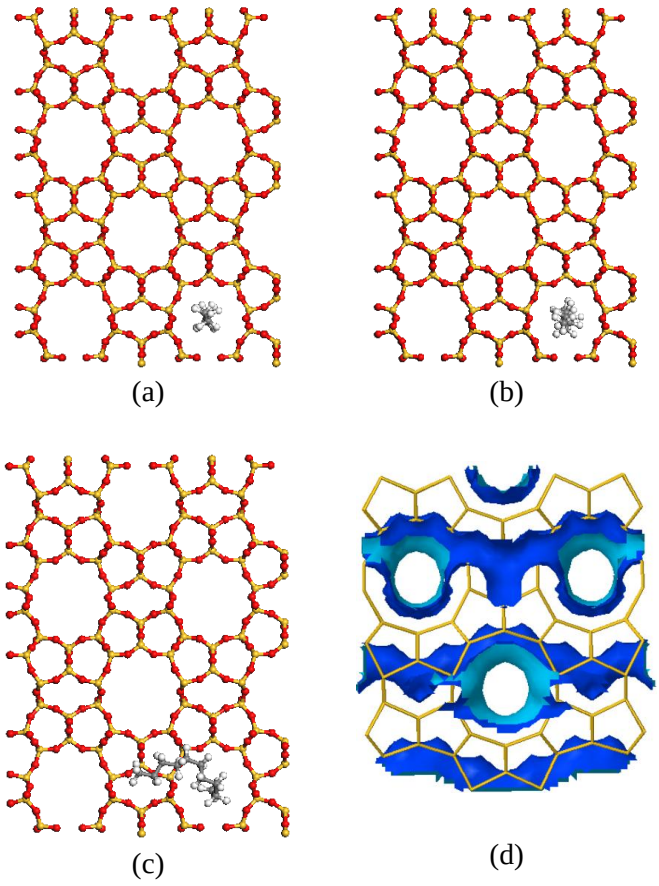

Figure 5.2. (a) *Hexane*, (b) *octane* and (c) *decane* adsorbed inside *MFS* (key: silicon atoms are yellow, oxygen atoms are red, carbon atoms are grey, and hydrogen atoms are white); (d) detail of *MFS* channel system surfaces: brighter blue is the channel internal face – Si atoms framework only displayed.

Nevertheless, because of the use of random numbers in these calculations, reaching the same final docking configurations is not certain. Proof of that is the case of *decane* (figure 5.2(c)) that seems to have adsorbed inside an *MFS* sinusoidal channel, indicating that the favourable interactions with the internal walls can compensate for the unfavourable gauche conformations of the alkane C– C– C– C dihedral angles.

The *MOR* zeolite framework (figure 5.3) contains wider and more linear channels (6.5 Å × 7.0 Å and 2.6 Å × 5.7 Å) compared to *MFI* (5.3 Å × 5.6 Å and 5.1 Å × 5.5 Å) and *MFS* (4.8 Å × 3.3 Å and 5.1 Å × 5.4 Å), which are also interconnected to each other by tight sinusoidal passages. Consistent with the very limited space

available in these smaller channels, none of the three alkanes were found inside them at the end of the MC runs.

A monitoring study (chapter 4) of the distance between the alkane C atoms and each of the Si and O atoms composing the zeolites internal walls (C_{alkane}–$O_{zeolite}$ and C_{alkane}–$Si_{zeolite}$) was carried out at two different temperatures, *i.e.* 350K and 500K. Figures 5.5 to 5.9 show the results for the study conducted at 350K.

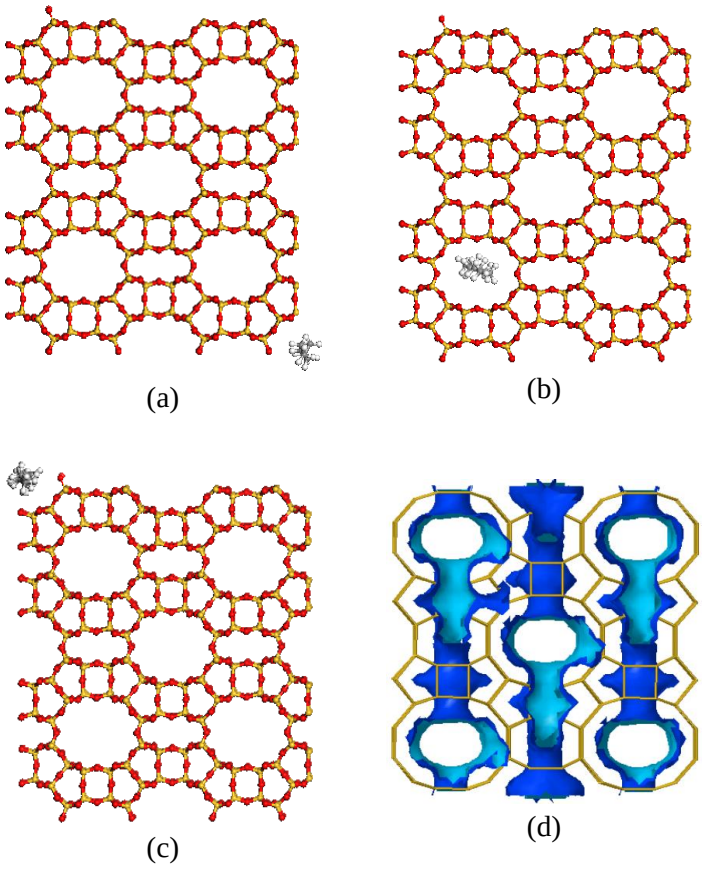

Figure 5.3. (a) *Hexane*, (b) *octane* and (c) *decane* adsorbed inside *MOR* (key: silicon atoms are yellow, oxygen atoms are red, carbon atoms are grey, and hydrogen atoms are white); (d) detail of *MOR* channel system surfaces: brighter blue is the channel internal face – Si atoms framework only displayed.

By monitoring the alkane terminal C atom positions and comparing those with the positions of C atoms belonging to the methylene groups in second position along the chain, it was possible to estimate the role that the shape of zeolite channels has

within the oxidation regioselectivity. In fact, from the findings of this study one can observe what is known as *pore effect*, a topic discussed in section 5.4.

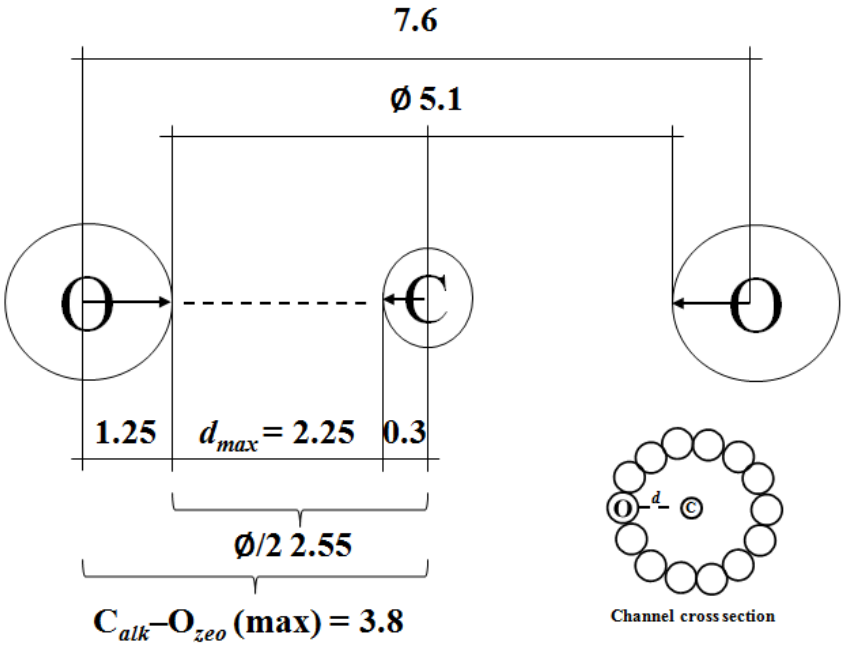

Figure 5.4. Drawing of the interatomic distances between guest C atoms and host O atoms (including ionic radius of each atom) within an *MFI* channel of (5.1 × 5.5) Å dimensions, where one of the two diameters only (Ø 5.1 Å) is displayed. *Right corner*: a zeolite channel cross section with one guest C atom in the middle.

As shown in figure 5.4 (refer to general scheme of figure 4.1), the distance C_{alkane}–$O_{zeolite}$ is the result of the sum of both O and C ionic radii (r_O and r_C, respectively) and a gap distance d between the two atoms. C_{alkane}–$O_{zeolite}$ can vary between a minimum and a maximum value. The minimum value (d = 0) is equivalent to the sum of r_O and r_C[9] (C–O_{min} = 1.55 Å). The maximum value (d_{max}), *i.e.* C–O_{max}, corresponds to the case where the alkane C atom is located at the centre of the zeolite channel, therefore is a function of the zeolite dimensions.

The results of the monitoring study found for the *hexane/MFI* system (figure 5.5(a) and (b)) are also observed when *hexane* is inside *MFS* (figure 5.6(c) and (d)) and *MOR* (figure 5.8(a) and (b)), or for systems where alkanes with longer chains are studied in those zeolites: *octane* in *MFI* (figure 5.5(c) and (d)), *MFS* (figure 5.7(a) and (b)) and *MOR* (figure 5.8(c) and (d)), and *decane* in *MFI* (figure 5.6(a) and (b)) *MFS* (figure 5.7(c) and (d)) and *MOR* (figure 5.9(a) and (b)).

The structures of the three alkanes, despite having a different number of C atoms, show consistent geometric features: they all have a C_2 rotation axis which allows each molecule to have the exact same initial position after rotations of 180° around the axis. With respect to the alkane adsorption occurring within a zeolite, this symmetry property makes the two terminal C atoms equivalent in all the adsorbates considered because they both have the same probability to get closer to the channels walls; the same stands with the two methylene C atoms in second position, and so on. In the diagrams of figures 5.5 to 5.9, the terminal pairs are labelled as C1/C6 for *hexane*, C1/C8 for *octane* and C1/C10 for *decane* while the internal C atoms are labelled according to their position along the chain, so the second positions are C2/C5 for *hexane*, C2/C7 for *octane* and C2/C9 for *decane*. To keep track of each atom in the plots, and also to highlight the symmetry features just discussed, where the atoms of a pair are equivalent, identical lines styles were assigned to the atoms of each pair.

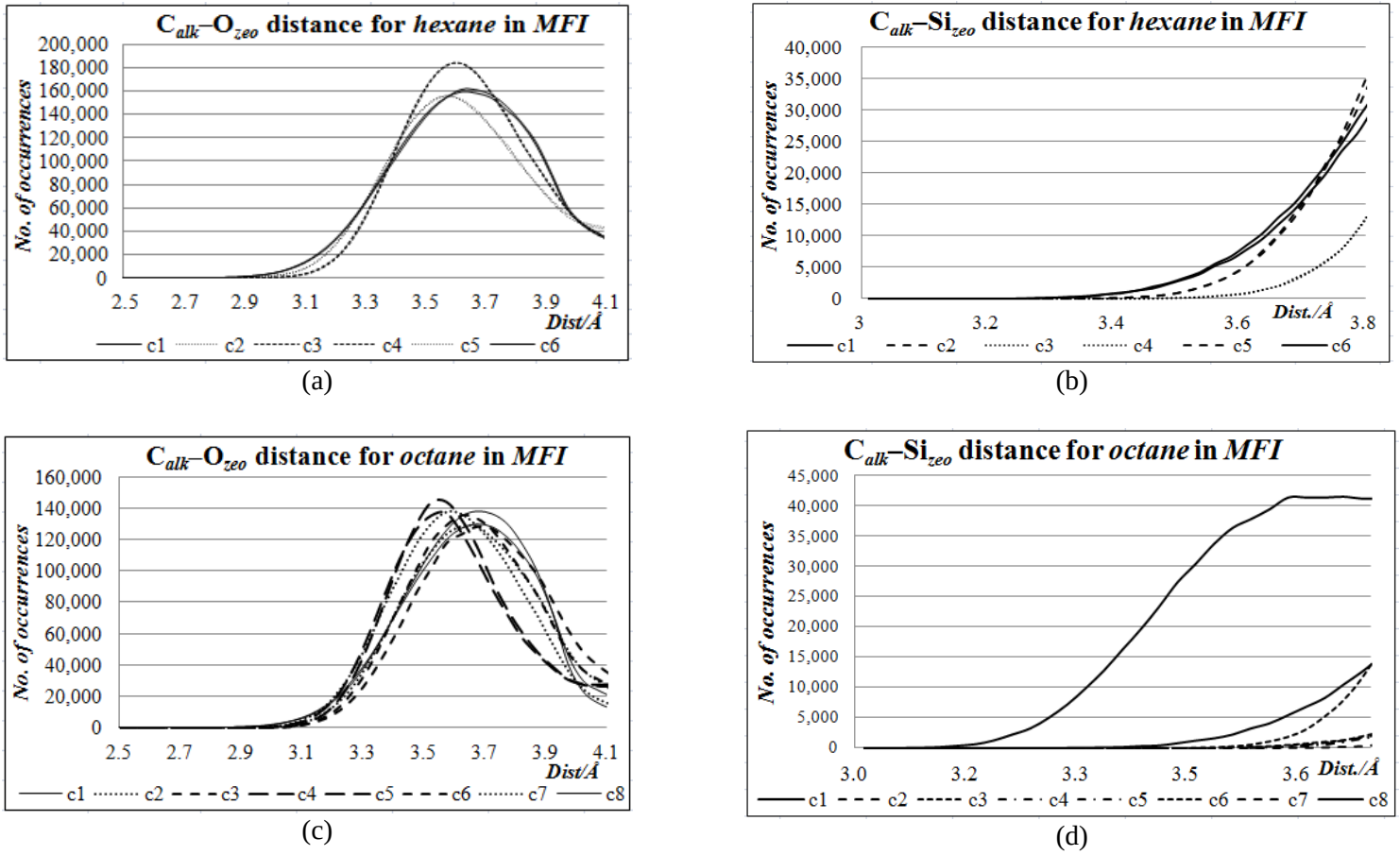

Figure 5.5. C_{alk}–O_{zeo} and C_{alk}–Si_{zeo} distances monitored during MC calculations (350K) for *hexane* in *MFI* ((a) and (b)) and *octane* in *MFI* ((c) and (d)), respectively.

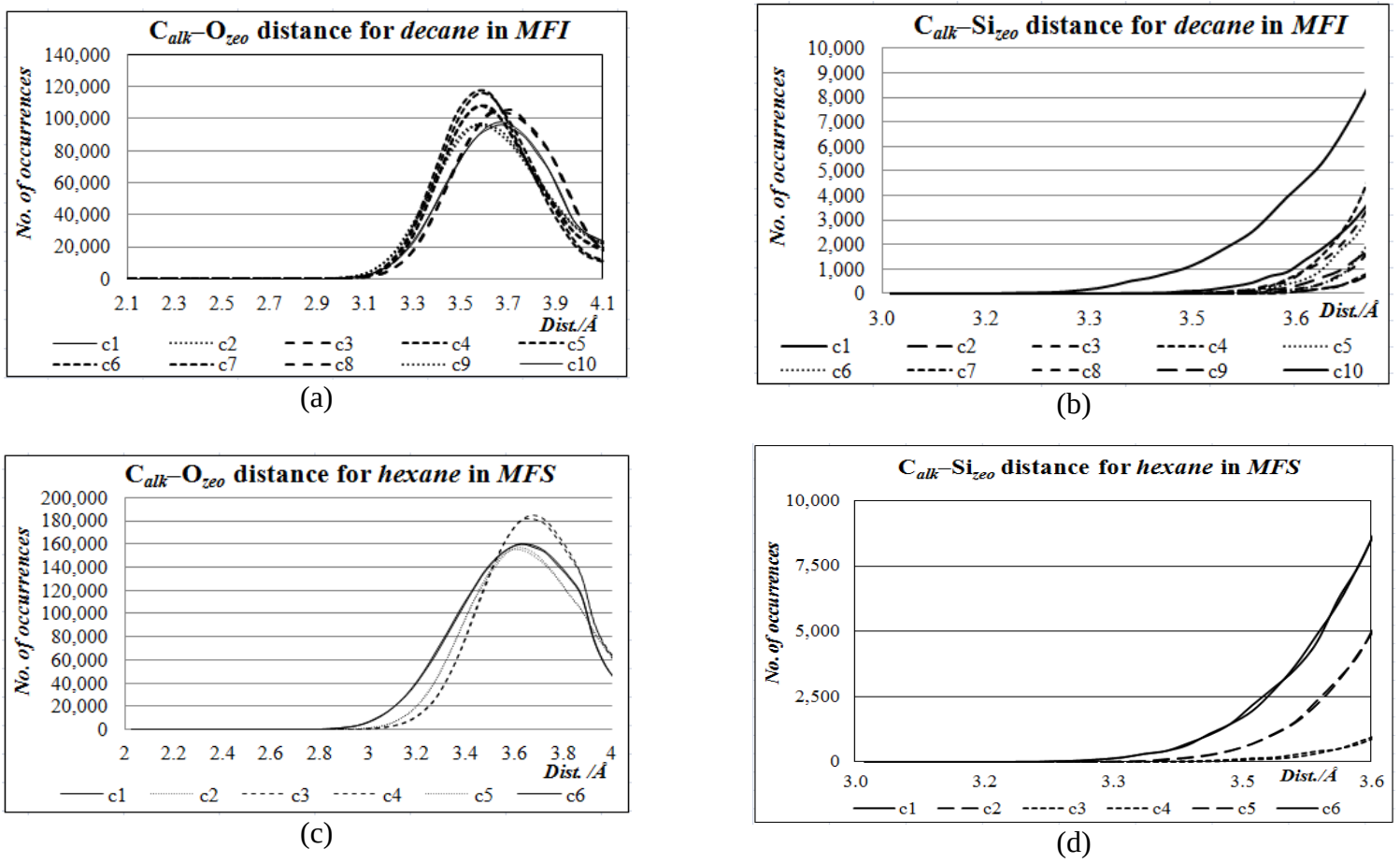

Figure 5.6. C_{alk}–O_{zeo} and C_{alk}–Si_{zeo} distances monitored during MC calculations (350K) for *decane* in *MFI* ((a) and (b)) and *hexane* in *MFS* ((c) and (d)), respectively.

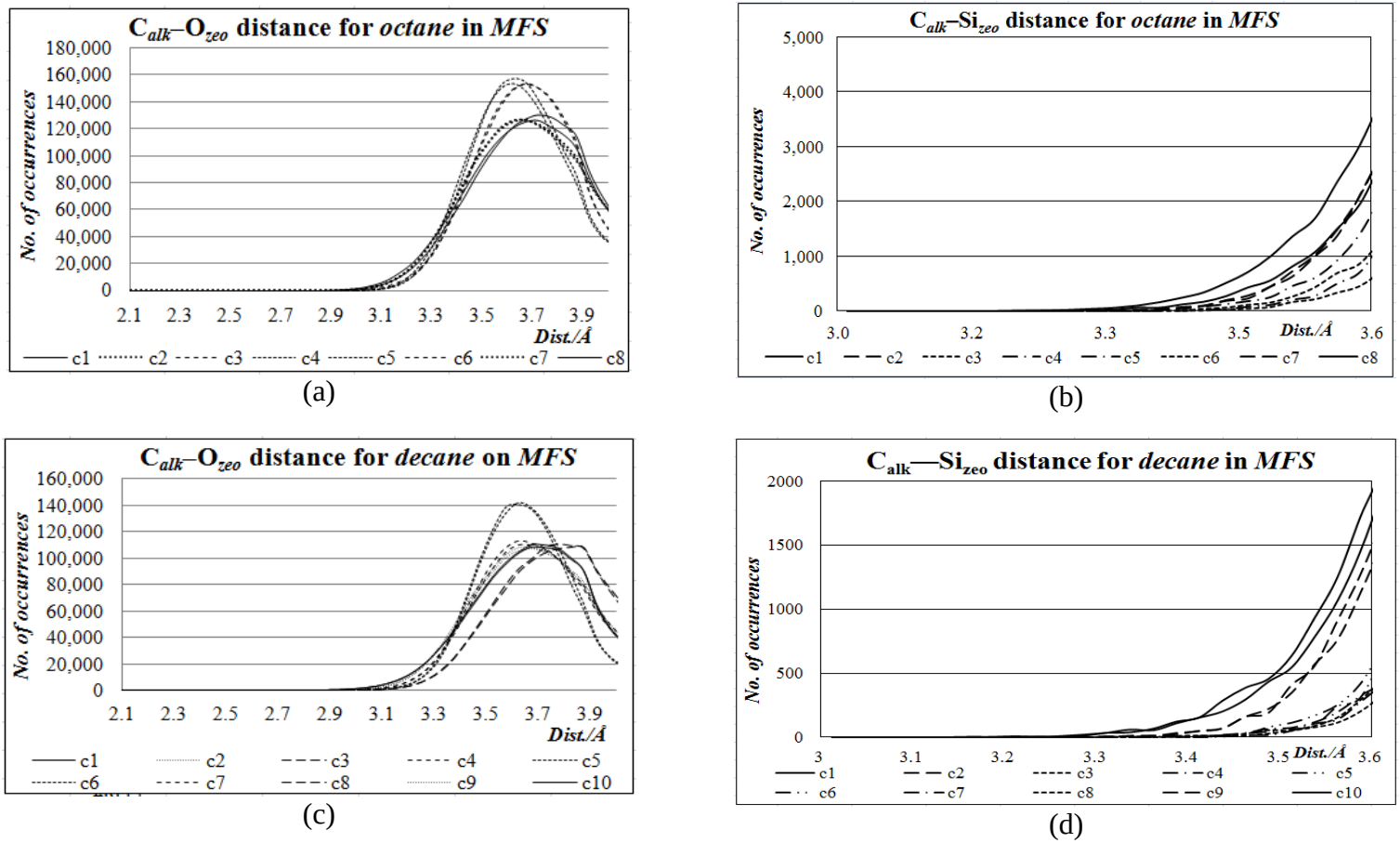

Figure 5.7. C_{alk}–O_{zeo} and C_{alk}–Si_{zeo} distances monitored during MC calculations (350K) for *octane* in *MFS* ((a) and (b)) and *decane* in *MFS* ((c) and (d)), respectively.

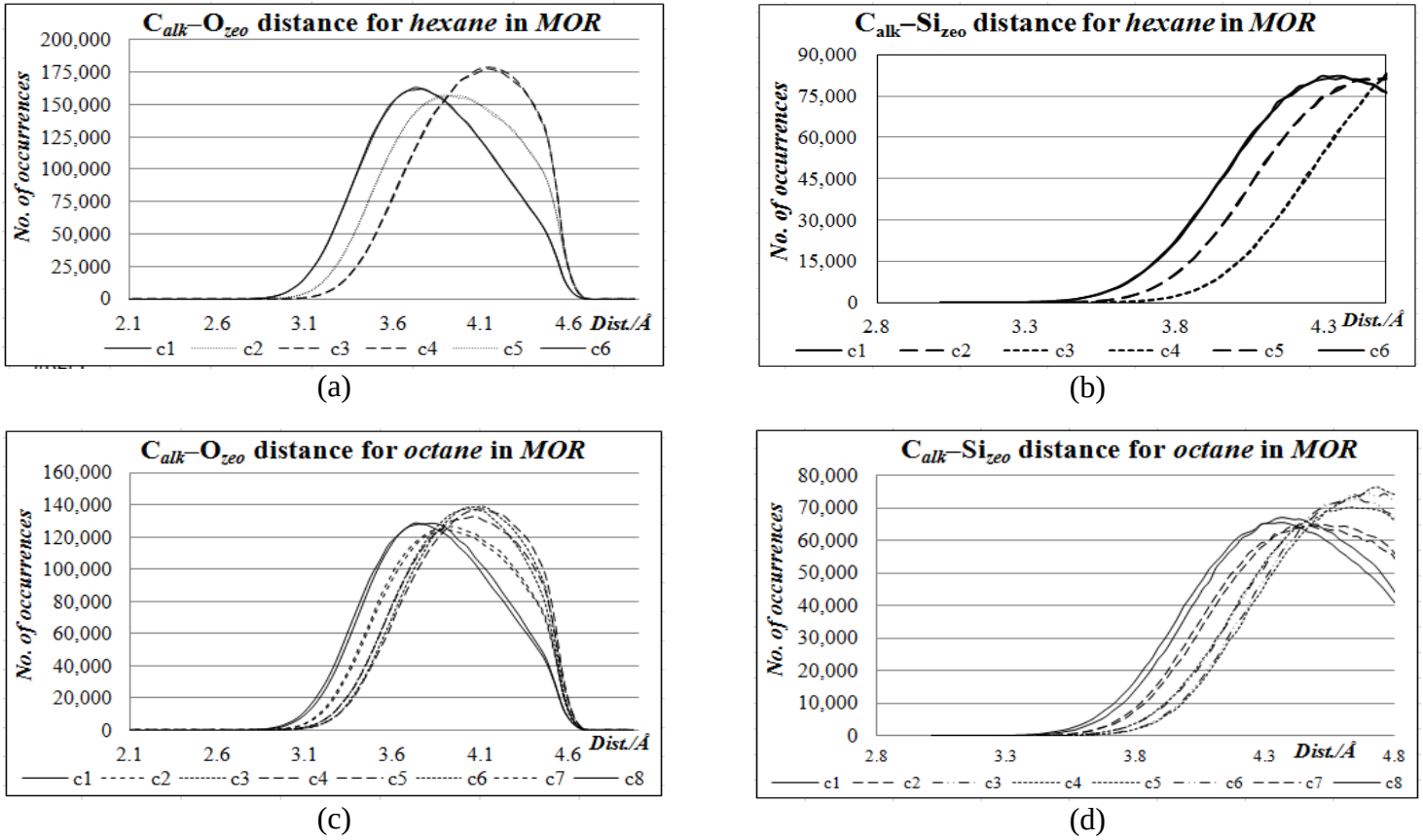

Figure 5.8. C_{alk}–O_{zeo} and C_{alk}–Si_{zeo} distances monitored during MC calculations (350K) for *hexane* in *MOR* ((a) and (b)) and *octane* in *MOR* ((c) and (d)), respectively.

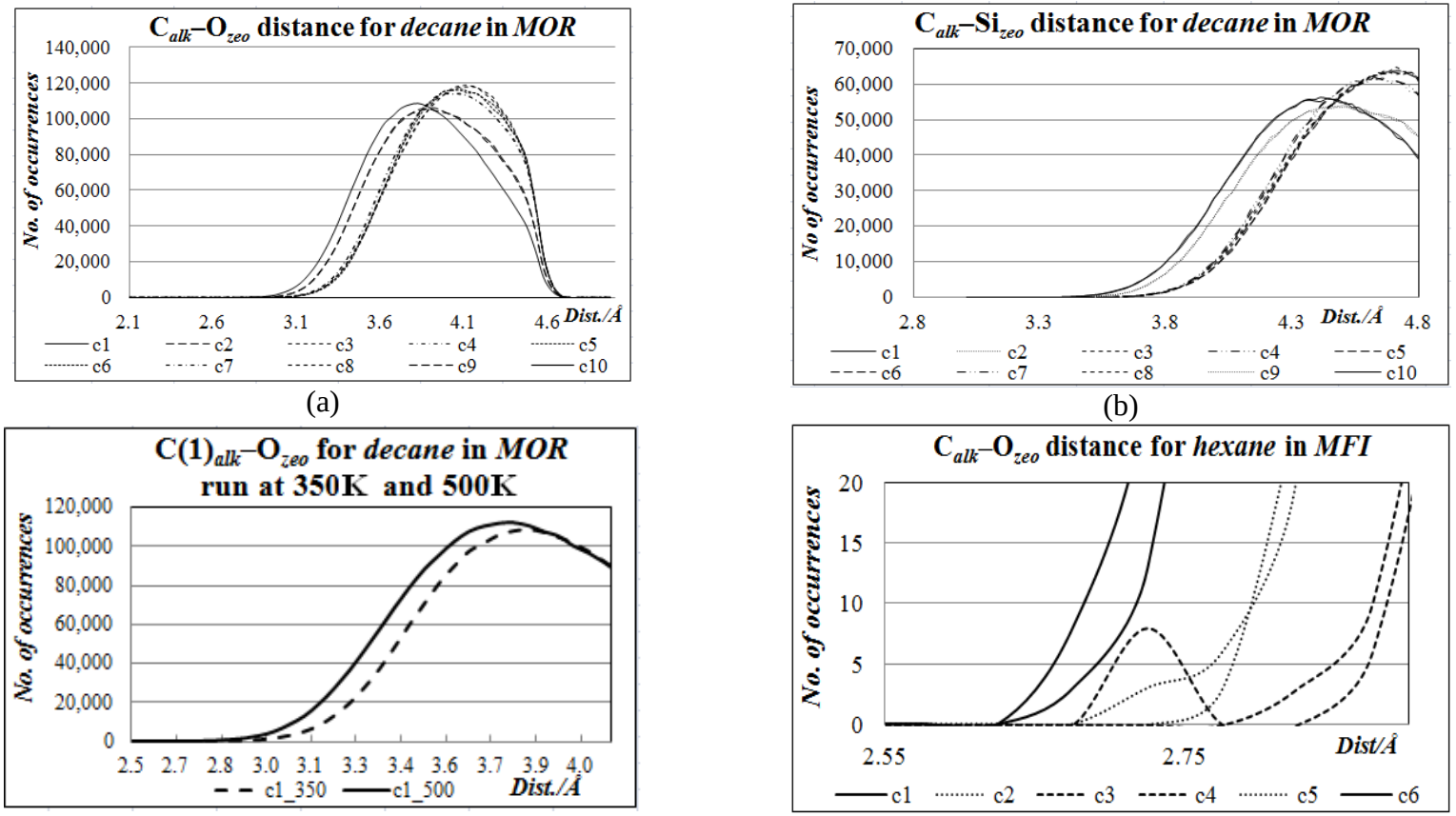

Figure 5.9. C_{alk}–O_{zeo} (a) and C_{alk}–Si_{zeo} (b) distances monitored during MC calculations (350K) for *decane* in *MOR*. (c) Comparison between distance $C(1)_{alk}$–O_{zeo}, where C(1) is *decane* primary C atom, run at 350K and 500K. (d) *First contact* distances visualized in the *hexane/MFI* system.

The *first contact* distance is the minimum distance at which the relevant alkane C atom is positioned from the zeolite O (or Si) atom. In the diagrams of figures 5.5 to 5.9, the first contact distance is the distance corresponding to the start of the plot rise from the left. Within the C_{alkane}–$O_{zeolite}$ monitoring study, from the comparison of the first contact distances between the three systems where the alkane is *hexane* (table 5.2), it is possible to notice that the substrate terminal atoms, namely "C1" and "C6", are closer to the walls than the two methylene C atoms (second position from both sides of the chain), namely "C2" and "C5", in all three zeolites. The same is observed for *octane* and *decane* inside the three zeolites (data not shown here).

Table 5.2. C_{alk}-O_{zeo} *first contact* distances (Å) for *hexane* terminal (C1/C2) and methylene (C2/C5) C atoms inside the three zeolites studied (350K).

hexane	C1	C2	C5	C6
MFI	2.675	2.725	2.775	2.675
MFS	2.675	2.825	2.775	2.575
MOR	2.625	2.775	2.775	2.525

The plots confirm this observation as the lines of the terminal pairs are always above all the other lines. This indicates that, during the calculation, the probability to find the substrate terminal C atoms closer to the pore walls is higher than that for the C atoms at other positions along the chain. Consistent with this is the fact that the lines of the secondary pairs are below the terminal lines but generally above all the others for short C_{alk}–O_{zeo} (or C_{alk}–Si_{zeo}) distances (figure 5.9(d)).

The results of the same study carried out at 500K (not shown here) describe the same patterns, where the terminal C atoms for all alkanes considered are closer to the walls than the secondary C atoms, as shown in one C_{alk}–O_{zeo} example in figure 5.9(c). In this example *decane* is inside *MOR* and it is noticeable that the alkane terminal C atom is ~0.2 Å closer to the zeolitic wall at 500K than it is at 350K.

Although each plot profile is different from the others, due to the different zeolite structure considered in each case (*i.e.* pore shape, channels layout *etc.*), and different alkane chain lengths are considered, common elements can be identified between all

the patterns and they can be considered as a rough indication of the internal surfaces complexity.

Taking as an example *hexane*, in the comparison between the results of the alkane C_{alkane}–$O_{zeolite}$ monitoring study when inside *MFI*, *MFS* and *MOR* (figure 5.5(a), figure 5.6(c) and figure 5.8(a)), a gradually larger separation between the paired plots of the C atom types is noticeable. This may reflect the fact that *MFI* has wide sinusoidal channels that cross its straight channels (figure 5.1(d)), *MFS* has sinusoidal channels with a small cross section (figure 5.2(d)) and that *MOR* has small straight channels crossing large straight channels (figure 5.3(d)). The degree of how much a crossing channel is sinusoidal may be an indication of the overall channel system linearity for the three zeolites. *MFI* represents the lowest level of linearity as its sinusoidal channels have a larger cross section than its straight channels have and therefore the former channels may be more likely to host alkanes than the latter ones. Instead, *MOR* represents the maximum level of linearity because all its channels are straight. *MFS*, with its smaller sinusoidal channels, is somewhere in between the two. Inside *MFI*, *Zebedde* may be forced to perform further alkane structure changes to sample better host-guest fits and avoid steric clashes. The new configurations sampled will contain gauche conformations for some of the C–C–C–C dihedral angles and so this will expose the C2 atoms to the walls more readily. This may be the reason for the very near plots in figure 5.5(a). Inside *MOR*, the paired plots of figure 5.8(a) are neatly separated from each other and this may indicate that the *hexane* configurations sampled inside *MOR* do not expose those internal methylene C atoms as much as they do inside *MFI*, while *MFS* is (again) somewhere in between the two other zeolites (figure 5.6(c)). The patterns just described for the C_{alkane}–$O_{zeolite}$ study are confirmed by what is observed for the C_{alkane}–$Si_{zeolite}$ study of *hexane* inside *MFI*, *MFS* and *MOR*. Here too, *MFI* is the zeolite that causes the plots to get closer (figure 5.5(b)), or even overlap, due to the low element of linearity of its channel system. Instead, for the *MFS* (figure 5.6(d)) and *MOR* (figure 5.8(b)), the plot separation is larger due to the increasing element of linearity discussed, as expected.

With the introduction of a further variable into the discussion, *i.e.* the alkane chain length, the overall complexity of the host-guest interactions is increased, although similar patterns to those highlighted above may be observed.

In the C_{alkane}–$O_{zeolite}$ study of *MFI* containing *hexane*, *octane* and *decane* (figure 5.5(a), (c) and figure 5.6(a), respectively), the effect of the presence of large sinusoidal channels, as discussed earlier, can be observed. In fact, the low linearity element of this zeolite does not allow a clear separation between the paired plots for any of the alkanes considered. Obviously, results for a longer chain are reflected in a more complex plot because more atoms take part in the competition between terminal and methylene C atoms.

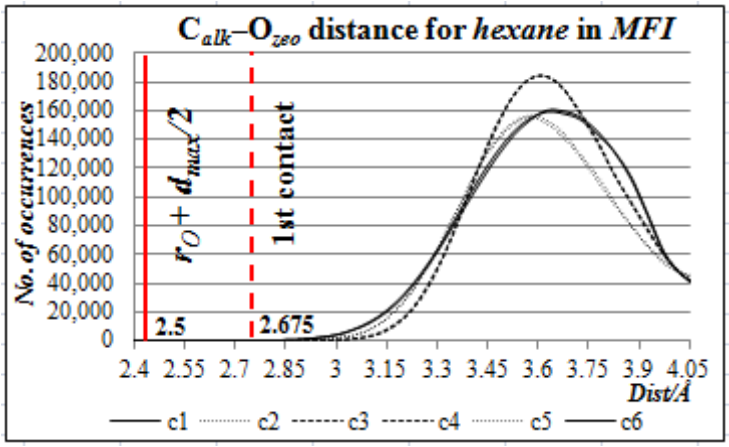

(a)

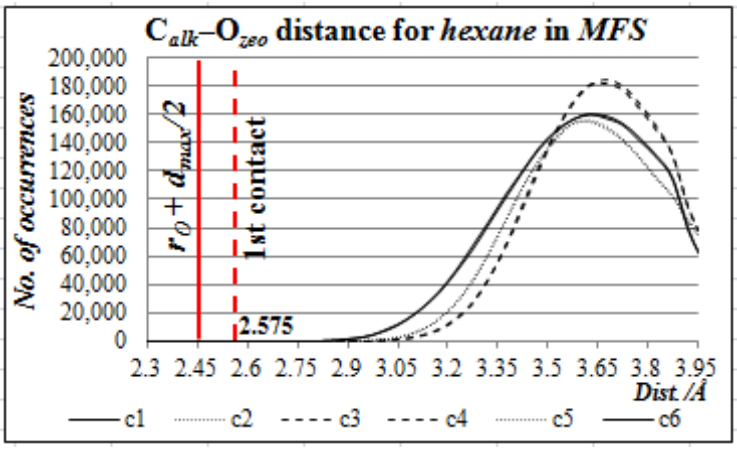

(b)

Figure 5.10. Plots for the C_{alkane}–$O_{zeolite}$ distance monitored inside *MFI* (a) and *MFS* (b) showing similarities in the location where the first contact host-guest occurs, *i.e.* closer to the centre of the respective channels.

A further evidence of the more uniform landscape inside *MOR* zeolites may be provided by the comparison between the early stages of the MC calculations. Data relative to the *first contact* distance in the different systems may be used to confirm *MOR* channel system linearity. In all host-guest systems studied here, the distance *d* (figure 4.1) indicates the gap between host and guest atoms monitored at their contact. If $d > d_{max}/2$, the contact host-guest occurs when the alkane C atom is closer to the middle of the channel and if $d < d_{max}/2$ the contact occurs in locations closer to the wall. Figure 5.10(a) highlights both first contact distance (red dotted vertical line labelled "1st contact") at 2.675 Å for *hexane* in *MFI* and the middle of the gap *d* (red vertical line labelled "$r_O + d_{max}/2$"), which is the sum of the O ionic radius (1.25 Å)[9] and the distance $d_{max}/2$. This corresponds to a *d* value of 1.425 Å and to a $d_{max}/2$ value of 1.25 Å. This means that substrate first contact with *MFI* wall occurs in a location closer to the middle of the channel. When *hexane* is inside *MFS*, the first contact C_{alk}–O_{zeo} distance is 2.575 Å ("1st contact" in figure 5.10(b)), which corresponds to a *d* value of 1.325 Å and a $d_{max}/2$ value of 1.2 Å. This indicates that also for *MFS* the first contact host-guest occurs closer to the middle of the channel.

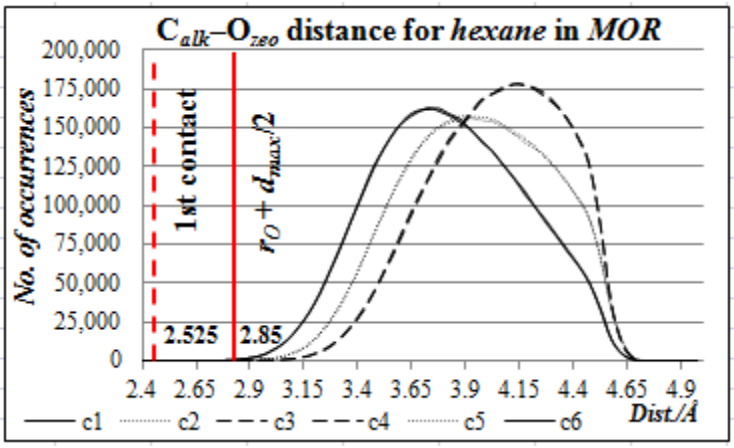

Figure 5.11. Plot for the C_{alkane}–$O_{zeolite}$ distance monitored inside *MOR* showing that the location where the first contact host-guest occurs is closer to the zeolitic walls.

As anticipated above, the wide straight channels in *MOR* are interconnected by small straight channels. This means that the results of the monitoring study for this zeolite do not reflect a combination of straight and sinusoidal channels. For this reason,

MOR is a more linear system. In fact, the first contact C_{alk}–O_{zeo} distance of *hexane* in *MOR* is equal to 2.525 Å ("1st contact" in figure 5.11). This corresponds to a *d* value of 1.275 Å and a $d_{max}/2$ value for the zeolite is 1.6 Å. This means that *MOR* is the only zeolite of the three to have a first contact host-guest closer to the wall than to the middle of the channel. This may indicate that no extra alkane configurations are required to adapt the chains to the sinusoidal channels layout. Instead, in *MFI* and *MFS*, the further readjustments to the chains create wider gaps between the alkane terminal C atoms and the walls to push the former towards the centre of the latter.

By showing the probability of each guest atom to be at a certain distance from each host atom, both the C_{alkane}–$O_{zeolite}$ and C_{alkane}–$Si_{zeolite}$ studies provide a qualitative understanding of the interactions occurring during a MC calculation between alkane and internal zeolitic walls, but the results of the former exercise give a further important feedback that may be able to help in qualitatively investigating the mechanism of the reaction considered in the different systems analyzed.

Table 5.3. First contact distances sourced by the $\mathbf{C_{alk}}$–$\mathbf{O_{zeo}}$ and $\mathbf{C_{alk}}$–$\mathbf{Si_{zeo}}$ monitoring studies run at 350K for all the host-guest systems studied in this project. The first contact distance is the sum of oxygen ionic radius (1.25 Å)[9] and the first contact distance *d* (section 4).

		MFI	*MFS*	*MOR*
hexane	C_{alk}–O_{zeo}	2.675	2.575	2.525
	C_{alk}–Si_{zeo}	3.0875	3.1625	3.0875
octane	C_{alk}–O_{zeo}	2.775	2.725	2.675
	C_{alk}–Si_{zeo}	3.0125	3.1625	3.1875
decane	C_{alk}–O_{zeo}	2.725	2.625	2.625
	C_{alk}–Si_{zeo}	3.1125	3.1375	3.1625

Within an Al-exchanged zeolite, the acid T-site is represented by the hydroxyl (OH) group bridging a Si atom and an Al atom: the oxygen atom is the Brønsted acid site with which the terminal alkane carbon atom is more likely to establish an interaction, as shown by table 5.3 (alkanes make first contact with the zeolite O atoms at 0.4653 Å shorter distances on average at 350K than what they do with the Si atoms), while

the associated H atom counter balances the network negative charge due to the Al atom being exchanged with a pore Si atom. From these considerations, it is clear that the zeolitic oxygen atom, and its distance from the alkane C atoms, plays a fundamental role in the alkane adsorption and reaction.

5.4 Terminal Selectivity Effect

Exploring the changes of the C_{alkane}–$O_{zeolite}$ distance during a MC sampling calculation provided a platform of data that allowed a reactivity study to be undertaken and that produced the plots shown in figures 5.12 to 5.14, for calculations run at 350K, and in figures 5.15 and 5.16, for calculations run at 500K (refer to chapter 4 for k_{prim}/k_{sec} calculation). Reactivity of primary and secondary carbon atoms for all the alkanes considered in this study, are compared.

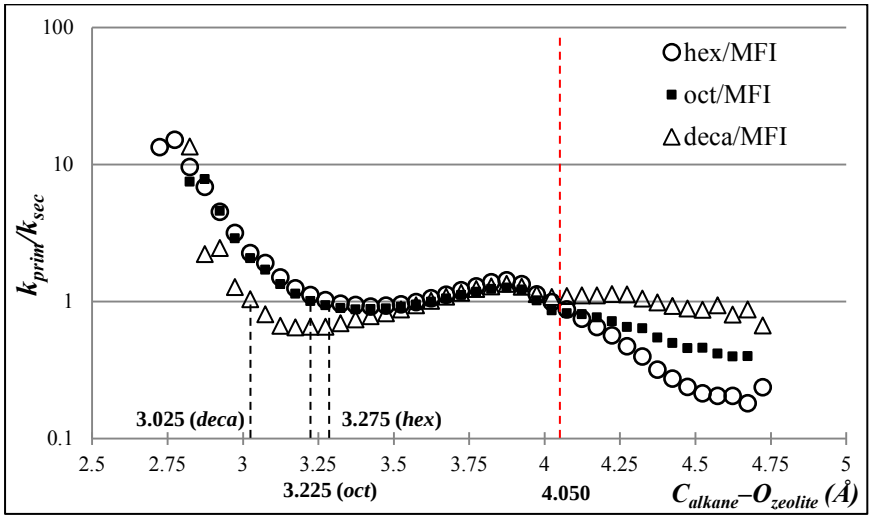

Figure 5.12. Estimation of the pore effect for *hexane*, *octane* and *decane* inside *MFI* at 350K. The dotted red line highlights the C–O_{max} distance which is the higher limit of the *reactivity window*: it corresponds to the alkane C atom in the middle of the zeolite channel (figure 4.1). The black dotted lines highlight the C_{alk}–O_{zeo} distances at which terminal positions are favoured for each alkane.

The drawing in figure 4.1 can be taken as a reference to help understand what information to gather from the plots. As anticipated above in this chapter, the distances C–O_{min} and C–O_{max} identify a *reactivity window*. In the plots of figures 5.12 to 5.16, the C–O_{max} distance is flagged by a vertical red dotted line, therefore whatever is detected over this line is not relevant to this reactivity discussion because C atoms at this distance must actually be closer to other framework atoms. Within the reactivity window, the guest molecules react preferentially at the terminal C atoms because the corresponding plots are observed at k_{prim}/k_{sec} values greater than the unity.

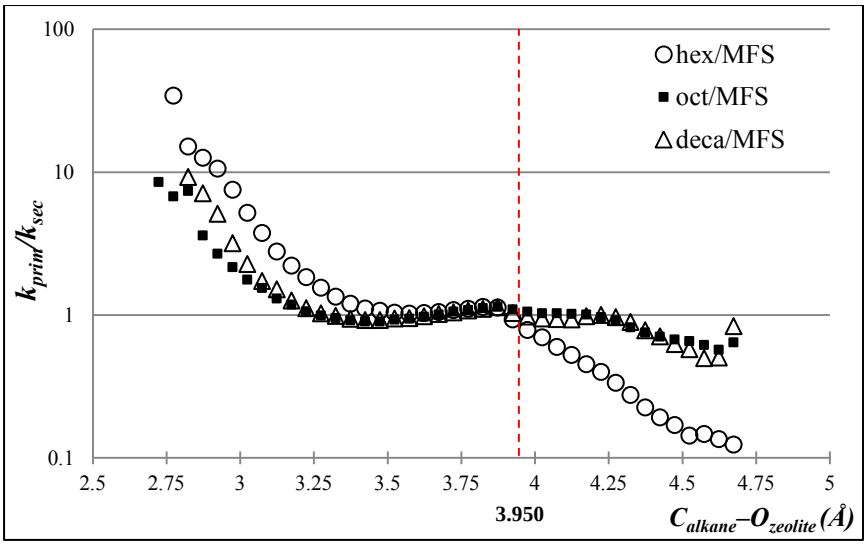

Figure 5.13. Estimation of the pore effect for *hexane*, *octane* and *decane* inside *MFS* at 350K. The dotted red line highlights the C–O_{max} distance which is the higher limit of the *reactivity window*: it corresponds to the alkane C atom in the middle of the zeolite channel (figure 4.1).

As described in chapter 4, k_{prim} is the calculated terminal reaction constant and k_{sec} is the reaction constant relative to the two methylene C atoms attached to the terminal C atoms, *i.e.* in position two from both chain ends where the ends are the position one.

Figure 5.12 shows that, at 350K, *hexane* preferentially reacts in *MFI* at terminal C atoms for C_{alkane}–$O_{zeolite}$ ≤ 3.275 Å. The right hand side (black vertical dotted) line identifies the distance from the wall at which *hexane* is preferentially oxidized at terminal positions, which is where the (empty circles) marks on the diagram cross the k_{prim}/k_{sec} unity line. The same occurs for *octane* at C_{alk}–O_{zeo} ≤ 3.225 Å (see middle black vertical dotted line), and for *decane* at C_{alk}–O_{zeo} ≤ 3.025 Å (see left hand side black vertical dotted line). *MFI* also shows some selectivity for the *hexane* and *octane* than it does for *decane*. This can be observed by the gap between the corresponding plots where the former two alkanes have higher k_{prim}/k_{sec} values than the latter.

Figure 5.13 shows the results of the same calculation at 350K inside *MFS*. In particular, for this host/guest system, *hexane* reacts at terminal positions for C_{alk}–O_{zeo} ≤ 3.575 Å (not shown on the diagram). In the same diagram, *octane* reacts at the

terminal C atoms for C_{alk}–$O_{zeo} \leq 3.225$ Å and *decane* does the same for C_{alk}–$O_{zeo} \leq 3.025$ Å.

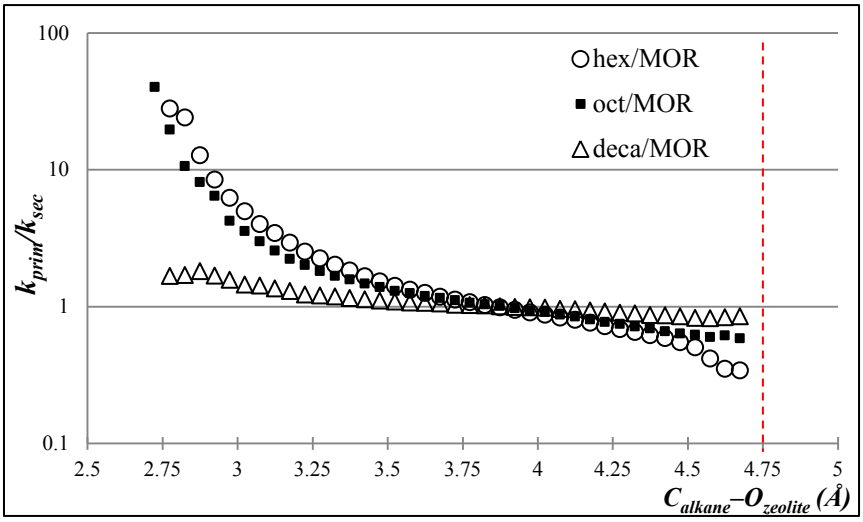

Figure 5.14. Estimation of the pore effect for *hexane*, *octane* and *decane* inside *MOR* at 350K. The dotted red line highlights the C–O_{max} distance which is the higher limit of the *reactivity window*: it corresponds to the alkane C atom in the middle of the zeolite channel (figure 4.1).

Noticeable from these data is that *octane* and *decane* react at terminal C atoms for the same C_{alk}–O_{zeo} values when they are inside *MFI* and *MFS*, which is consistent with the similarity in channel dimensions of the two zeolites (chapter 2): in fact, (5.3 × 5.6) Å and (5.1 × 5.5) Å are *MFI* channel dimensions and (4.8 × 3.3) Å and (5.1 × 5.4) Å are those of *MFS*, with one matching straight channels aperture, *i.e.* 5.1 Å. Differently to the *MFI* case, a very small gap between the *hexane* plot and that of the *octane*/*decane* pair may be observed, although this may not necessarily translate into a selectivity of *MFS* for *hexane*.

Figure 5.14 shows the plot for the alkanes reacting at 350K inside *MOR*. All three guest molecules seem to react preferentially at terminal C atoms in correspondence of C_{alkane}–$O_{zeolite} \leq 3.875$ Å. This may be interpreted as a consequence of *MOR* high linearity for its channel system, as discussed earlier. The fact that *MOR* does not have sinusoidal intercommunicating channels where the alkanes would be hosted, the substrate methylene C atoms are not exposed as a result of further geometry alterations sampled by the *Zebedde* code. A further element to highlight is that *MOR*,

as well as *MFI*, shows a higher selectivity for *hexane* and *octane* than it does for *decane*, while *MFS* only shows a marginal selectivity for *hexane*.

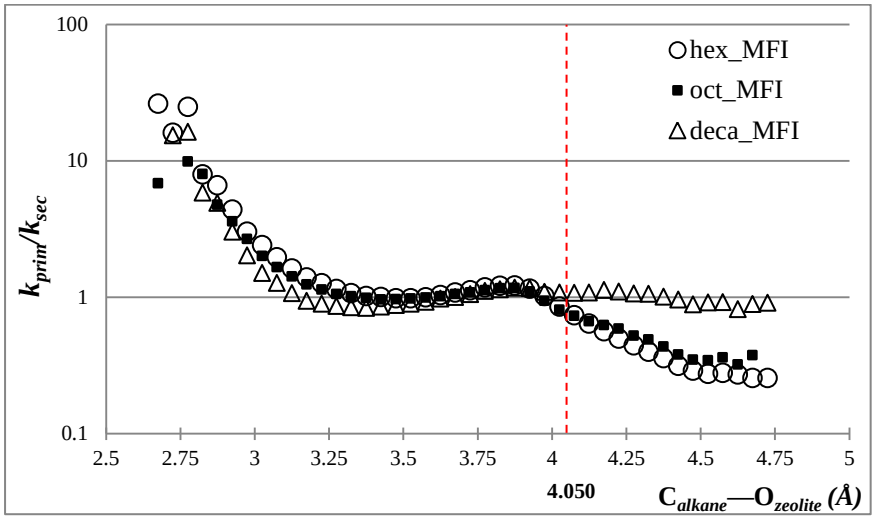

Figure 5.15. Estimation of the pore effect for *hexane*, *octane* and *decane* inside *MFI* at 500K. The dotted red line highlights the C–O_{max} distance which is the higher limit of the *reactivity window*: it corresponds to the alkane C atom in the middle of the zeolite channel (figure 4.1).

Calculations run at 500K in *MFI* for *hexane*, *octane* and *decane* (figure 5.15) show that terminal selectivity occurs at C_{alkane}–$O_{zeolite} \leq$ 3.425 Å, 3.325 Å and 3.125 Å, respectively. The selectivity that *MFI* showed for *hexane* and *octane* at a lower temperature has disappeared, as the overlapping of plots shows in the diagram.

In *MFS* (figure 5.16(a)) C_{alkane}–$O_{zeolite} \leq$ 3.525 Å (*hexane*), 3.325 Å (*octane*) and 3.525 Å (*decane*). Here too, *octane* C_{alkane}–$O_{zeolite}$ value matches the corresponding value in *MFI*. In this zeolite though, as it was noticed at lower temperature, a small gap between *octane*'s plot and the other plots may be observed. Here too though, this is far too marginal to be recognized as an element of *MFS* selectivity for *octane*.

In *MOR* (figure 5.16(b)), the three substrates at 500K preferentially react at the terminal C atoms for C_{alkane}–$O_{zeolite} \leq$ 3.875 Å, which is consistent with what was shown at 350K. A further similarity to the reaction in *MOR* at lower temperature is the selectivity of the zeolite for *hexane* and *octane*, noticeable for the wide gap between the plots of two alkanes from that of *decane*.

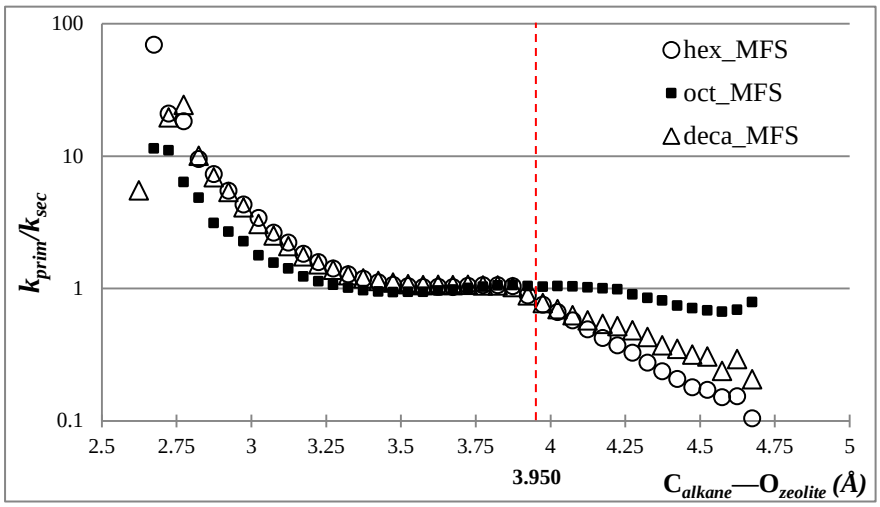

(a)

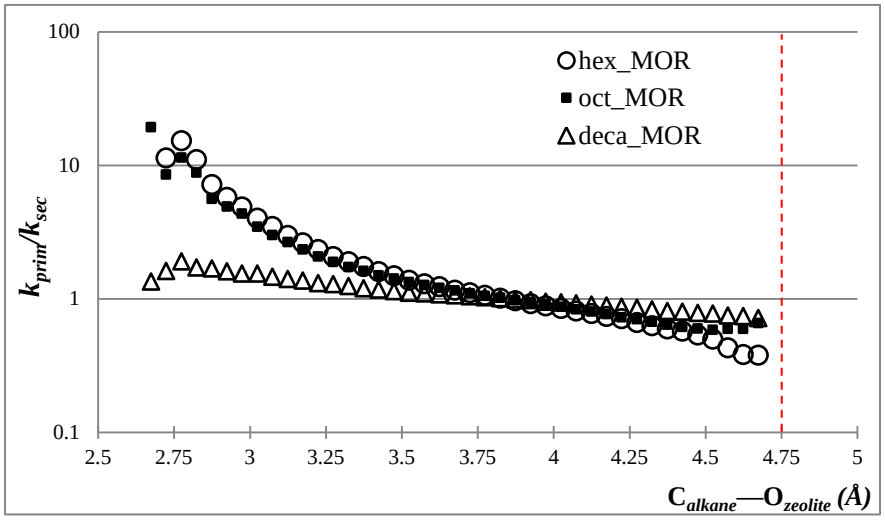

(b)

Figure 5.16. Estimation of the pore effect for *hexane*, *octane* and *decane* inside *MFS* (a) and *MOR* (b) at 500K. The dotted red line highlights the C–O_{max} distance which is the higher limit of the *reactivity window*: it corresponds to the alkane C atom in the middle of the zeolite channel (figure 4.1).

5.5 Conclusions

In each of the host-guest systems considered in this study, the Monte Carlo (MC) sampling of alkane configurations was stopped once the corresponding energy (E_{vdW}) reached an equilibrated level and the standard deviation demonstrated the sampled configurations formed an ensemble. From the energy point of view (table 5.1), one may observe that the interaction guest-host inside *MOR* is more constant through the different hydrocarbon chain lengths. This may indirectly confirm that *MFI* and *MFS* sinusoidal channels represent an element that does selection among the alkanes, in fact *decane* adsorption inside those channels (figure 5.2(c)) may be less favourable than that of *hexane* and *octane*. This also means that the contribution from the more stable *decane* conformation does not appear to compensate for the energetically costly clashes between the alkane and walls to the same extent that it does for the two shorter alkanes. Conversely, as discussed above, *MOR* has no sinusoidal channels, hence the more linear energetic profile.

The model introduced in chapter 4 (figure 4.1) and briefly re-discussed in this chapter for a specific example (figure 5.4) provided a necessary view to break down the geometrical features hidden within the results of the monitoring study and to further assess the *pore effect* from the results of the reactivity study that followed.

It is understood that more than one contribution to the results of both studies may have played a part in describing where and how host-guest interactions occur within the systems considered. The C_{alk}–O_{zeo} interaction seems to play a large part within the reactive scenario, more than the C_{alk}–Si_{zeo} does, as shown in table 5.3 and confirmed an example shown in figure 5.17, where *MFI* Si atoms appear farther than O atoms from the channel centre, and therefore from the alkane.

A further contribution is represented by the intrinsic stability of the alkane conformations that may (or may not) compensate for the interactions with the walls.

Since the MC calculations sampled configurations without any bias for the alkanes final position, the sinusoidal channels probably represents another contribution, at least within *MFI* and *MFS*.

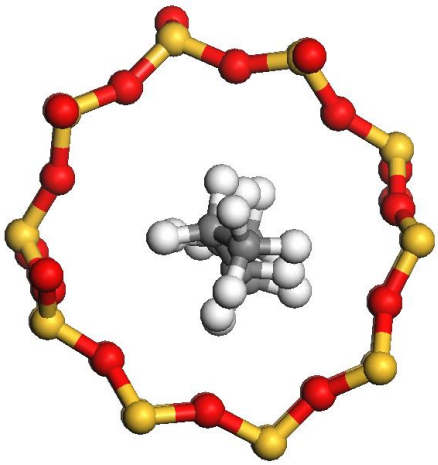

Figure 5.17. Detailed snapshot extracted from figure 5.1(a) of *hexane* adsorbed inside an *MFI* straight channel (key: silicon (Si) atoms are yellow, oxygen (O) atoms are red, carbon (C) atoms are grey, and hydrogen (H) atoms are white). The picture shows that Si atoms are farther than O atoms from the channel centre.

Their shape (and dimensions in *MFS*) may force alkanes' non linear configurations to be sampled, where internal C atoms are more exposed and therefore able to get closer to the walls. In turn, this may influence the shape of the plots in figures 5.12 to 5.16 where, although only at times, methylene C atoms appeared as likely as terminal C atoms to be closer to the zeolitic O atoms. Being the *pore effect* estimation based on the monitoring study results, the sinusoidal channel effect may also have an impact on the zeolites selectivity for specific alkanes or on the oxidation selectivity for specific positions in each alkane.

The change in temperature, *i.e.* from 350K to 500K, does not seem to have a large impact on the reactions studied. The $C_{alk}-O_{zeo}$ study detected that at higher temperature alkanes are slightly closer to the zeolitic wall. The reaction at 350K showed a good selectivity of two zeolites (*MFI* and *MOR*) for *hexane* and *octane*, while at 500K the same selectivity was only observed inside *MOR*. Generally, the results of these studies were in agreement with experimental observations: the terminal atoms in the guest molecule are more likely to be closer to the host system internal walls. This also agrees with the regioselectivity of the reaction occurring in zeolites, as highlighted by Iglesia *et al.* in their work.[2] Therefore, one could say that local constraints may force a closer contact between host atoms and guest terminal C

atoms that, being at the two ends of the molecule, may be more often freer to move than those further inside the chain. The plots shown in figure 5.12 to 5.16 simply describe the effect that the zeolitic internal structure exerts over the alkanes terminal and secondary adsorption, favouring the former within a distance range C_{alkane}–$O_{zeolite}$ that is characteristic of the zeolite chosen as a support. The k_{prim}/k_{sec} ratio defined within this study (chapter 4) does not take into account the fact that the terminal positions in linear alkanes are intrinsically less reactive than the secondary and tertiary positions; in fact, it is more energetically expensive to form a terminal radical than it is to form a secondary or tertiary. The patterns estimated in this study though do reproduce the unprecedented results that Iglesia and co-workers obtained in their work where they demonstrated[2] that the *shape selectivity* can be directed by the zeolitic channel shape.

The considerations made in this study in terms of reactivity are based on the assumption that the reaction of these species is a direct consequence of their interactions with the zeolitic walls and their adsorption at the most favourable T-sites, namely the pore walls O atoms. The calculations of this part of the study aimed at isolating that part of the catalyst that influences the selectivity so that the effect of the channel shape (*shape selectivity*) could be considered independently by any other aspect. This was deemed to be a fundamental first target in order to establish a contact with the experimental results.[2] After this contact was being established, further studies focussing on the actual mechanicistic details of the reaction investigated would have progressed.

References

[1] F. P. Guengerich *Chem. Res. Toxicol.*, **14**(6), 611 (2001).
[2] B.-Z. Zhan, E. Iglesia, B. Modén, J. Dakka, J. G. Santiesteban *J. Catal.*, **245**, 316 (2007).
[3] David R. Lide, ed., *CRC Handbook of Chemistry and Physics, Internet Version 2005,* <http://ww.hbcpnetbase.com>, CRC Press, Boca Raton, FL, 2005.
[4] M. D. Foster, I. Rivin, M. M. J. Treacy, O. Delgado Friedrichs *Micropor. Mesopor. Mat.*, **90**, 32-38 (2006).
[5] D. W. Lewis, D. J. Willock, C. R. A. Catlow, J. M. Thomas, G. J. Hutchings *Nature*, **382**, 604 (1996).
[6] C. R. A. Catlow, D. W. Lewis, C. M. Freeman *J. Phys. Chem*, **99**, 11194 (1995).
[7] J.-R. Hill, J. Sauer *J. Phys. Chem*, **99**, 9536-9550 (1995).
[8] Materials Studio v6.0 <http://accelrys.com/products/materials-studio/>.
[9] R. D. Shannon *Acta Cryst. A*, **32**, 751 (1976).

6. Propane activation on molybdena

This chapter describes the activation of propane on the MoO_3 (010) surface. The introduction on the subject is followed by the computational details and the results that are given in five sections concerning perfect and defective MoO_3(010) surfaces, perfect and defective $Fe_2(MoO_4)_3$ surfaces, H and propyl radical adsorption, H and isopropyl radical adsorption, and lastly C–H bond activation.

6.1 Introduction

The ability of transition metal centres to take part in a redox process is transferred to metal oxide surfaces in terms of the capability of these systems to be reduced during the oxidation of a substrate adsorbed on those surfaces: the initial surface characteristics are then regained by replenishing the adsorption and reaction site with oxidizing agents, where O_2 represents the ideal agent. As proposed in the Mars-van Krevelen oxidation mechanism supported by these systems, the lattice oxygen species on the catalyst plays a central role in providing oxygen atoms that eventually appear within the products of the oxidation.[1]

As discussed previously (chapter 2), molybdenum in MoO_3 allows the surface to selectively catalyze via C–H activation alkanes to obtain partial oxidation products such as corresponding alcohols and aldehydes. In mixed oxides where another transition metal is present, molybdenum still gives a large contribution to the redox process converting alkanes into alkenes through dehydrogenation.[2]

The periodic density functional theory (pDFT) used to treat redox processes on oxides surfaces is affected by the self interaction error which tends to delocalize electronic states: DFT methods describe the electron interacting with itself because its potential is generated by an electronic density that includes the same electron; the results affected by this error are therefore biased and do not reproduce experimental electron spin resonance measurements[2] or post-Hartree-Fock calculations.[3] The self interaction effects[4] can be corrected either by using hybrid functionals[5] or by introducing

additional on-site terms to compensate for the error; although both these approaches allow a more accurate treatment of the spin localization in DFT, the latter is more adapt when employed in plane wave (basis sets) periodic calculations. The effect of the additional potential on the defective MoO_3 surface has been studied[6] and its value has been determined through reference calculations using the hybrid functional approach.

As already discussed in section 2.3, the fundamental unit of the orthorombic α-MoO_3 layered structure is represented by edge- and corner-sharing distorted MoO_6 octahedron pictured in figure 6.1.

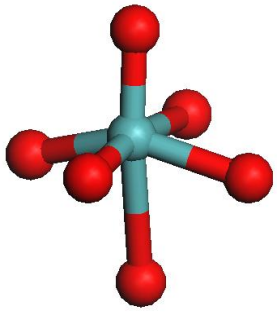

Figure 6.1. MoO_6 octahedron structure of the bulk α-MoO_3 (key: Mo atom is blue, O atoms are red).

The substrate adsorption on the three surfaces considered, namely $MoO_3(010)$, $Fe_2(MoO_4)_3(001)$ and $(\bar{1}10)$, is studied in order to identify the most likely energetic paths and mechanism of an alkane reaction leading to corresponding olefins.

Figure 6.2 shows a proposed scheme of the propane oxidation mechanism mediated by $MoO_3(010)$ surface: the perfect surface is reduced to create the conditions for the substrate, activated by an initial H transfer onto the lattice, to adsorb and react via a second H transfer, followed by the product desorption and the recovery of the surface initial conditions. The oxidizing agent, the oxygen atom itself, is provided by the lattice of the catalyst (Mars-van Krevelen mechanism): a more detailed description of the mechanism and its *redox* cycle will follow. The study was only able to provide calculated structures and energies for the first two intermediates following the defect creation with the (perfect) surface O atom removal.

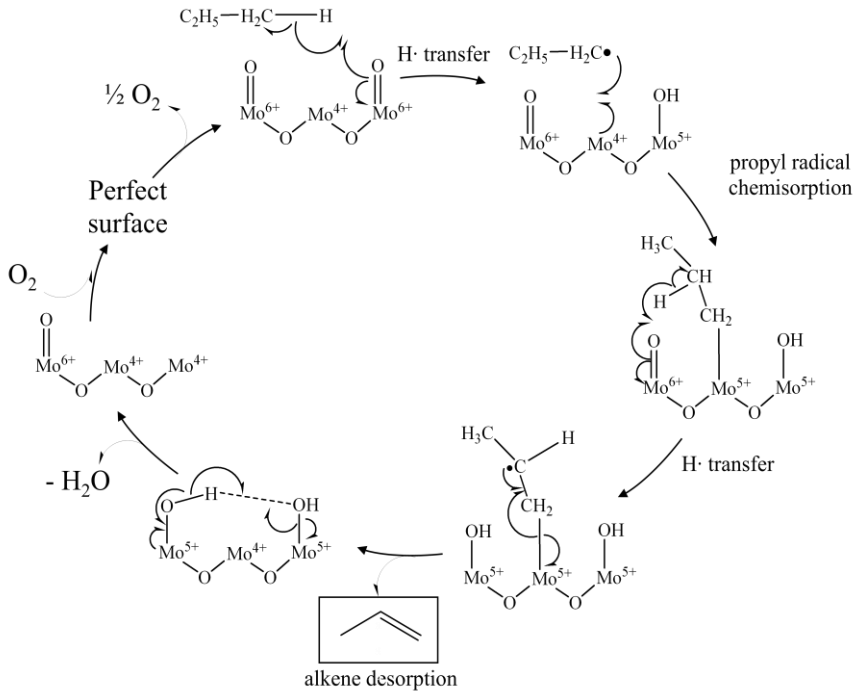

Figure 6.2. The mechanism of the propane oxidation mediated by MoO_3(010), as proposed in this work.

The choice of employing propane as a model for studying the oxidation of alkanes is based on the compromise between being a substrate computationally not expensive, due to its small size, and the fact that propane can be oxidized in two chemically diverse positions, the comparison of which is able to provide insights of reactivity that can be directly transferred to larger and more complex substrates.

The homolysis of a terminal propane C–H bond leads to a propyl radical, while an isopropyl radical is obtained when the bond to be cleaved is a secondary one: therefore, in this work the terms terminal- and secondary-mode adsorption refer to the adsorption of propyl and isopropyl radical, respectively.

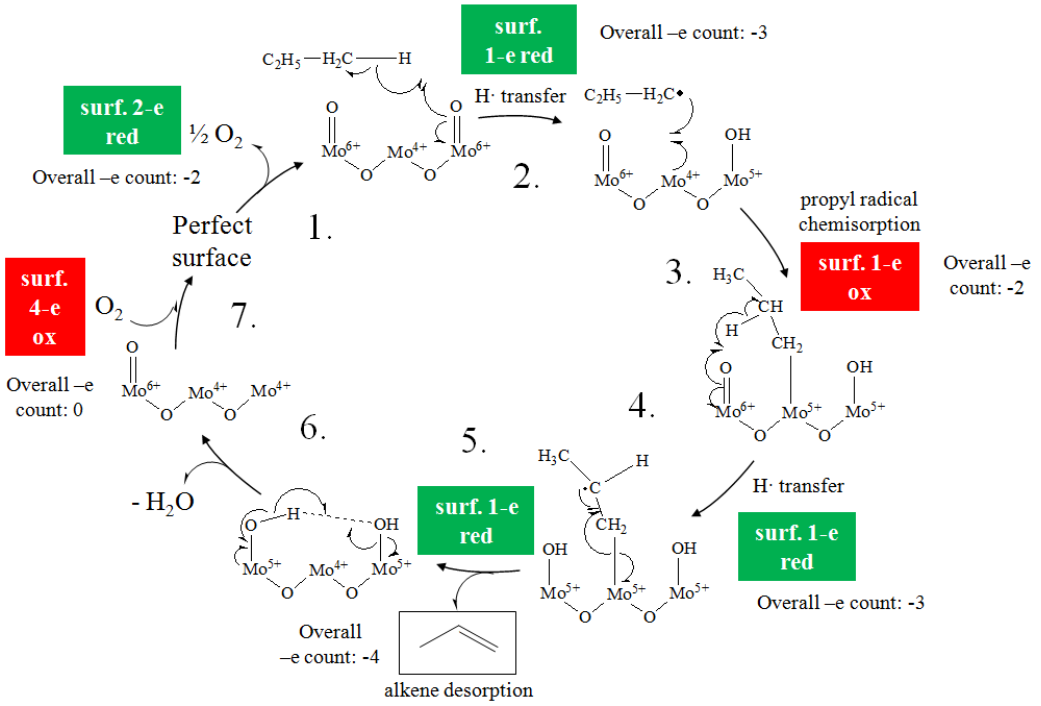

Figure 6.3. Proposed redox mechanism mediated by $MoO_3(010)$ for the propane oxidation reaction: $½O_2(g) + (g)C_3H_8 \rightarrow H_2O(g) + (g)C_3H_6$.

Figure 6.3 shows a more detailed reaction scheme: as a result of the O_T removal, two electrons are left on the surface and the scheme attempts to follow their location along the reaction, in order to identify all the aspects of the *redox* cycle studied.

As a catalyst and oxidizing agent, molybdenum in oxides is believed to perform most effectively if operating under slight reduced conditions.[7,8]

As already proposed,[9] the active oxygen species in partial oxidation reactions is the terminal oxygen (O_T), as also confirmed by studies on methane partial oxidation to formaldehyde.[6] So, step 1 of the cycle in figure 6.3 is characterized by the loss of a single O_T atom bound to a surface Mo(VI) atom, which is an expected event on MoO_3 surfaces.[10,11] the remaining two electrons sit on the metal centre which is therefore reduced to Mo(IV).

When surface defects are exposed to gaseous O_2, a re-oxidation may take place. On the contrary, extended defects may also occur,[12] in which case a crystallographic shear occurs: this process is characterized by changes in metal-to-oxygen stoichiometry and by metal-oxygen unit rearrangements.

The propane C–H bond activation is step 2 of the cycle: this step represents the main focus of this part of the study and that, together with the corresponding step on the iron molybdate surfaces, took up the largest part of time dedicated to the surface calculations. For this step, VASP (section 6.2) was employed and the Nudged Elastic Band (NEB)[13,14,15] (section 4.5) is the method used to locate and identify the transition state of this first surface-mediated H atom transfer.
The radical chemisorption on the active site, which oxidizes the surface, is step 3 and is the furthest step the calculations were able to describe, as already anticipated. A second hydrogen radical transfer (further surface reduction) to a vicinal lattice oxygen is what was proposed to follow the radical chemisorption (step 4), and in sequence the product (propene) desorption (step 5), the loss of water as a by-product (step 6) and the subsequent surface oxidation with two O atoms (step 7) to close the redox cycle allowing the surface to obtain the initial characteristic.

This chapter presents results obtained from the VASP[18,19] and Gaussian09[16] codes representing two different approaches to correct the self interaction term within DFT: for VASP, this was done by using the Perdew, Burke and Ernzerhof's (PBE)[17] functional together with the DFT+U correction and in Gaussian09 the hybrid functional B3LYP was employed, as discussed in the next section.
The MoO_3 bulk phase and (010) perfect and defective surfaces are studied and focus is then given to clusters of different dimensions cut from the MoO_3(010) surfaces. Finally, the $Fe_2(MoO_4)_3$ system and its (001) and $(\bar{1}10)$ surfaces are considered.

6.2 Computational Details

The periodic calculations performed in this work have all been carried out employing the Vienna *ab initio* Simulation Program (VASP).[18,19]

The calculations were carried out within the generalized-gradient approximation (GGA) and the PBE functional[17] was also used for its accurate description of the uniform electron gas, the correct behaviour under uniform scaling and a smoother potential, which all represent improvements compared to the PW91[20] functional.

The Project Augmented Wave method (PAW)[21,22] was used as pseudopotential for the good agreement with the all electron results and also for the less parameters required to construct potentials, compared to the ultra-soft potential methods.[23] Within this work, the pseudopotential includes molybdenum and iron (in the mixed oxide system) orbitals up to 4*s* (included) and the 1*s* orbital for carbon and oxygen, while the molybdenum and iron 4*p* orbitals (valence), 4*d* and 5*s*, the 4*p* orbitals for carbon and oxygen and the 1*s* for hydrogen atoms are all treated explicitly. The pseudopotential radii of each atom were taken by the VASP pseudopotential database, in particular they were: 2.6 a.u. (*s* states) and 2.75 a.u. (*p* and *d* states) for Mo, 2.3 a.u. (*s* states) and 2.3 a.u. (*p* and *d* states) for Fe, 1.2 a.u. (*s* states) and 1.52 a.u. (*p* states) for O, 1.2 a.u. (*s* states) and 1.5 a.u. (*p* states) for C and 1.1 a.u. (*s* states) for H.

A mesh of (3×3×3) was employed upon bulk energy convergence within 0.01 eV after several tests on Monkhorst-Pack *k*-point grid densities, although for density of states calculations finer *k*-point grids are used.

The bulk energy was found to converge for a value of E_{cut} equal to 400 eV: this value has been used for all molybdenum oxide and iron molybdenum oxide calculations throughout this work.

The bulk unit cell size/shape and coordinate optimization are carried out by using the conjugate gradients technique that uses stress on the unit cell, total energy and Hellman-Feynman forces on the atoms.

The *k*-points form no regular three-dimensional grid, so the band structure calculation is carried out by firstly generating a high quality charge density with the defined *k*-point grid through a self consistent run; finally, the density charge is then used in a non-self-consistent run with denser grid.

VASP is also able to calculate the vibrational frequencies (section 3.4) employing the atomic masses and the Hessian matrix: the program can determine the matrix by calculating the second derivative of the energy with respect to the atomic positions. The construction of the Hessian is carried out via a central difference: two displacements are specified, *i.e.* each ion makes a small positive and negative move (set to 0.04 Å). The VASP output file provides with the frequencies cm^{-1} which are compared to experimental values.[24]

The surface calculations are carried out on the (010) surface, for the MoO_3 system, and on the (001) and $(\bar{1}10)$ surfaces for the mixed system, namely $Fe_2(MoO_4)_3$. The MoO_3(010) surface is a bilayer (each layer is composed of 2 slabs) and a 14 Å vacuum gap separates it from its perpendicular periodic image. The two layers weakly interact in the *c*-direction, as evidenced by the difficulty for DFT to find a minimum in that direction. Therefore, the option of considering just a single bilayer instead of two was thought to be viable to simplify the model and save in computational time: initially, the surface unit cell for MoO_3(010) was set to p(3×3) to ensure enough molybdyl groups were present on the surface, in order not to exclude *a priori* the realistic possibility of clashes between these groups and the propyl radical during its adsorption on the surface. The number of *k*-points chosen for this system was (3×3×1) with an accuracy up to 10^{-3} (where the *c* direction being the vacuum direction), while the difference in energy between (3×3×3) and (5×5×5) was only accurate to 10^{-1}.

Despite not being formed by two layers like MoO_3(010), the two $Fe_2(MoO_4)_3$ surfaces (001) and $(\bar{1}10)$ have a higher structural complexity due to the presence of Fe(III). Iron is bonded to six oxygen atoms in an octahedral symmetry, while molybdenum is tetrahedral. Also for this mixed metal oxide a p(3×3) unit cell and a (3×3×3) *k*-points mesh were chosen.

DFT+U is the method used for the periodic calculations within this work (section 3.2.2): through the Dudarev *et al.*[25] approach, a value of 6.3[6] was selected for the molybdenum centres only.

Cluster models of the MoO_3(010) system were studied in this work in order to probe the electron localization described by the Hartree-Fock exchange, and were treated with hybrid DFT: since this is not available on VASP, the Gaussian09[16] program was

used. The basis sets used for molybdenum is the Los Alamos effective core potential plus double-ζ (LANL2DZ),[26,27] while for the oxygen, hydrogen and carbon centres is the split valence 6-31G(d) basis set, with polarization on the oxygen.

Lastly, in VASP the NEB method is employed to locate the transition state for the alkane C–H bond activation over the surface, as discussed in section 4.5.

6.3 MoO_3 (010) surface

6.3.1 Bulk, perfect surface and clusters

DFT is unable to properly describe dispersion interactions and as a consequence Coulombic and van der Waals forces are poorly represented. For this reason, the interlayer distance, which goes along the *c* direction in MoO_3 (figure 2.18), was not minimized. Instead the experimental value for the corresponding *c*-parameter was used for bulk calculations, while the rest of the parameters were optimized via relaxations of atomic coordinates at fixed volumes that varied around experimental values: in order to reduce the Pulay stress, final equilibrium values were obtained by a fit to an equation of state and then compared with the literature, as shown in table 6.1.

Table 6.1. Optimization of bulk MoO_3 lattice parameters.

Lattice parameter optimization	**Lattice constant (Å)**			
	This study	calc.[6]	LDA[28]	Exp[29]
a	3.972	4.022	3.729	3.963
b	3.715	3.752	3.478	3.696
c	*13.3855*[29]	*13.3855*[29]	13.036	13.3855

Experimental values in *italic*, unless stated.

Table 6.2. Mo–O bond lengths in MoO_3 bulk and (010) surface.

	Bond length (Å)				
Bond	Bulk	(010)	Bulk/(010)[6]	Bulk (exp)[29]	(010) LDA[28]
Mo–O_T	1.70	1.82	1.70/1.70	1.67	1.67
Mo–O_S	1.96	1.92	1.97/1.97	1.95	1.92
	1.96	2.32	2.34/2.41	2.33	2.30
Mo–O_A	1.77	1.88	1.75/1.76	1.73	1.76
	2.22	2.08	2.29/2.28	2.25	2.19

The calculated Mo–O bond lengths for MoO_3 bulk and (010) surface are shown in table 6.2 and compared to values obtained from previous computational studies for this same system[6,28] and experimental values.[29]

Figure 6.4 shows the optimized structures for the clusters studied in this work: the construction of these clusters is discussed in section 4.6.

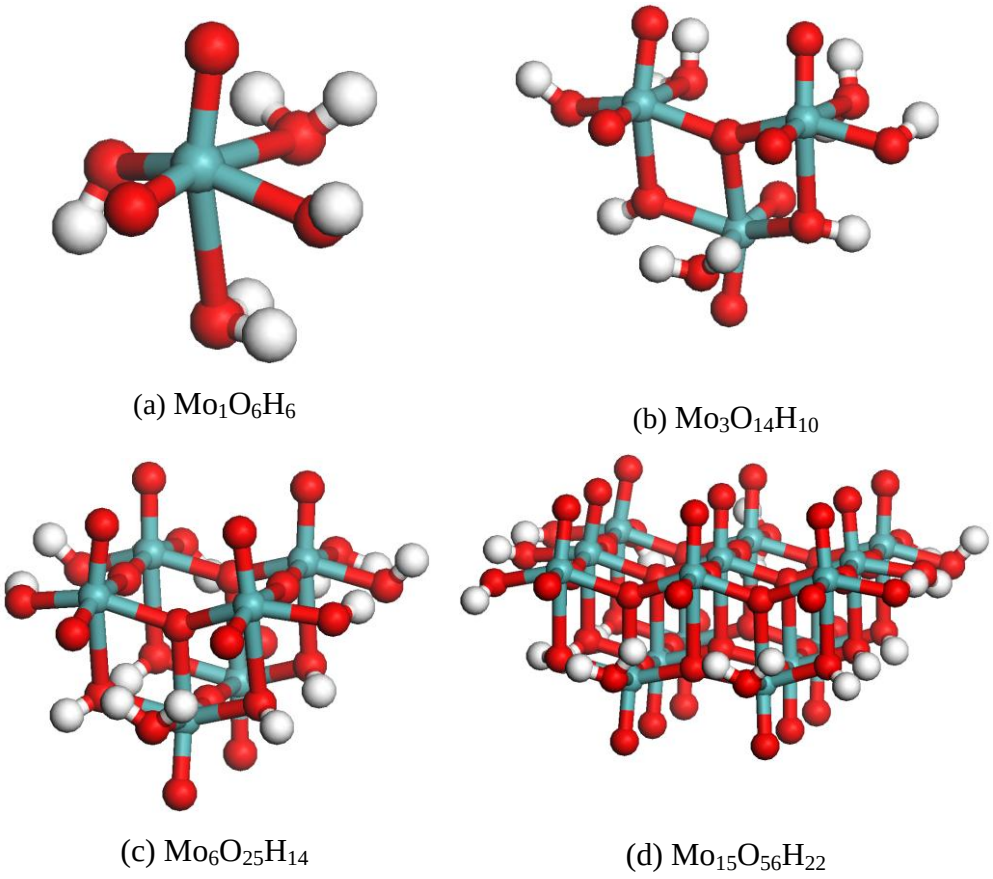

(a) $Mo_1O_6H_6$ (b) $Mo_3O_{14}H_{10}$

(c) $Mo_6O_{25}H_{14}$ (d) $Mo_{15}O_{56}H_{22}$

Figure 6.4. Clusters cut from MoO_3(010) surface of different size: (a) $Mo_1O_6H_6$, (b) $Mo_3O_{14}H_{10}$, (c) $Mo_6O_{25}H_{14}$ and (d) $Mo_{15}O_{56}H_{22}$. The clusters include H atoms added at their edges to correctly terminate according to the valency of the O atoms: the number of H atoms depends of the bond length between the relevant edge O atom and the Mo atom neglected from the surface (key: Mo atoms are blue, O atoms are red, H atoms are white).

The clusters' optimized structures clearly maintain their periodic features even with the saturation H atoms applied to the edges to mimic the neglected surface around each cluster.

Measured Mo–O bonds in each cluster (table 6.3) are very close to those measured for the MoO_6 unit in MoO_3(010) (table 6.2).

Table 6.3. Mo–O bond lengths in MoO_3 clusters generated from the perfect and optimized (010) surface.

	Bond length (Å)				
	$Mo_1O_6H_6$	**$Mo_3O_{14}H_{10}$** [a)]	**$Mo_6O_{25}H_{14}$** [a)]	**$Mo_{15}O_{56}H_{22}$** [a)]	**$Mo_{15}O_{56}H_{22}$** [30]
Mo–O_T	1.712	1.704-1.713	1.693-1.700	1.691-1.701	1.67
		1.709	1.697	1.695	
Mo–O_A	1.711	1.706-1.717	1.728-1.762	1.710-1.752	1.73
		1.711	1.742	1.737	
	2.530	2.249-2.353	2.318-2.335	2.214-2.367	2.25
		2.289	2.311	2.278	
Mo–O_S	1.935	1.936-1.991	1.931-1.975	1.934-2.062	1.94
		1.966	1.950	1.970	
	1.973	2.001-2.025	1.963-2.025	1.921-2.029	1.94
		2.012	1.987	1.967	
Mo–$O_{interlayer}$	2.529	2.460-2.584	2.250-2.505	2.333-2.572	2.33
		2.525	2.436	2.442	

[a)] Mo–O_X bond length ranges (above) and corresponding average (below).

Table 6.3 compares the Mo–O bond lengths of the clusters of different sizes cut from MoO_3(010) surface (ranges and corresponding averages) and those of the $Mo_{15}O_{56}H_{22}$ cluster studied by Witko *et al.*[30] The choice of reporting here ranges and averages was dictated by the different environments within each cluster, except for $Mo_1O_6H_6$ obviously: this is due to the different number of molybdenum atoms in each structure. All Mo–O bond length values except one, namely Mo–O_T, reported by Witko fall within the ranges of the corresponding cluster generated in this study, namely $Mo_{15}O_{56}H_{22}$, which seems to be consistent with the fact that statistically the averages for that cluster are bound to be more accurate than the other clusters because calculated over fifteen sets of Mo–O bond lengths, while the second largest cluster, namely $Mo_6O_{25}H_{14}$, has less than half number of sets, *i.e.* six.

The large computational effort made in this study, in terms of CPU time and resources employed to carry out calculations with molybdenum oxide surfaces, made it

important to consider ways to simplify the periodic models in order to speed up the computations.

MoO_3(010) surface was initially obtained by cleaving its bulk phase to a 2-layered surface, where each layer was formed by two slabs (figure 2.19). The elimination of the two bottom slabs was explored as a way to simplify the system (figure 6.5).

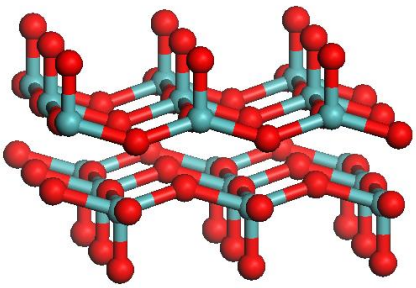

Figure 6.5. Simplified MoO_3(010) surface model with one layer (2 slabs): one layer was removed from the original catalyst with two layers (4 slabs, figure 2.19) to increase in overall computations speed and save in CPU time (key: Mo atoms are blue, O atoms are red).

These changes had to be proven capable of, most importantly, providing consistent results to those found for the 2-layered system, and at the same time they had to bring substantial improvements not only in terms of CPU running time decrease (from computation start to convergence), but also for the time required to carry out the whole calculation: the queuing time (from submission to computation start) adds up to the overall calculation time and having the system a "lighter" structure, *i.e.* 1-layer (2 slabs), was thought to theoretically have a positive impact on decreasing the resources requested to run the calculation.

6.3.2 Defective surface and clusters

In order to calculate the energy for the formation of a vacancy on the MoO_3(010) surface one can either calculate the energy of the O_2 molecule as a reference for the O atom that is removed or simply that of the oxygen atom, making sure that in both cases the ground state is a triplet. In this study, the calculated O_2 energy is E_{O2} = -9.85 eV

(bond length 1.24 Å) which resulted in E_O = -4.93 eV per O atom. For sake of consistency with previous calculations, the reference state chosen in this work is the neutral oxygen atom. When an oxygen atom is removed from the reducible MoO_3(010) surface, the remaining two electrons sit on the molybdenum centre. The defect energy is the energy to create the defect through the removal of ½ O_2*(g)*.

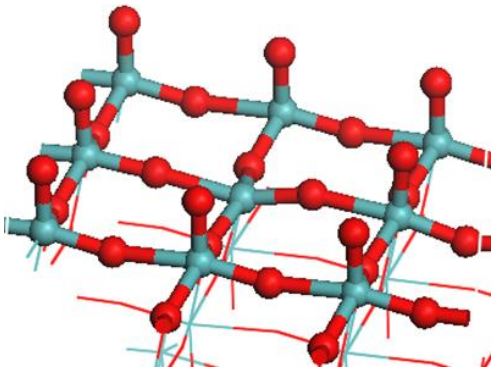

Figure 6.6. Structure of the defective MoO_3(010) surface from the periodic model with 4 layers optimized with VASP: the defect is created by the removal of a terminal oxygen atom (key: Mo atoms are blue, O atoms are red).

Breaking the Mo–O bond on the α-MoO_3 (010) surface by removing an O_T atom reduces the molybdenum atom from Mo(VI) to Mo(IV). By comparing the DOS results for perfect and defective surfaces (figure 6.7, left), it was possible to identify an extra occupied band gap state corresponding to the molybdenum *d* electrons sitting on the metal centre of the defective surface.

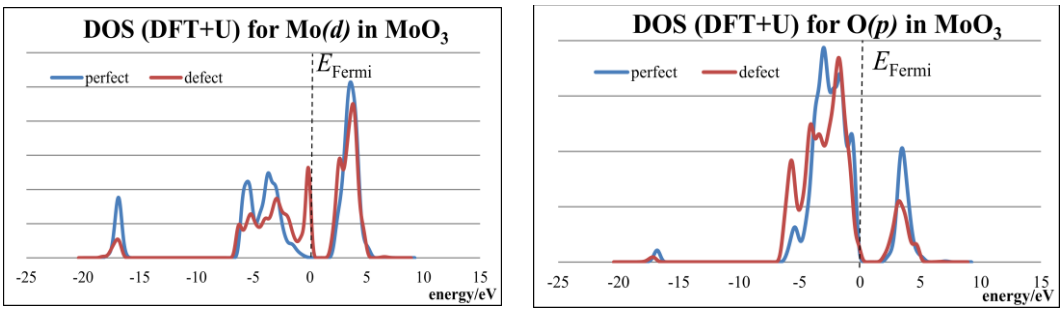

Figure 6.7. DOS analysis of perfect and defective α-MoO_3 (010) surface: (*left*) reduction Mo(VI) to Mo(IV) at the defect of the surface corresponding to an additional occupied band gap state in the Mo*(d)* bands. This is isolated to the metal centre as (*right*) no corresponding state is observed for the O*(p)* bands.

For the DOS analysis for the *p* orbital bands of the oxygen atoms surrounding the metal centre (figure 6.7, right), no corresponding state could be observed and this confirmed that the extra electrons sit exclusively on the metal centre, as expected on a reducible oxide like MoO_3.

For the cluster models, the vacancy was created on the optimized perfect cluster by removing an O_T atom and carrying out a further optimization leaving, as described before for the perfect cluster, the H atoms frozen and the rest of the cluster atoms free to relax.

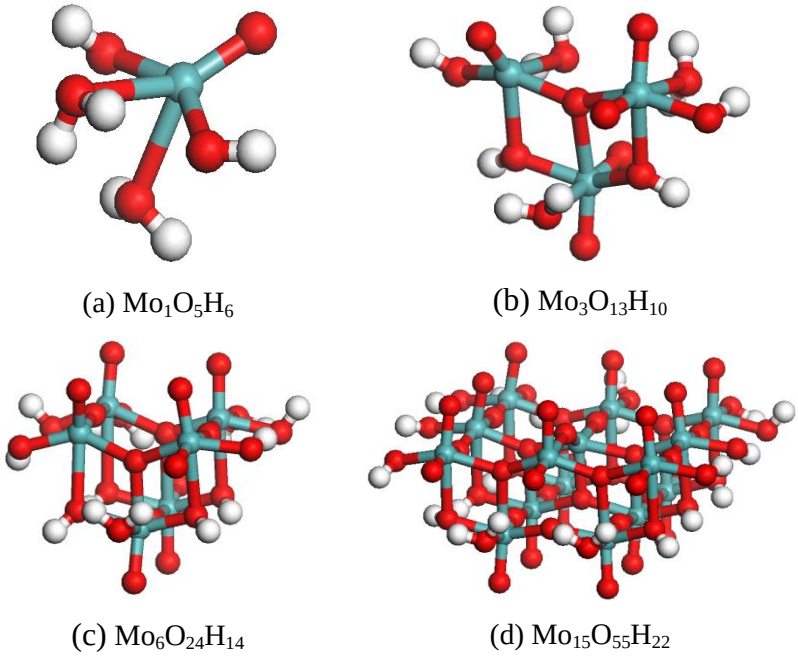

(a) $Mo_1O_5H_6$ (b) $Mo_3O_{13}H_{10}$

(c) $Mo_6O_{24}H_{14}$ (d) $Mo_{15}O_{55}H_{22}$

Figure 6.8. Structures of the defective clusters cut from a perfect MoO_3(010) surface (the names reflect the actual composition of the cluster): (a) $Mo_1O_5H_6$, (b) $Mo_3O_{13}H_{10}$, (c) $Mo_6O_{24}H_{14}$ and (d) $Mo_{15}O_{55}H_{22}$. The defective clusters are created by the removal of a terminal oxygen atom from the corresponding perfect clusters (key: Mo atoms are blue, O atoms are red, H atoms are white).

As can be seen from figure 6.8, the O_T removal causes the O_A with shorter O–Mo bond (with no saturation H atom in the smaller clusters) to raise and this effect is observed in all clusters: the O_A–Mo bond shortens in all systems indicating that the remaining O_A replaces the removed atom and this effect may be caused by the neglected surface

which is an element of destabilization. The O_A rise though does not clash with the alkane approaching the Mo(IV) centre and therefore it has no repercussion on either the H transfer (figure 6.3, step 2), or on the radical adsorption (figure 6.3, step 3).

A spin state study for all clusters used in this work was carried out and confirmed what was also reported in a past computational study[6] involving a $Mo_7O_{32}H_{22}$ cluster, which is that the metal atom is in a triplet state at the defect.

Table 6.4. Defect energy (eV) relative to an oxygen atom removed from the relevant systems studied.

	Defect Energy (eV)		
Model / O_T removed	**DFT+U**		**DFT (B3LYP)**[a)]
	4 slabs	*2 slabs*	
MoO_3(010) (surface)	0.87	1.35	-
	1.36[b)]	1.47[b)]	-
$Mo_1O_6H_6$ (cluster)	-	-	3.32
$Mo_3O_{14}H_{10}$ (cluster)	-	-	3.09
$Mo_6O_{25}H_{14}$ (cluster)	-	-	2.19
$Mo_{15}O_{56}H_{22}$ (cluster)	-	-	2.62

[a)] Spin state of defective cluster surface is triplet. [b)] Dispersion correction[31] introduced.

Table 6.4 shows the calculated values for the energy necessary to remove the O_T atom from MoO_3(010) surface and clusters.

The comparison of these values across the different systems, *i.e.* surface and clusters, does not give a pattern of consistency and this is due to the very different set ups. The different structural features seem to play an important role: the use of saturating H atoms in clusters to mimic the periodic structure prevents the clusters from collapsing during the optimization but it does not provide the stabilization that the neglected surface does in the periodic systems; an effect of this was described earlier for the O_A atom raising and Mo–O_A shortening following the O_T removal. Furthermore, the cluster calculations are carried out employing hybrid functionals, *i.e.* B3LYP, because the DFT+U correction is not available in the Gaussian09 package: hybrid functionals offer an alternative way to deal with the self interaction correction. Also, the

dispersion correction[31] has a significant effect on the size of the defect energy calculated and on the consistency of the two slab thicknesses.
Within the clusters, consistency across the size of the model is observed: the defect energy seems converging to lower figures with size increase, probably caused by a stabilizing effect exerted by the presence of more atoms. These energies though show discrepancies from cluster calculations made by Witko *et al.*[32] who found 6.80 eV for O_T: the reason may be due to the poor treatment of the Madelung potential when describing the cluster models.

6.3.3 Radical adsorption on defective surface and clusters

The simulation of the propane adsorption on the models studied was attempted by considering the energy difference between the structures' initial state, where the alkane is standing over the T site of the defective surface, and the final state where the alkane H atom is bound to the lattice oxygen and the radical is adsorbed at the metal centre.

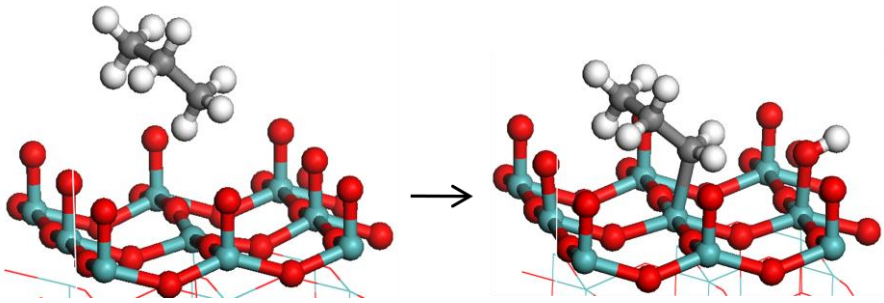

Figure 6.9. Terminal adsorption of the propyl radical on MoO_3(010) active site (key: Mo atoms are blue, O atoms are red, C atoms are grey, H atoms are white).

As discussed in the introduction of this chapter, two modes of adsorption are studied: a *terminal* mode where a terminal H atom from the alkane is transferred on to the surface, which leads to the formation of a propyl radical eventually adsorbing on the catalyst, and a *secondary* mode where a secondary H atom instead is transferred, which leads to an isopropyl radical adsorbing on the surface.

Figure 6.9 displays the terminal mode for the propyl radical adsorption on $MoO_3(010)$ surface. The catalyst modelled here includes 2 layers (4 slabs) while the corresponding simpler model with only 1 layer (2 slabs) showed instability issues: the top slab seemed to break its structural features displaying surface roughness not observed on the 2 layered model. This may be caused by the neglected stabilization interaction with the missing bottom layer.

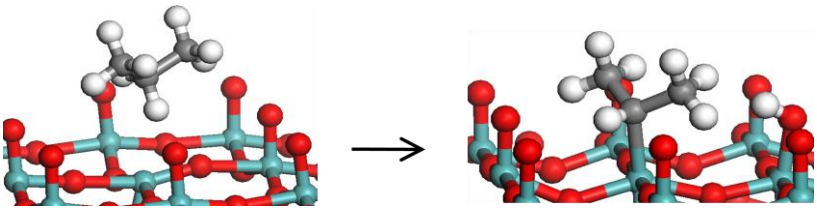

Figure 6.10. Secondary adsorption of the propyl radical on $MoO_3(010)$ active site (key: Mo atoms are blue, O atoms are red, C atoms are grey, H atoms are white).

Figure 6.10 shows the secondary mode of adsorption on 2 layers (4 slabs) of $MoO_3(010)$ surface.

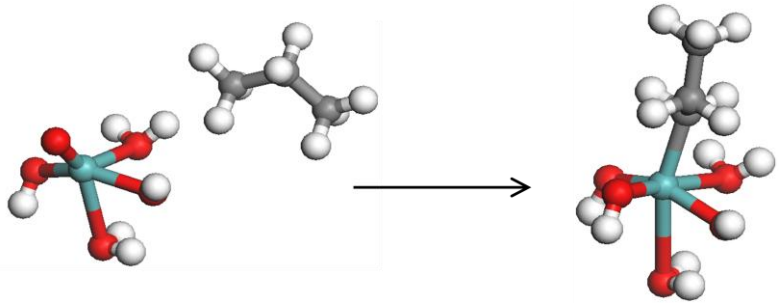

Figure 6.11. Simulation of the (primary) adsorption reaction of propyl radical on the defective cluster $Mo_1O_5H_6$ cut from $MoO_3(010)$ surface (key: Mo atoms are blue, O atoms are red, C atoms are grey, H atoms are white).

Figure 6.11 shows the terminal adsorption mode occurring on the smallest of the defective clusters considered, *i.e.* $Mo_1O_5H_6$. This model can only provide limited information regarding possible interactions with the neglected vicinal MoO_6 octahedra, but it becomes important within the comparison with larger size clusters to test the defective energy. It is possible to observe that in $Mo_1O_5H_6$ the raised O_A atom, due to the O_T removal that created the defect, does not prevent the radical from adsorbing. This may be because the H atom is transferred on O_A itself, which may induce the oxygen atom to position itself equatorially to avoid clashing with the

incoming radical; on larger clusters this does not happen because the H atom is assumed to transfer to another O_T atom.

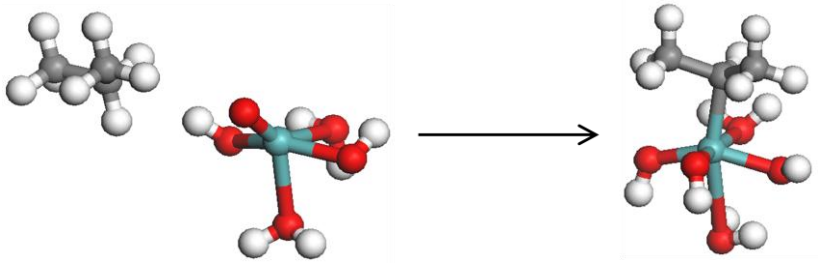

Figure 6.12. Simulation of the (secondary) adsorption reaction of isopropyl radical on the defective cluster $Mo_1O_5H_6$ cut from MoO_3(010) surface (key: Mo atoms are blue, O atoms are red, C atoms are grey, H atoms are white).

The secondary mode of adsorption on the defective cluster $Mo_1O_5H_6$ is shown in figure 6.12 while propyl and isopropyl radical adsorption reactions on $Mo_3O_{13}H_{10}$ are shown in figure 6.13 (a) and (b), respectively.

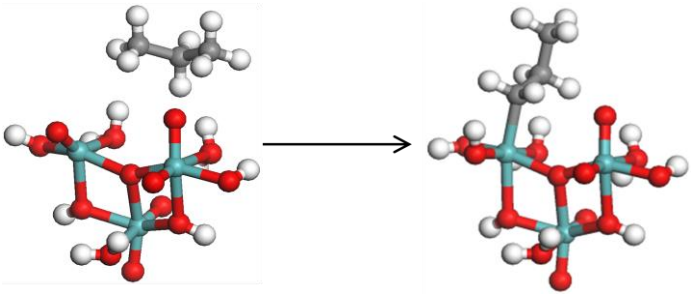

(a)

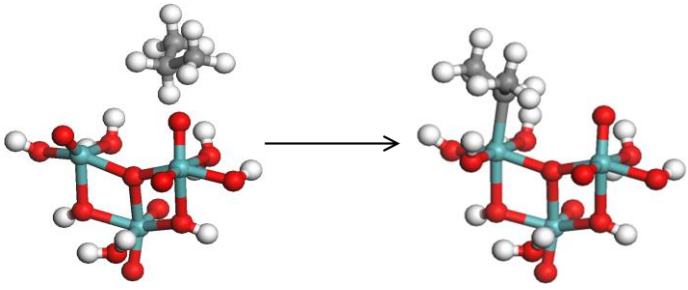

(b)

Figure 6.13. Simulation of (a) propyl radical (primary) adsorption reaction on the defective cluster $Mo_3O_{13}H_{10}$ and of (b) isopropyl radical (secondary) adsorption on the same defective cluster cut from MoO_3(010) surface (key: Mo atoms are blue, O atoms are red, C atoms are grey, H atoms are white).

In $Mo_3O_{13}H_{10}$ defective cluster too, O_A shows the tendency to assume a terminal position, which is a characteristic observed on the largest defective cluster of all too, namely $Mo_{15}O_{54}H_{22}$, shown in figure 6.14(a) and (b) for the adsorption reaction of propyl and isopropyl radicals, respectively.

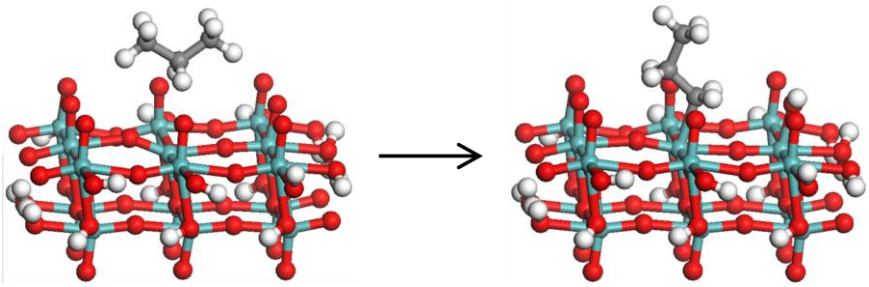

(a)

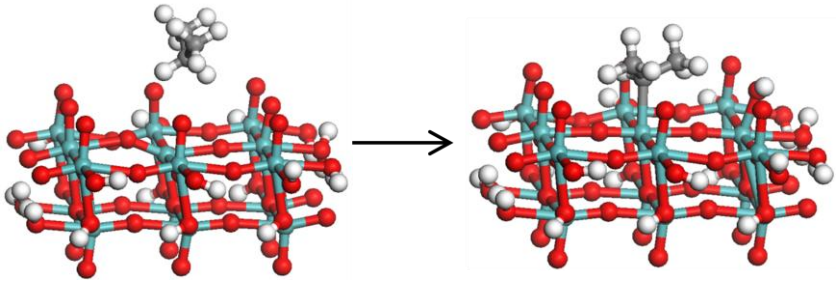

(b)

Figure 6.14. Simulation of (a) propyl radical (primary) adsorption and (b) isopropyl radical (secondary) adsorption reactions on the defective cluster $Mo_{15}O_{55}H_{22}$ cut from MoO_3(010) surface (key: Mo atoms are blue, O atoms are red, C atoms are grey, H atoms are white).

The $Mo_{15}O_{55}H_{22}$ defective cluster is the only model where the metal centre is located in the middle of the cluster far from the edges, in fact even in $Mo_6O_{24}H_{14}$ (figure 6.8(c)) the T site is at one of the corners of the cluster. In $Mo_{15}O_{55}H_{22}$, the two pairs of O_A and O_S atoms bonded to the molybdenum atom at the defect are bridged oxygen atoms, therefore potentially stable within the surface: despite this fact, the tendency of at least one O_A to assume a terminal orientation (once defect is created) is still present as shown on the left hand side of the two reactions in figure 6.14, although this does not lead to a surface Mo–O_A bond breaking.

Table 6.5. Reaction energies calculated for the MoO_3(010) surface systems studied in this work including the 2 and 4 layers surface models and the clusters $Mo_1O_6H_6$, $Mo_3O_{14}H_{10}$, $Mo_{15}O_{56}H_{22}$.

	Reaction Energy (eV)			
Model	**Terminal**		**Secondary**	
	surface			
MoO_3(010)	*4 slabs*	*2 slabs*	*4 slabs*	*2 slabs*
	0.08	-	0.08	0.07
	cluster			
$Mo_1O_6H_6$	0.48		0.02	
$Mo_3O_{14}H_{10}$	0.62		0.69	
$Mo_{15}O_{56}H_{22}$	0.27		0.52	

The results of the calculations showed that the adsorption on MoO_3 systems is slightly unfavourable as the reaction energy is positive (table 6.5). The cluster models confirm this trend, although they show larger figures with values of an order of magnitude higher than the corresponding surface values.

6.3.4 C–H bond activation

The supporting systems studied in this work were investigated with the Nudged Elastic Band (NEB) method described in chapter 4. Each individual calculation is started off with an initial guess for the overall adsorption process through a linear interpolation employing *Intervasp*,[33] an in-house utility program that features the GRUP method and the *late centre* option, very useful in situations where a molecule is required to reach a determined location prior to any chemical event occurring, represented in this case by the propane H atom transfer onto the lattice.

Although the study did not undertake any *Dimer Method* (section 4.5) check, transition states (TS) were identified and confirmed via multiple NEB runs. The energy curve of an NEB calculation was assessed by looking for a saddle point (maximum). When it was deemed to have found one, a frequency calculation was undertaken to confirm the existence of an imaginary value corresponding to a transition state structure. Then, the

preceding image of the TS structure and the one just following were selected and a second NEB calculation was run between the two to further confirm the finding.

Several NEB runs were being launched in order to lower the TS energy barrier and head to convergence. This was necessary to use the selected *ab initio* method VASP, a computationally expensive package, combined with the computational resources available at the time of the calculations that were provided by the Hector Supercomputer[34] in packages of 24 hours per run: being the 4 slab defective $MoO_3(010)$ system formed by 143 atoms, 36 of which were molybdenum atoms, it was necessary to restart the calculations several times to reach convergence. Plot in figure 6.15 shows NEB results for propyl radical (terminal adsorption) adsorbing on the 4 slab model of the α-$MoO_3(010)$ surface, which in total required 47 restarts to reach convergence.

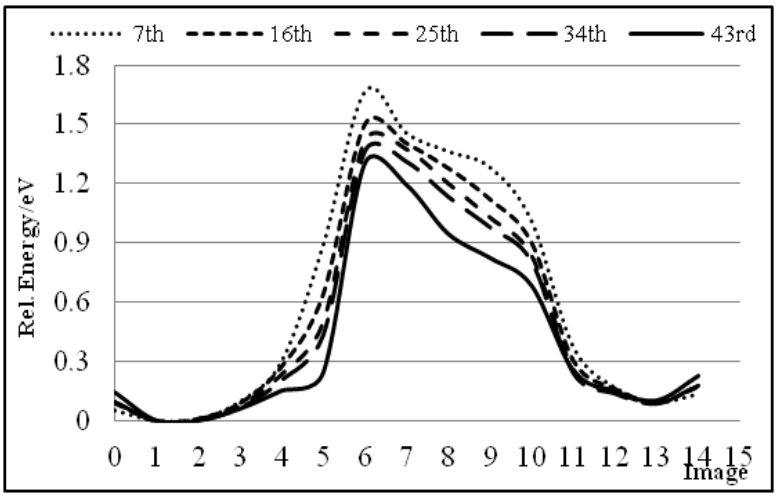

Figure 6.15. Plots of successive NEB calculations for propane terminal adsorption on α-MoO3(010) (4 slab) surface.

A snapshot of what it is thought to be the transition state for the "7th" run of figure 6.15, is shown in figure 6.16: the peak of energy barrier corresponds to the moment immediately following the alkane H atom transfer to the lattice O, which is when the propyl starts its journey towards the defect where adsorption eventually takes place, event characterized by a decrease in energy.

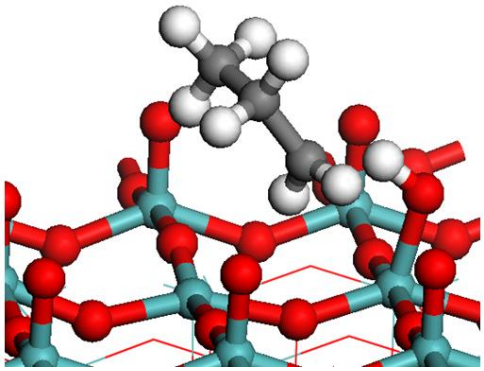

Figure 6.16. Snapshot of the transition state for the terminal C–H activation in propane adsorption on α-MoO_3(010) (4 slabs) surface (key: Mo atoms are blue, O atoms are red, C atoms are grey, H atoms are white).

Figure 6.17 shows the energy variation during the C–H cleavage for the same system shown in figure 6.15: this time the energy is plotted against the actual C–H bond distance.

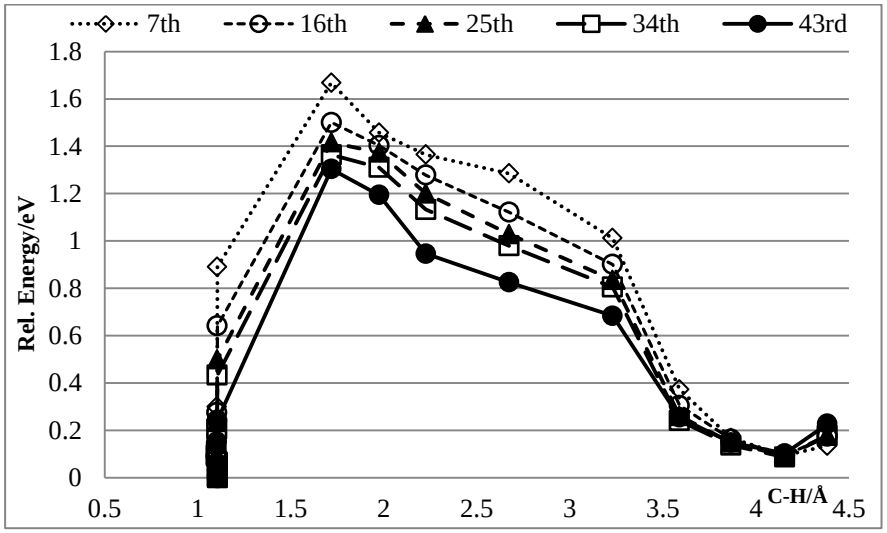

Figure 6.17. Plots of successive NEB calculations for propane terminal adsorption on α-MoO3 (010) (4 slabs) surface: energy as a function of the C–H bond distance.

A lack of markers between the first two marks from the left (*i.e.* at ~1.2 Å and ~1.75Å) is noticeable in figure 6.17. A deeper and more detailed NEB study was carried out to gather all possible information that might have been missed at the initial analysis and to uncover more sensible propane structural features when in proximity of

the curve peak, features that might have been hidden in the previous run; in particular, a further TS search between the structures corresponding to the two identified marks was run.

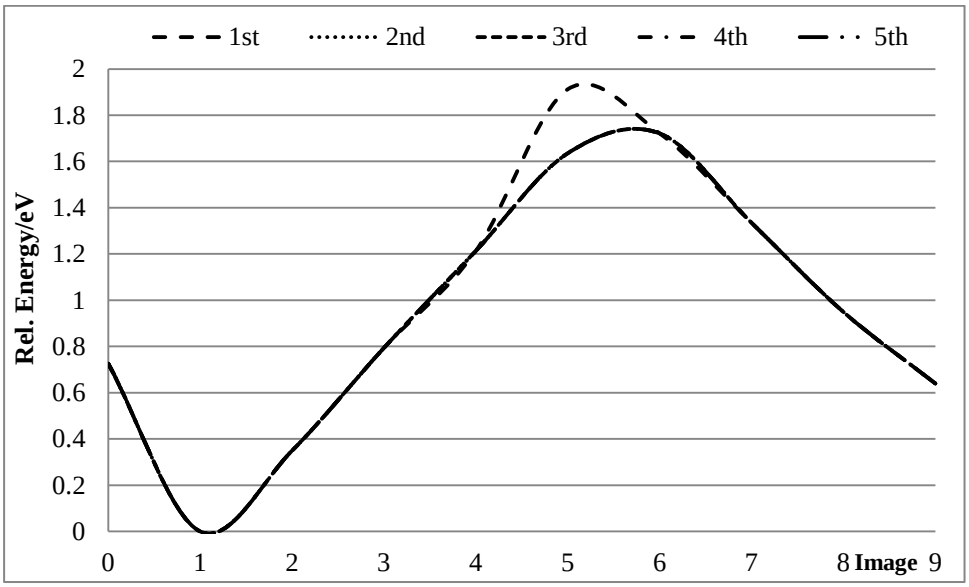

Figure 6.18. Plots of five successive NEB calculations for propane terminal adsorption on α-MoO3 (010) (4 slabs) surface, run between two structures identified on the plot of figure 6.17.

The plot of the more refined TS search in figure 6.18 shows an energy barrier decrease occurring only following the first run, which is an indication of optimization reached. A frequency calculation to verify whether image 6 in figure 6.18 corresponds to an actual TS structure was carried out: an imaginary frequency was found for the C–H bond breaking (1.61 Å), confirming that a potential energy maximum (saddle point) was identified for the terminal adsorption of propane onto MoO_3(010) surface.

Figure 6.19 shows four consecutive snapshots extracted from the NEB calculation where the propane primary C–H bond is broken, the propyl radical is formed and the H is transferred to the vicinal lattice O atom.

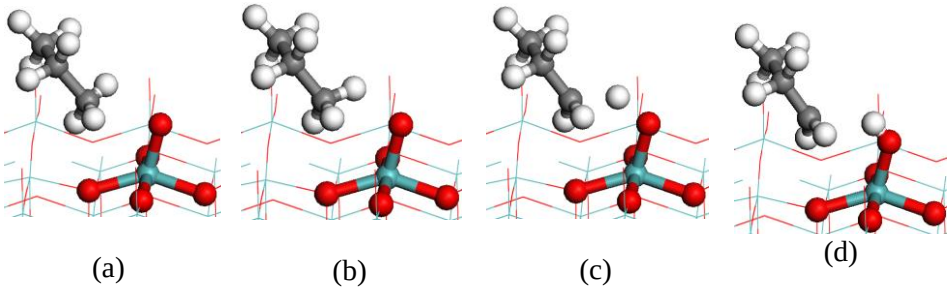

Figure 6.19. Terminal propane adsorption on MoO_3(010) (4 slabs) surface: sequence of snapshots ((a) to (d)) relative to the primary $C_{(propane)}$–H bond cleavage and H–$O_{(lattice)}$ bond formation (key: Mo atoms are blue, O atoms are red, C atoms are grey, H atoms are white).

Figure 6.20 plots two different sets of data: one is sourced by the NEB study for the propane terminal adsorption on MoO_3(010) (figure 6.15) and the more detailed NEB study (figure 6.17) triggered by the former study and aimed at exploring the region near to the transition state for C–H activation.

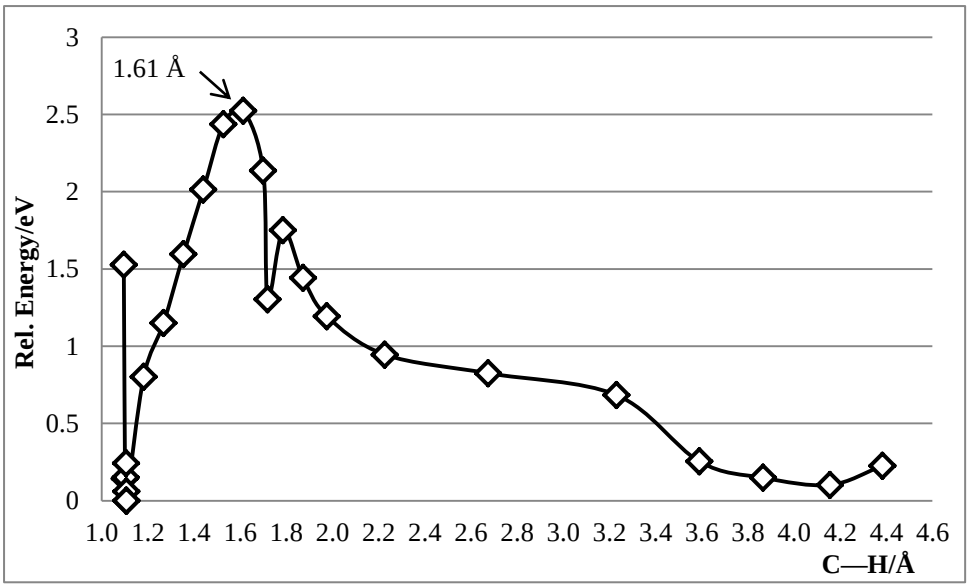

Figure 6.20. Propane terminal C–H activation on MoO_3(010) (4 slabs) surface: energy as a function of the C–H bond distance with highlighted the TS bond value. The plot unifies two sets of data, *i.e.* the "43rd" run from the initial NEB study (figure 6.15) and the "2nd" run from the more detailed NEB study (figure 6.17).

The simplification of the 4 slab model of the MoO_3(010) surface by removing the 2 bottom slabs, allowed to carry out relatively fast TS searches compared to the "full" system.

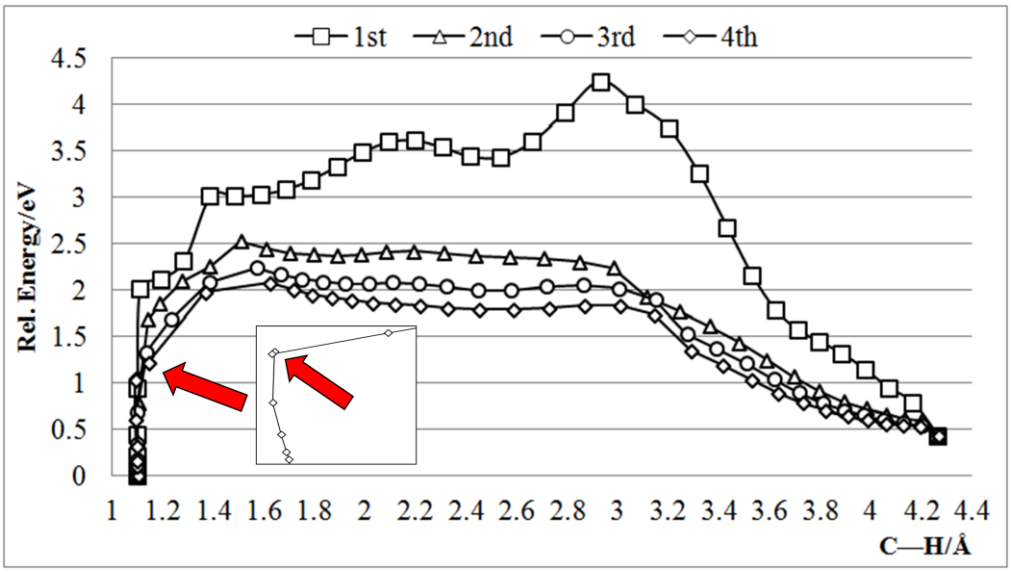

Figure 6.21. Plots of four successive NEB calculations for propane terminal adsorption on α-MoO3 (010) (2 slabs) surface: the energy varies as a function of the C–H bond distance. TS candidates of the "4th" run are shown (inset).

Figure 6.21 shows that the energy barrier height reached after four restarts (~ 2 eV) for the 2 slabs molybdate (010) surface is comparable to that of the same surface with 4 slabs (~1.45 eV, figure 6.15) after 7 restarts.

From the same plot it is also noticeable that the NEB calculations of the 2 slab system are effectively modelling the behaviour of radical species: the "plateau" (flat area) that forms following the activation barrier is typical in reactions involving radicals. As already described, the propyl radical is created by the abstraction of the propane terminal hydrogen: the radical then moves over the oxide surface with which it establishes a constant interaction (hence the "plateau") before approaching the metal centre Mo(IV) where eventually adsorption takes place.

The red arrow inside the inset of figure 6.21 highlights one of the TS candidates of the "4th" run.

6.4 $Fe_2(MoO_4)_3$ (001) and $(\bar{1}10)$ Surfaces

6.4.1 Bulk and perfect surface

As anticipated in chapter 2, the monoclinic phase of iron molybdate α-$Fe_2(MoO_4)_3$ is the second system studied: its structure is more complex than the molybdate system. In contrast to MoO_3, molybdenum appears in a tetrahedral rather than nearly octahedral environment (figure 2.24).

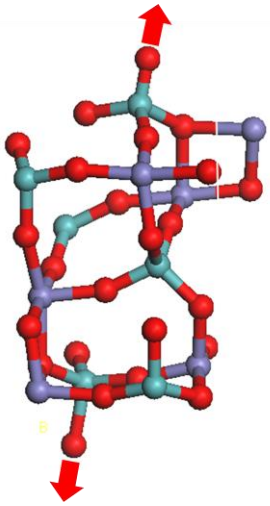

Figure 6.22. Visualization of the frequency calculation for the $Fe_2(MoO_4)_3$(001) slab: highlighted are the Mo=O stretching modes (key: Mo atoms are blue, O atoms are red, Fe atoms are purple).

To seek proof of the change in molybdenum symmetry from octahedral to tetrahedral when passing from molybdate to the mixed metal oxide, a frequency calculation for the Mo=O stretching modes was performed on $Fe_2(MoO_4)_3$(001) surface: figure 6.22 highlights the relevant Mo=O groups the calculation focused on. The comparison between the calculated frequencies and a measured Raman spectrum[35] of the $Fe_2(MoO_4)_3/MoO_3$ mixture produced the proof sought: figure 6.23 shows that the calculated frequencies (blue dots) for the tetrahedral M=O are matched by the measured tetrahedral M=O signature on the spectrum.

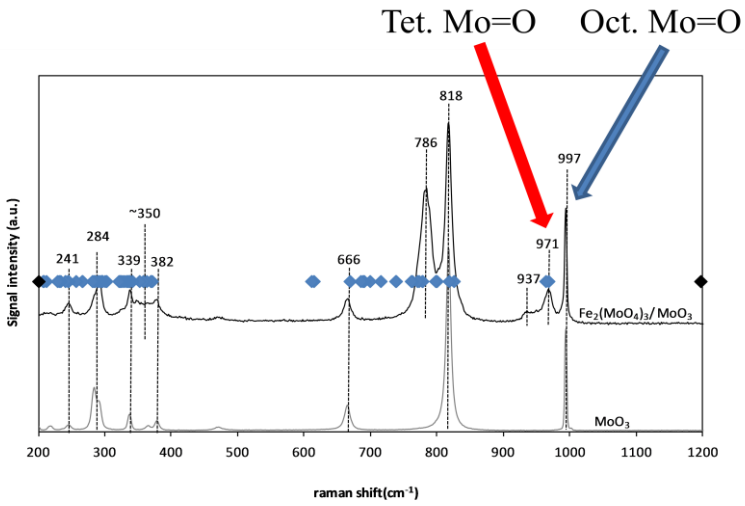

Figure 6.23. $Fe_2(MoO_4)_3(001)$ surface frequency values calculated with VASP[18,19] (blue dots) and compared with $Fe_2(MoO_4)_3/MoO_3$ measured Raman spectrum[35] showing that molybdenum in $Fe_2(MoO_4)_3$ is tetrahedral.

The complexity of the systems is evidenced by the many sets of Mo–O and Fe–O bond lengths measured describing at least five different environments within the system: the presence of a further metal atom generates a readjustment of the structure that follows a very different symmetric pattern compared to $MoO_3(010)$ surface.

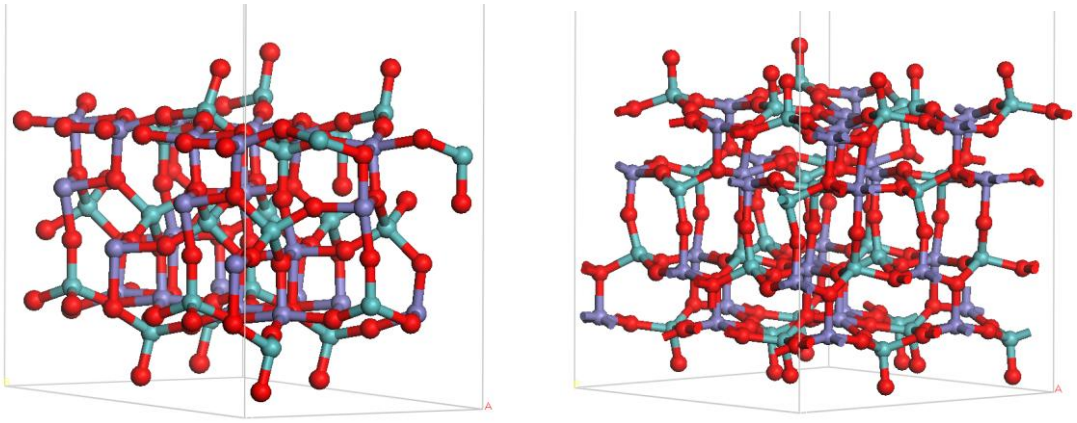

(a) (b)

Figure 6.24. Iron molybdate surfaces structure: (a) (001) surface; (b) $(\bar{1}10)$ surface (key: Mo atoms are blue, O atoms are red, Fe atoms are purple).

For the same reasons that a simpler model was sought for the MoO_3 system, here too an alternative to the initial p(3×3) cell for both $Fe_2(MoO_4)_3(001)$ and $(\bar{1}10)$ surfaces (figure 6.24(a) and (b), respectively) was identified by halving the *a* and *b* dimensions of the cell (figure 6.25(a) and (b), respectively) leaving the *c* direction (vacuum direction) untouched.

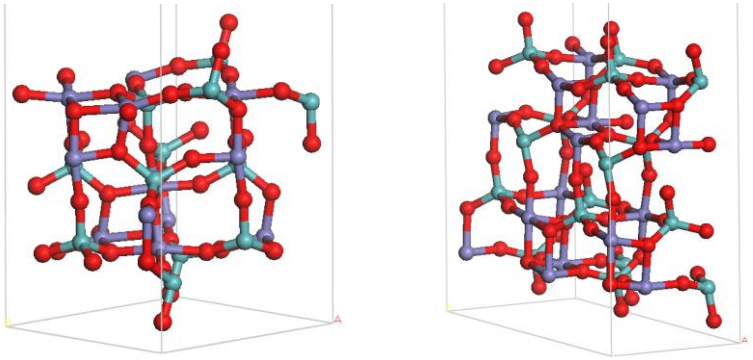

(a) (b)

Figure 6.25. "Half cell" model. Simplified iron molybdate surface structures: *a* and *b* directions halved for (a) (001) surface and (b) $(\bar{1}10)$ surface, while *c* direction (vacuum direction) is untouched (key: Mo atoms are blue, O atoms are red, Fe atoms are purple).

6.4.2 Defective surface

In α-$Fe_2(MoO_4)_3$ molybdenum is fully oxidised and the creation of a defect causes its symmetry to go from tetrahedral (figure 6.26(a) and (c)) to distorted trigonal planar (figure 6.26(b) and (d)).

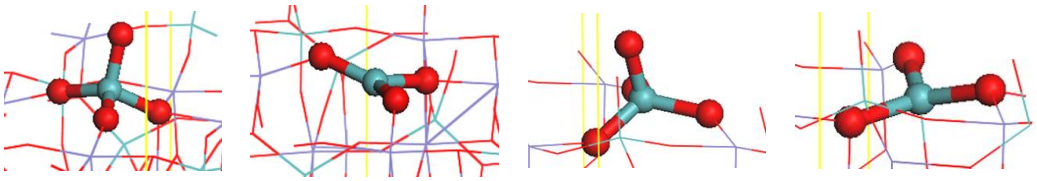

(a) (b) (c) (d)

Figure 6.26. Molybdenum symmetry in α-$Fe_2(MoO_4)_3$ surfaces: (a) MoO_4 unit of the perfect (001) surface and (b) MoO_3 unit of the defective (001) surface; (c) MoO_4 unit of the perfect $(\bar{1}10)$ surface and (d) MoO_3 unit of the defective $(\bar{1}10)$ surface. Clearly, the removal of one O atom causes molybdenum to go from tetrahedral to distorted trigonal planar (key: Mo atoms are blue, O atoms are red, Fe atoms are purple).

Table 6.6. Point defect energy formation for the removal of an O atom from iron molybdate (001) and $(\bar{1}10)$ surfaces (full cell model).

Model System/O Terminal (O_T) species removed	**DFT+U (eV)**
$Fe_2(MoO_4)_3(001)$	1.91
$Fe_2(MoO_4)_3(\bar{1}10)$	1.30

Table 6.6 collects the calculated energy for creating a point defect on the full cell model of the $Fe_2(MoO_4)_3$ surfaces. A small difference is noticeable between (001) and $(\bar{1}10)$ surfaces: neither of them is very available to be reduced (positive energy) and the former is less available than the latter.

6.4.3 Radical adsorption on defective surface

As previously discussed for the reaction on MoO_3, the propane adsorption energy is the result of the difference between the optimized initial state structure (alkane over defective surface) and optimized final state structure (alkane H atom bound to lattice oxygen and radical adsorbed at metal centre). The two modes of the radical adsorption are here too studied, namely *terminal* and *secondary*. The new element to be considered in this mixed metal oxide system is the possible competition between the two metal centres (T sites), *i.e.* molybdenum and iron, that was not present on the MoO_3 system. The radical is able to link to either of the centres, the choice may be affected by multiple elements: the local surface morphology, *i.e.* steric hindrances encountered by the radical during its diffusion towards the T site, the diverse metal centre locations that may favour the choice for the T site closer to the radical or the competition between metal centres in terms of intrinsic energy stabilizations provided to the radical at the adsorption.

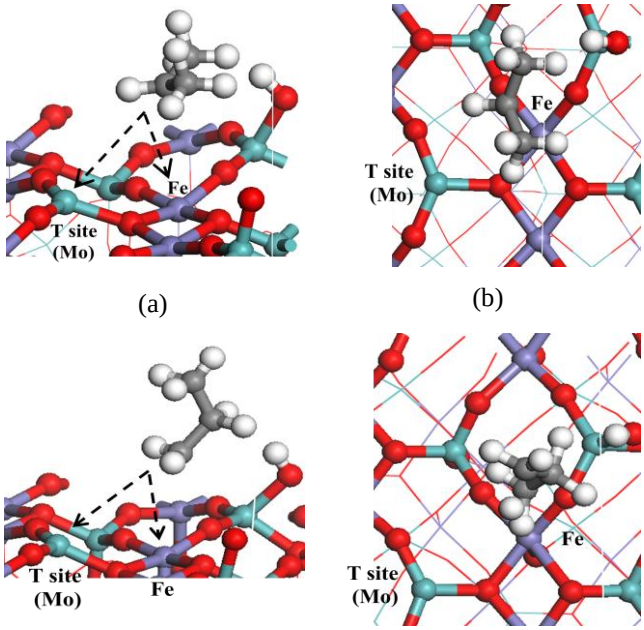

Figure 6.27. Possible paths a radical could choose to adsorb: (a) isopropyl and (b) propyl radicals; (b) isopropyl and (d) propyl radicals from above (key: Mo atoms are blue, O atoms are red, Fe atoms are purple, C atoms are grey, H atoms are white).

Figure 6.27 shows the possible adsorption paths for the radicals on iron molybdate: although the isopropyl radical seems more likely to clash with molybdyl groups (a) than the propyl radical (c), the mixed metal surface is less crowded than MoO_3 in molybdyl groups: they are in fact more widely spaced on the former system than on the latter, so a secondary mode of adsorption may be more favoured on $Fe_2(MoO_4)_3$.

Table 6.7. Adsorption energies for the radicals on $Fe_2(MoO_4)_3(001)$ and $(\bar{1}10)$ surfaces: comparison of the two T sites in competition, namely Mo(IV) and Fe(III), for the full cell model.

Model System (Catalyst)	**Reaction energy (eV)**			
	Terminal[a)]		**Secondary**[b)]	
	Mo	**Fe**	**Mo**	**Fe**
$Fe_2(MoO_4)_3$ (001)	1.04	0.70	0.10	0.87
$Fe_2(MoO_4)_3$ $(\bar{1}10)$	-	-	0.44	0.60

[a)] Propyl and [b)] isopropyl radical adsorption modes.

Figure 6.28 shows the simulation of propyl adsorption on iron molybdate (001) surface (a) Mo and (b) Fe centres: the surface is optimized on a p(3×3) cell (terminal adsorption mode in table 6.7).

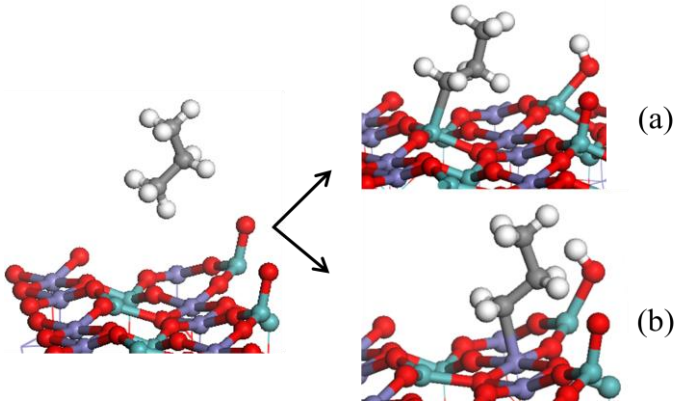

Figure 6.28. Terminal adsorption of the propyl radical on iron molybdate (001) (a) Mo and (b) Fe active sites – full cell (key: Mo atoms are blue, O atoms are red, Fe atoms are purple, C atoms are grey, H atoms are white).

Figure 6.29 shows the same reaction for the isopropyl radical adsorption on (a) molybdenum and (b) iron centres of the (001) surface (secondary adsorption mode in table 6.7). Visually, there appear to be no noticeable difference between terminal and secondary mode on this surface.

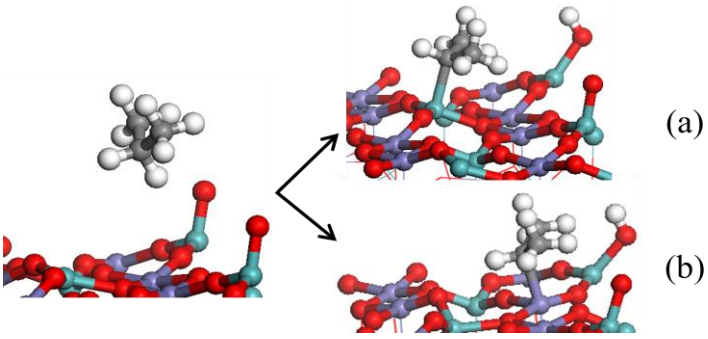

Figure 6.29. Secondary adsorption of isopropyl radical on iron molybdate (001) (a) Mo and (b) Fe active sites – full cell (key: Mo atoms are blue, O atoms are red, Fe atoms are purple, C atoms are grey, H atoms are white).

The last system analyzed for the mixed metal oxide is the one shown in figure 6.30 where isopropyl radical adsorbed on (a) molybdenum and (b) iron centres of the $(\bar{1}10)$ surface: it is possible to notice that this surface is slightly more crowded in molybdyl groups than the (001) surface (secondary adsorption mode in table 6.7).

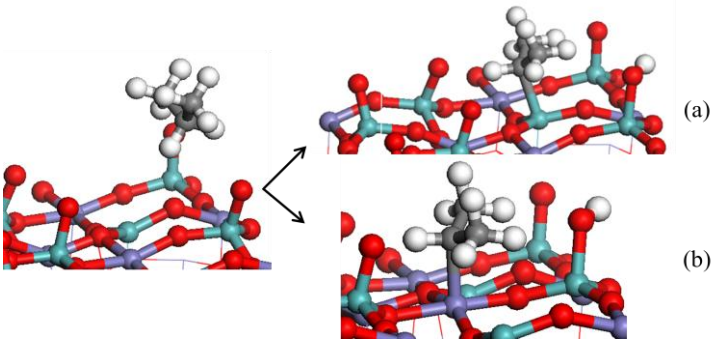

Figure 6.30. Secondary adsorption of isopropyl radical on iron molybdate $(\bar{1}10)$ (a) Mo and (b) Fe active sites – full cell (key: Mo atoms are blue, O atoms are red, Fe atoms are purple, C atoms are grey, H atoms are white).

6.4.4 C–H bond activation

Substrate diffusion showed that on these mixed metal systems there are more choices of surface cations for the radical to adsorb to: the high reactivity of the radical induces interactions with the surface metal centres during the radical transfer towards the surface point defect. These interactions radical-surface could only be relatively controlled on the $Fe_2(MoO_4)_3$ surfaces by limiting the substrate diffusion.

As already discussed, the presence of a different metal centre other than molybdenum gives rise to a competitive adsorption where the T site can either be a Mo or Fe centre; this competition is clearly reproduced by the calculations, as shown in figure 6.31 (full cell model): the graph compares transition state (TS) searches with Mo(IV) and Fe(II) as T sites. Although the substrate diffusion has been limited, corrugated plots are visible at the start of the run. As shown in figure 6.32, the C–H bond homolysis for the "Mo" run appears to occur earlier (at shorter C–H distance) than what seems to happen for the "Fe" run, although with more energetic expense.

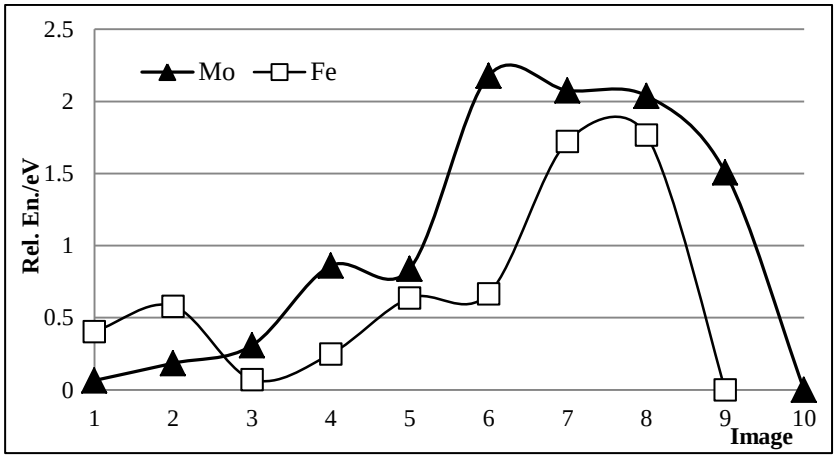

Figure 6.31. NEB plot for the terminal mode adsorption of propyl radical on $Fe_2(MoO_4)_3$(001) surface (full cell).

The terminal C–H activation plots seem to confirm what already discussed for figure 6.31, unless the actual saddle point (maximum) of the "Fe" curve occurs at around 2 Å (and not ~3 Å) of C–H distance, which would change the interpretation of the comparison between the two.

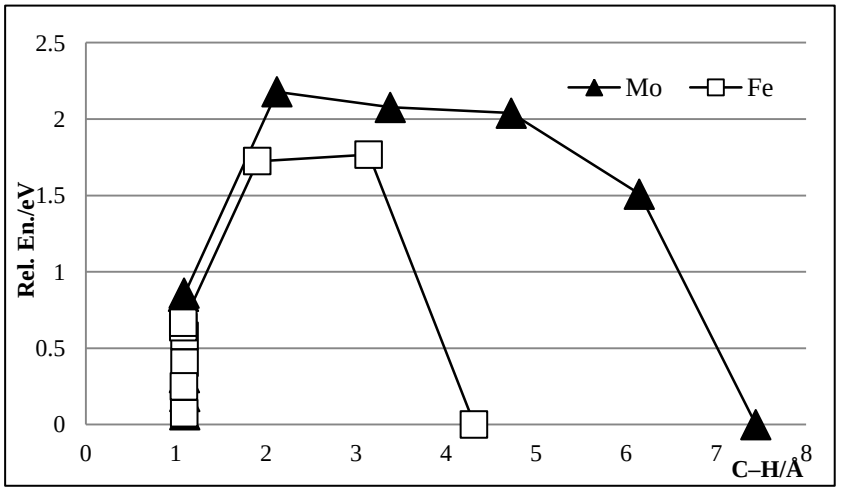

Figure 6.32. Propane terminal C–H activation on $Fe_2(MoO_4)_3$(001) surface (full cell): energy as a function of the C–H bond distance.

6.5. Conclusions

The creation of MoO_3(010) surface point defects, by removing a single terminal oxygen atom (O_T), is the first step in the reaction scheme shown in figure 6.3. The calculated defect formation energy shows discrepancy between the 4 slab- and 2 slab-models (table 6.4): this could be an indication that the absence of the bottom layer in the latter model may be source of an unphysical general destabilization for the system, translated in this instance into making the relative top surface less available to be reduced (higher energy). A further indication of this destabilization was noticed during the NEB visual checks carried out for the 2-slab model when top bi-layer "tremors" were observed: due to its high reactivity, the alkyl radical interacted with alternative surface metal centres spread along its journey to the T site, and the lack of a bottom layer was identified as the reason of the surface's jumping.

A dispersion correction[31] was introduced in order to describe in a better way the inter-layer (or inter-slab) van der Waals (vdW) interactions. The correction is more noticeable on the 4 slabs system where the vdW interactions are much more strongly present between the two bi-layers than between the two slabs of the mono bi-layered model: 0.47 eV is the difference in energy between the corrected (0.89 eV) and uncorrected (1.36 eV) 4 slabs system, which is in favour of the less availability of the model to be reduced when the correction is introduced.

The cluster models appear less available to be reduced than the surface they were originated from; this seems consistent with the fact that for a cluster the stabilization following an oxygen atom removal leads to a substantial change in the energy of the system, and in particular the smaller the dimensions of the structure, the higher the energy penalty to pay. This is clearly observed in the pattern of the energy necessary to create a point defect because values decrease from smaller to larger structures (table 6.4), approaching the surface energy that, in this respect, seems as if it represented a very large cluster itself.

The defect energy for the iron molybdate system (table 6.6) shows slightly higher values for both (001) and $(\bar{1}10)$ surfaces than for the (4 slab) molybdate, which is an indication that in a mixed material the MoO_3 component would be more easily

reduced. No results were available for the half-cell iron molybdate model at the time this thesis was written therefore no direct comparison could be made.

The radical adsorption (figure 6.3, step 3) has been quantified by the calculation of the adsorption energy for the substrate in terms of a surface bound radical and (O)H group on each surface. Table 6.5 collects these data: according to the calculations, both primary (terminal) and secondary radical reactions are slightly unfavourable on MoO_3(010): with only one defect on the surface, the vertical molybdyl (Mo=O) groups interact with the substrate through their O_T atoms, and this is likely to cause steric clashes that may be reflected in the adsorption energy. Further support to this effect was found when adsorption was modelled on MoO_3 clusters (table 6.5): the figures obtained for a cluster containing one metal centre ($Mo_1O_6H_6$) also show that the radical adsorption is unfavourable (positive energy), as the rest of the clusters also confirm. The slight discrepancy in values with MoO_3(010) reflects the nature of the systems analyzed: $Mo_1O_6H_6$ cluster is forced to employ H atoms at the edges to mimic the effect of the surface periodicity; also, the presence of one only lattice O atom hosting the cleaved H atom was identified as a most likely limiting factor that can raise the energy if compared to larger clusters (and ultimately the surface), where more options are available.

The local geometry of the iron molybdate surfaces (001) and $(\bar{1}10)$ is such that the distance the radical has to cover in order to be stabilized by binding to the surface defect is greater than in MoO_3. This is reflected by the data summarized in table 6.7 where the mixed metal surface calculations produced values that are all higher than those relative to the molybdate surface (table 6.5). This MoO_3/$Fe_2(MoO_4)_3$ difference is also reproduced in the terminal (primary) C–H bond activation (figure 6.3, step 2) energy: 1.3 eV is the barrier found on the MoO_3 (4 slab model), which is lower than 2.1 eV found for the $Fe_2(MoO_4)_3$(001) (full cell model). As anticipated earlier, iron molybdate has two competitive adsorption sites: the calculations show though that the Mo site is almost always dominant for (001) surface, and the same pattern over the $(\bar{1}10)$ surface is also described.

Figures for the adsorption energy show consistency throughout the models and the terminal and secondary adsorption modes. The active catalysts are usually systems of

mixed MoO_3 and $Fe_2(MoO_4)_3$ phases where the iron molybdate is viewed as a support for MoO_3 which is the actual source of the oxidizing agent, namely oxygen: this is consistent with the results showing that the C–H activation barrier is lower on MoO_3 than on $Fe_2(MoO_4)_3$, which means that the latter surface alone is not a good catalyst for the alkane activation step (figure 6.3, step 2) of the reaction.

References

[1] J. Haber, E. Lalik *Catal. Today*, **33**, 119 (1997).
[2] L. E. Cadus, M. C. Abello, M. F. Gomez, J. B. Rivarola *Ind. Eng. Chem. Res.*, **35**, 14 (1996).
[3] G. Pacchioni, F. Frigoli, D. Ricci *Phys. Rev. B*, **63**, 054102 (2000).
[4] M. Nolan, S. Grigoleit, D. C. Sayle, S. C. Parker, G. W. Watson *Surf. Sci.*, **576**, 217 (2005).
[5] X.-B. Feng, N. M. Harrison *Phys. Rev. B*, **69**, 132502 (2004).
[6] R. Coquet, D. J. Willock *Phys. Chem. Chem. Phys.*, **7**, 3819-3828 (2005).
[7] L. E. Cadus, M. F. Gomez, M. C. Abello *Catal. Lett.*, **43**, 229 (1997).
[8] R. Schlögl, A. Knop-Gericke, M. Hävecker, U. Wild, D. Frickel, T. Ressler, R. E. Jentoft, J. Wienold, G. Mestl, A. Blume, O. Timpe, Y. Uchida *Topics Catal.*, **15**, 219 (2001).
[9] M. R. Smith, U.S. Ozkan *J. Catal.*, **142**, 226 (1993).
[10] E. Serwicka *J. Solid State Chem.*, **51**, 300 (1984).
[11] E. Serwicka *Crit. Rev. Surf. Sci.*, **1**, 27 (1990).
[12] A. Magneli *Nature*, **165**, 356 (1950).
[13] H. Jönsson, G. Mills, K. W. Jacobsen *Classical and Quantum Dynamics in Condensed Phase Simulations*, ed. B. J. Berne, G. Ciccotti, D. F. Coker (1995), Singapore: World Scientific.
[14] G. Mills, H. Jönsson *Phys. Rev. Lett.*, **72**, 1124 (1994).
[15] G. Mills, H. Jönsson, G. K. Schenter *Surf. Sci.*, **324**, 305 (1995).
[16] Gaussian 09, Revision **D.01**, M. J. Frisch, G. W. Trucks, H. B. Schlegel, G. E. Scuseria, M. A. Robb, J. R. Cheeseman, G. Scalmani, V. Barone, B. Mennucci, G. A. Petersson, H. Nakatsuji, M. Caricato, X. Li, H. P. Hratchian, A. F. Izmaylov, J. Bloino, G. Zheng, J. L. Sonnenberg, M. Hada, M. Ehara, K. Toyota, R. Fukuda, J. Hasegawa, M. Ishida, T. Nakajima, Y. Honda, O. Kitao, H. Nakai, T. Vreven, J. A. Montgomery, Jr., J. E. Peralta, F. Ogliaro, M. Bearpark, J. J. Heyd, E. Brothers, K. N. Kudin, V. N. Staroverov, R. Kobayashi, J. Normand, K. Raghavachari, A. Rendell, J. C. Burant, S. S. Iyengar, J. Tomasi, M. Cossi, N. Rega, J. M. Millam, M. Klene, J. E. Knox, J. B. Cross, V. Bakken, C. Adamo, J. Jaramillo, R. Gomperts, R. E. Stratmann, O. Yazyev, A. J. Austin, R. Cammi, C. Pomelli, J. W. Ochterski, R. L. Martin, K. Morokuma, V. G. Zakrzewski, G. A. Voth, P. Salvador, J. J. Dannenberg, S. Dapprich, A. D. Daniels, Ö. Farkas, J. B. Foresman, J. V. Ortiz, J. Cioslowski, and D. J. Fox, Gaussian, Inc., Wallingford CT, 2009.
[17] J. P. Perdew, K. Burke, M. Ernzerhof *Phys. Rev. Lett.*, **77**, 3865-3868 (1996).
[18] G. Kresse, J. Hafner *Phys. Rev. B*, **47**, 558 (1993).
[19] G. Kresse, J. Hafner *Phys. Rev. B*, **49**, 14251 (1994).
[20] J. P. Perdew *Phys. Rev. B*, **33**, 8822 (1986).
[21] P. E. Blöchl *Phys. Rev. B*, **50**, 17953 (1994).
[22] G. Kresse, J. Joubert *Phys. Rev. B*, **59**, 1758 (1999).
[23] D. Vanderbilt *Phys. Rev. B*, **13**, 5188 (1990).
[24] U. S. Ozkan, R. B. Watson *Catal. Today*, **100**, 101-114 (2005).
[25] S. L. Duradev, G. A. Botton, S. Y. Savrasov, C. J. Humphreys, A. P. Sutton *Phys. Rev. B*, **57**, 1505 (1998).
[26] P. J. Hay, W. R. Wadt *J. Chem. Phys.*, **82**, 270 (1985).
[27] W. R. Wadt, P. J. Hay *J. Chem. Phys.*, **82**, 284 (1985).
[28] M. Chen, U. V. Waghmare, C. M. Friend, E. Kaxiras *J. Chem. Phys.*, **109**, 6854-6860 (1998).
[29] L. Kihlborg *Ark. Kemi*, **21**, 357-364 (1963).
[30] R. Tokarz-Sobieraj, K. Hermann, M. Witko, A. Blume, G. Mestl, R. Schlögl *Surf. Sci.*, **489**, 107-125 (2001).
[31] S. Grimme *J. Comp. Chem.*, **27**, 1787 (2006).

[32] M. Witko, R. Tokarz-Sobieraj *Catal. Today*, **91-92**, 171-176 (2004).
[33] http://theory.chem.cf.ac.uk/~dave/inter_vasp.html.
[34] http://www.hector.ac.uk/.
[35] From private conversation with Dr. Simon Kondrat.

7. General conclusions

The direct partial oxidation of alkanes is a very complex topic in catalysis. The approach adopted in this work to study alternative catalytic supporting systems directed the choice to diverse theoretical methods, each one suitable to face multiple challenges and model different materials.

An investigation over the influence of the restricted environment inside zeolitic microporous materials on the regioselectivity of the reaction was carried out with a Monte Carlo (MC) simulation approach. The use of an adaptable in-house program like *Zebedde*[1] allowed performing a significant study on configurations and energetics to establish a connection between theory and experimental data.[2] The demonstration that the constraints of the host channels drive the selectivity to terminal positions of one molecule of substrate is an important result. It does though represent the initial step of what it could be a larger MC study of zeolites filled up to the level dictated by external partial pressure or concentration of molecules of alkanes. Future studies could be addressing the simulation of realistic low concentration reactions simulated by Grand Canonical Monte Carlo (GCMC) methods to attempt a quantification of loading measures and so the effect of alkane-alkane interactions on selectivity.

Going back to this study, the MC simulations of different guest/host systems sampled a large number of positions, orientations and configurations available to the guest molecules and this generated a considerable amount of data. In principle, these calculations could carry on sampling structures even after reaching a balanced energetic level. Therefore, it was important to find a trade-off between limiting the data to manage CPU time and having a statistically meaningful description of the events. The choice of running 10^6 MC steps calculations revealed appropriate because the averaged energy was able to reach an equilibrated level, and the standard deviation of the energy confirmed that the sampled configurations formed an ensemble. The amount of data generated was large to be handled, so it was decided

to "peek" a frame every 10^3 sampled structures in order to build up the body of data to generate plots, *etc*. The study attempted to give a contribution in describing the basics that the frameworks *regioselectivity* is based on. The geometry analysis carried out through the C_{alkane}–$O_{zeolite}$ and C_{alkane}–$Si_{zeolite}$ distances monitoring studies managed to probe the intimate aspects of the host-guest interactions, in an attempt to contribute with the information gathered from alternative methods. A study using a hybrid approach employing quantum mechanics (QM) and molecular mechanics (MM) to further describe the insights of this reaction was planned to be undertaken. It was shown[3] that a hybrid approach can bypass the inability of DFT to describe the dispersion effect via corrections implemented by parameterized dispersion terms. This approach in principle may be able to deliver a deeper understanding of the oxidation mechanism where the extra-framework metal cation, represented initially by Al, plays a central role: the QM part would be represented by the metal cation and the immediate neighbouring framework region (active site), treated by the hybrid DFT method, while the remainder of the framework (MM region) would be treated with the computationally less expensive MM approximations.

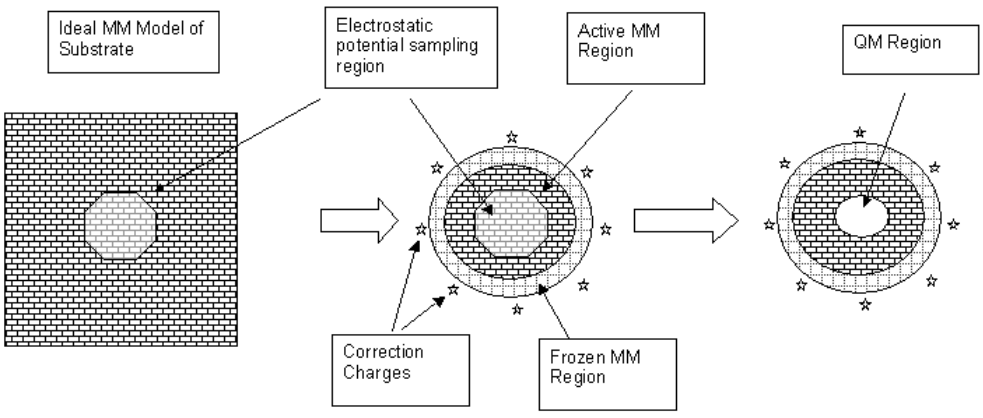

Figure 7.1. Drawing representing the charge fitting approach: it enables a finite cluster to model accurately a single QM defect within an infinite classical crystalline system (figure taken from www.chemshell.org).

ChemShell[4] (CS), the package chosen for the QM/MM study, is a computational environment that uses external methods and codes to perform calculations and handles data and communications. The commands entered in CS are interpreted *via* a

Tool Command Language (TCL) package linked to CS executables. The calculations set up in this study would have used the GAMESS-UK[5] code for the QM part and the DL-POLY[6] code for the MM part.

CS carries out simulations of condensed phase materials by cutting spherical clusters from those materials where the MM part is the outer region of the sphere and the QM part is the cluster core. The software does not implement periodic boundary conditions (PBC) but employs a charge fitting approach that allows finite clusters to model a single QM defect within an infinite crystalline system. An infinite periodic system is initially modelled with the MM approach (figure 7.1(a)). A cluster is cut from the infinite model (figure 7.1(b)) and the outer region is kept frozen to model the MM region while the core is where the QM part is going to be embedded. Computation of the central region electrostatic potential is carried out for both the infinite and finite model (cluster) and their difference represents the error introduced when the cluster is considered in QM/MM calculations performed with CS. Introducing the corrective charges reduces this error by their positioning on the cluster surface and around the outside, further away. The magnitude of the charges is calculated by least-square fitting to the error so that they can compensate for the neglected long-range electrostatic terms, and the QM region is then defined (figure 7.1(c)).

Figure 7.2 shows the setup for a QM/MM calculation where a molecule of methanol adsorbs inside the core region of an Al-exchanged CHA[7] zeolite cluster. This system was chosen for setup purposes.

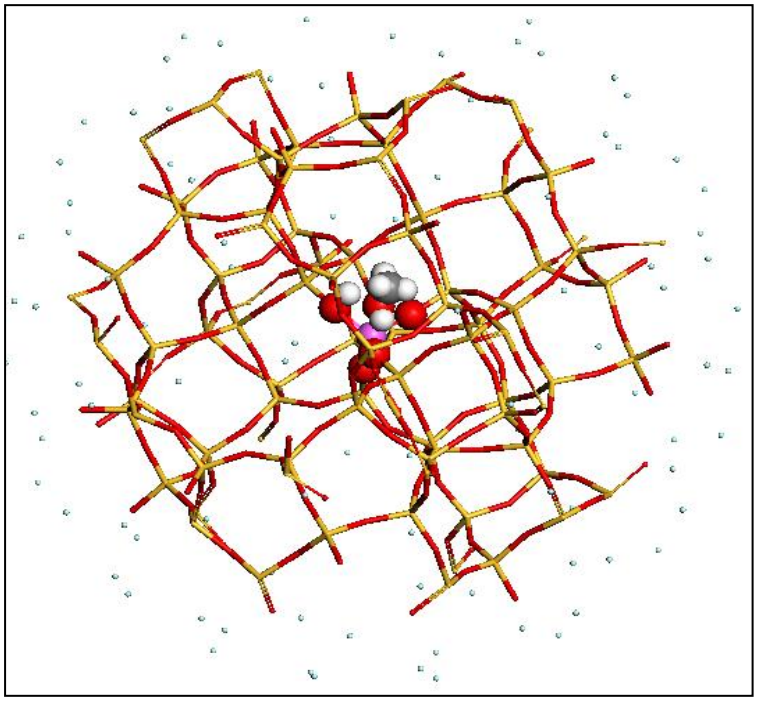

Figure 7.2. ChemShell[3] input structure of an Al-exchanged CHA zeolite cluster with a molecule of methanol at its centre: the molecular mechanics (MM) part is the outer region (red sticks are O atoms, yellow sticks are Si atoms), the quantum mechanics (QM) part is the core of the cluster (white spheres are H atoms, red spheres are O atoms and the pink sphere is the Al atom). On the outside, correction charges (represented by F atoms collared in light blue) to model the finite cluster inside a periodic system are visible.

A lengthy setup required for the *ab initio* calculations (using VASP[8,9]) dealing with the alternative supporting systems (molybdates) studied in this project, brought the progress of the QM/MM study to protracted delays in the completion of its setup. Also, the length of each individual VASP calculation was CPU time consuming. This was due to the combination two factors, namely the large system studied (up to 152 atoms including adsorbate and the 4 sub-layers MoO_3(010) surface, with 37 being Mo atoms) and the limited computational time window (24 h) for a single run available on the Hector Supercomputer[10] (the machine supplying the computational resources dedicated to the VASP part of this study), as discussed in chapter 6. Furthermore, a major hard disk failure of the Raven ARCCA Cluster[11] (the machine dedicated to the QM/MM part of this project) occurred prevented the QM/MM study initial results from being presented in this thesis. The corruption of Raven file system "/home" caused an unrecoverable loss of majority of stored data, affecting

backup and emergency data recovery system facilities too. The lost data relative to the QM/MM study were stored on Raven before December 2012. The external firms involved for the recovery exercise, in collaboration with the supercomputer supplier (Bull), advised that the data recovery would involve decoding tape backup libraries, operation that would have required a longer period of time than that available for the submission of this thesis.

The use of DFT+U and hybrid DFT methods was successful in describing surface systems without being affected by the electron self-interaction problem that DFT methods suffer from, as demonstrated in previous calculations[12] over the same oxide surfaces.

Two models of the defective MoO_3(010) surface were studied. The DFT+U approach to study those models showed that the simplification represented by considering only one bi-layer model may have optimized the computational resources employed but it may have also introduced an unphysical element of structural instability due to the lack of interactions of mainly van der Waals (dispersion) nature. This is consistent with results relative to the same calculations where the dispersion correction[13] was applied: a lesser contribution of the correction to the one bi-layer model was observed because targets of the correction are forces that in the simpler system are partially neglected.

The cluster models treated with hybrid DFT methods did find consistency in the results with those of the periodic DFT+U calculations. The slight disagreement in adsorption energy though is expression of the intrinsic difference of setups in the two types of calculations, combined with the different response of the methods to the self interaction problem.

The DFT+U consistency in treating these periodic systems was further probed with the iron molybdate surfaces. Results of defect energy and transition state (TS) energy barrier, both higher in the mixed metal system, confirmed that in a $MoO_3/Fe_2(MoO_4)_3$ system the $Fe_2(MoO_4)_3$ component acts as a support of the MoO_3 component, which acts like an oxygen reservoir.

The initial C–H activation is the rate limiting step in both molybdate and iron molybdate components. The energy barrier found for MoO_3(010) is ~ 1.45 eV for the

4-slabs model and to ~ 2 eV for the 2 slab model. The energy barrier found for the $Fe_2(MoO_4)_3$(001) surface is ~ 1.75 eV for the adsorption occurring on the Fe centre, and just over 2 eV for the adsorption on the surface defect (Mo(VI)). The further progress of the study over molybdate (010) surface and the iron molybdate (001) and $(\bar{1}10)$ surfaces will provide with a fuller picture of the two components of the actual catalyst. The investigation of the step relative to the second H transfer onto MoO_3(010) surface will allow to fully describe the *redox* cycle where product desorption and replenishment of the surface defect are the final stages of this reaction. The description of a similar *redox* mechanism for $Fe_2(MoO_4)_3$(001) and $(\bar{1}10)$ surfaces will also be the next step for this study, once the analysis of the rate limiting step, *i.e.* C–H activation, for the $Fe_2(MoO_4)_3$(001) surface is complete. Also, attempts will be made to find transition states (TS) for all the remaining adsorption modes occurring on both the competing active sites, *i.e.* Mo(IV) and Fe(III), available in the two surfaces of the mixed metal system.

References

[1] D. W. Lewis, D. J. Willock, C. R. A. Catlow, J. M. Thomas, and G. J. Hutchings *Nature* **382**, 604 (1996).
[2] B.-Z. Zhan, B. Modén, J. Dakka, J. G. Santiesteban, E. Iglesia *J. Catal.*, **245**, 316-325 (2007).
[3] T. Kerber, M. Sierka, J. Sauer *J. Comput. Chem.*, **29**, 2088 (2008).
[4] P. Sherwood, A. H. de Vries, M. F. Guest, G. Schreckenbach, C. R. A. Catlow, S. A. French, A. A. Sokol, S. T. Bromley, W. Thiel, A. J. Turner, S. Billeter, F. Terstegen, S. Thiel, J. Kendrick, S. C. Rogers, J. Casci, M. Watson, F. King, E. Karlsen, M. Sjøvoll, A. Fahmi, A. Schäfer, C. Lennartz *J. Mol. Struct. (Theochem.)*, **632**, 1 (2003).
[5] M.F. Guest, I. J. Bush, H.J.J. van Dam, P. Sherwood, J.M.H. Thomas, J.H. van Lenthe, R.W.A Havenith, J. Kendrick *Molecular Physics*, **103** (6-8), 719-747 (2005).
[6] http://www.stfc.ac.uk/CSE/randd/ccg/software/25526.aspx.
[7] Ch. Baerlocher and L.B. McCusker, Database of Zeolite Structures: http://www.iza-structure.org/databases/.
[8] G. Kresse, J. Furthmüller *J. Comp. Mat. Sci.*, **6**, 15 (1996).
[9] G. Kresse, J. Furthmüller *J. Phys. Rev. B*, **54**, 169 (1996).
[10] http://www.hector.ac.uk/.
[11] http://www.cardiff.ac.uk/arcca/index.html.
[12] R. Coquet, D. J. Willock *Phys. Chem. Chem. Phys.*, **7**, 3819-3828 (2005).
[13] S. Grimme *J. Comp. Chem.*, **27**, 1787 (2006).

Appendix 1

Tabulated Force Field Parameters (PCFF)[1]

Symbol	Mass (CRC 1973/74 pp B-250)	Non-bond		Atom type
		r	ε	
C	12.01115	4.0100	0.05400	sp^3 carbon (terminal and methylene)
H	1.00797	2.9950	0.02000	bonded to C atoms
Si	28.08600	0.0001	0.0000	Si atom in zeolites
O	15.99491	3.4506	0.1622	O atom between two Si atoms

$$E_{nonbond} = \varepsilon_{ij}\left(2\left(\frac{r^0{}_{ij}}{r_{ij}}\right)^9 - 3\left(\frac{r^0{}_{ij}}{r_{ij}}\right)^6\right) \qquad r_{ij} = \left(\frac{r^6{}_{ii} + r^6{}_{jj}}{2}\right)^{\frac{1}{6}} \qquad \varepsilon_{ij} = 2\sqrt{\varepsilon_{ii}\varepsilon_{jj}}\left(\frac{r^3{}_{ii}\, r^3{}_{jj}}{r^6{}_{ii} + r^6{}_{jj}}\right)$$

Quartic bond					
I	J	R_0	K_2	K_3	K_4
C	C	1.5300	299.6700	-501.7700	679.8100
C	C	1.5300	299.6700	-501.7700	679.8100
C	H	1.1010	345.0000	-691.8900	844.6000
C	H	1.1010	345.0000	-691.8900	844.6000
O	Si	1.6155	325.4430	-9433640	1454.6700

$$E_{quartic\_bond} = K_2(R - R_0)^2 + K_3(R - R_0)^3 + K_4(R - R_0)^4$$

Quartic angle						
I	J	K	Θ	K_2	K_3	K_4
C	C	C	112.6700	39.5160	-7.4430	-9.5583
C	C	H	110.7700	41.4530	-10.6040	5.1290
H	C	H	107.6600	39.6410	-12.9210	-2.4318
O	Si	O	110.6120	154.1860	-68.6595	23.6292

$$\Delta = \Theta - \Theta_0$$

$$E_{quartic\_angle} = K_2\Delta^2 + K_3\Delta^3 + K_4\Delta^4$$

Torsion									
I	*J*	*K*	*L*	*V(1)*	$\Phi_1(0)$	*V(2)*	$\Phi_2(0)$	*V(3)*	$\Phi_3(0)$
C	C	C	C	0.1223	0.0	0.0514	0.0	-0.2230	0.0
C	C	C	C	0.0000	0.0	0.0514	0.0	-0.1430	0.0
C	C	C	H	0.0000	0.0	0.0316	0.0	-0.1681	0.0
C	C	C	H	0.0000	0.0	0.0316	0.0	-0.1781	0.0
H	C	C	H	-0.1432	0.0	0.0617	0.0	-0.1083	0.0
H	C	C	H	-0.1432	0.0	0.0617	0.0	-0.1383	0.0
O	Si	Si	O	-0.3417	0.0	0.0961	0.0	0.1683	0.0

$$E_{torsion} = \sum_{n=1,3} \{V(n)[1-\cos(n\Phi - \Phi_0(n))]\}$$

References

[1] J.-R. Hill, J. Sauer *J. Phys. Chem*, **99**, 9536-9550 (1995).